Optical Properties of Nanowire-based Quantum Dots across the Near-Infrared

Lingxi Yu

Thesis submitted to the University of Ottawa
in partial fulfillment of the requirements for the
Master's degree in Physics

Department of Physics
Faculty of Science
University of Ottawa

Abstract

Ideal single-photon sources are key elements to realizing quantum technologies such as quantum information processing and cryptography, using photons as the smallest unit to carry information. Solid-state two-level emitters are considered promising candidates for generating single photons with high efficiency, high single-photon purity and a high degree of indistinguishability. In particular, quantum dots, made of binary semiconductor (e.g. II-VI, III-V) materials, are artificial atoms that exhibit outstanding optical performance. A well-studied example is the InGaAs/GaAs self-assembled quantum dot system. However, these dots are typically formed through random nucleation on a sample substrate. To overcome this barrier, a position-controlled nanowire-based quantum dot system, made of InAsP/InP will be investigated in this work.

This thesis will first introduce the growth technique of embedding a disk-shaped quantum dot (InAsP) in a nanowire waveguide (InP). The optical properties of three different samples with tunable emission wavelengths are demonstrated. A tuning range from 890 nm to 1530 nm is achieved using two approaches. By varying the size and the As composition of the dot, the emission wavelengths can reach up to $\sim 1\,\mu$m. Furthermore, devices can be made to operate in the telecom C-band by employing a dot-in-a-rod structure. Time-resolved photoluminescence measurements and second-order auto-correlation measurements are conducted under different excitation schemes (above-band, p-shell and resonant excitation) to investigate the optical performance of these samples.

For the first time, strictly resonant excitation was applied to the nanowire quantum dot system. Photoluminescence spectra, coherent control, and auto-correlation measurements demonstrated that the pump laser's overlap with the quantum dot emission can be effectively suppressed using a polarization-rejection optical setup. Additionally, experimental results suggest that resonant excitation significantly reduces the excitation timing jitter compared to above-band excitation.

Lastly, this work focuses on the coherence properties and two-photon indistinguishability of the photons emitted from different samples. Linewiths were measured using high-resolution photoluminescence spectroscopy with a Fabry-Pérot etalon and the two-photon indistinguishability was investigated with Hong-Ou-Mandel interferometry. Both measurements were performed under above-band and resonant excitation. The linewidths and the visibilities of the two-photon interference consistently demonstrated the impact of excitation methods on the coherence properties and aligned well with findings from other quantum dot systems.

Statement of Contributions

First of all, all the research was done at the optics lab of the National Research Council Canada, with facilities provided by Dr. Robin L. Williams and Dr. Dan Dalacu. The nanowire quantum dot samples that were investigated in this work were prepared by Dr. Sofiane Haffouz and grown by Dr. Philip J. Poole.

This thesis was entirely written by the author, who also performed all data analysis and plotting. The author independently investigated the optical properties of nanowire quantum dots at 4 Kelvin using non-resonant excitation. The measurements and data analysis presented in Sections 4.1 to 4.3, and the linewidth measurements using non-resonant excitation were all conducted by the author.

Andrew N. Wakileh and the author contributed equally to the project on telecom C-band nanowire quantum dots, including experimental measurements, data analysis, plotting, and the initial drafting of the article. This work marks the first demonstration of single-photon emission from nanowire quantum dots in the telecom C-band. The article titled ***Single photon emission in the telecom C-band from nanowire-based quantum dots*** was published at the *Applied Physics Letters* in 2024.

Sayan Gangopadhyay and the author equally contributed to the project on resonant excitation of nanowire quantum dots. Their contributions included the development of the optical setup and experimental measurements of photoluminescence spectra, Rabi oscillations, lifetime, single-photon purities, linewidths and two-photon indistinguishabilities. The power control program used in the experiments was developed by Kai-Sum Chan. All the measurements and results were performed on nanowire quantum dots for the first time. The results were partially included in the manuscript ***On demand single photon generation and coherent control of excitons from resonantly driven nanowire quantum dots*** uploaded to the arXiv in 2024.

Publications and Conferences

Article 1 A. N. Wakileh, L. Yu, D. Dokuz, S. Haffouz, X. Wu, J. Lapointe, D. B. Northeast, R. L. Williams, N. Rotenberg. P. J. Poole, & D. Dalacu, "Single photon emission in the telecom C-band from nanowire-based quantum dots", Applied Physics Letters **124**, 044006 (2024).

Article 2 J. Gao, G. Krishna, E. Yeung, L. Yu, S. Gangopadhyay, K.-S. Chan, C.-T. Huang, T. Descamps, M. E. Reimer, P. J. Poole, D. Dalacu, V. Zwiller, & A. W. Elshaari, "On demand single photon generation and coherent control of excitons from resonantly driven nanowire quantum dots", arXiv:2409.14964.

Conference 1 "On-demand single photon emission in the telecom C-band from nanowire-based quantum dots", poster presentation, Schawlow-Townes Symposium on Photonics, 2023

Conference 2 "Towards nanowire quantum dot-based high-performance single-photon sources operating in the telecom C-band", poster presentation, Quantum Days, 2024

Conference 3 "Unconventional Temperature-dependence of the Zero-phonon Linewidth in Nanowire Quantum Dots", oral presentation, ICPS, 2024

Acknowledgements

I would like to express my gratitude to many individuals from the National Research Council who supported me throughout my master's program.

First and foremost, I would like to thank my supervisor Dr. Dan Dalacu for his encouragement, guidance and patience. Thank you for providing me with the incredible opportunity to work on the fascinating project of nanowire quantum dots. Your mentorship has been invaluable to my growth as a researcher. Further, I would like to thank Dr. Philip J. Poole, Dr. Robin L. Williams and Dr. David B. Northeast for sharing their profound expertise in III-V semiconductor materials and quantum optics. A special thanks goes to Philip for growing the nanowire samples discussed in this work. I extend my thanks to Dr. Marek Korkusinski, whose brilliant insights and patient teaching helped me understand the theory of quantum dots more deeply.

Thanks also go to Dr. Patrick Laferriére and Edith Yeung, my lab partners and mentors, for introducing me to the fundamentals of experimental optics. Patrick, thank you for teaching me laser alignment, laser safety and data analysis techniques. Edith, thank you for your guidance on handling fibres, sample exchange and organizing, and the pick-and-place technique. Thank you, Andrew N. Wakileh, it was a pleasure collaborating with you on the C-band telecom quantum dots. I am also grateful for your advice on improving my presentation skills and all your support in the lab.

Outside NRC, I would like to first thank Jakob Devey from the University of Waterloo, who was a co-op student at NRC. Thank you for guiding me through the optical experiments at the very beginning to help me get started. Secondly, a great thanks goes to Sayan Gangopadhyay, a PhD student from the University of Waterloo. Working with you on the resonant excitation project was a truly enjoyable and enriching experience. Thanks for all the support and advice in building the optical setup and taking measurements. These could never have been done so efficiently without you. I would also like to thank Dr. Jun Gao and Dr. Ali W. Elshaari from KTH Royal Institute of Technology, for their advice on the resonant excitation setup.

I am also thankful to my friends, Yiqin, Keyan and Weifan for for their constant support and for bringing so much joy into my life. A special thanks to Yuexi, my safe harbour, for always being there for me. I'll always cherish the coffee you make. Lastly, my deepest gratitude goes to my parents. Thank you for your unconditional support in my studies and my life, and for respecting every decision I make. You have been my greatest friends and my unwavering source of strength. I will always love you.

To Mr. Collin

Good morning! Life is beautiful.

Table of Contents

List of Figures

List of Tables

List of Abbreviations

2DEG Two-Dimensional Electron Gas 16

AB Above-Band xv, 64, 69, 70, 72

AFM Atomic Force Microscopy xi, 17

BS Beamsplitter xiii, 29, 30, 32, 42, 44

CBE Chemical-Beam Epitaxy 19

CBR Circular Bragg Resonator xvi, 76, 77

CCD Charge-Coupled Device 38

CMOS Complementary Metal-Oxide-Semiconductor 30

CW Continuous-Wave xiii, 34, 35, 42, 43, 47, 55, 67

D-A Donor and Acceptor 20, 24

DBH Double-Barrier Heterostructure 16

DOS Density of States 10

DROD Dot-in-a-Rod xii, 24, 26, 53, 58, 75

FDTD Finite-Difference Time-Domain xi, 21, 22

FP Fabry-Pérot viii, xiii, 39, 40

FSR Free Spectral Range 40

FSS Fine Structure Splitting x, 14, 67, 68, 77

FWHM Full-Width Half Maximum 40

GUI Graphical User Interface 37

h-BN Hexagonal Boron Nitride 2

HBT Hanbury-Brown and Twiss x, 7, 8, 42, 44, 51, 72

HH Heavy Hole 11, 12

HOM Hong-Ou-Mandel xv, 67, 71

HRPL High-Resolution Photoluminescence viii, xv, 28, 38, 39, 41, 69, 72

HWP Half-Wave Plate 43, 44

LH Light Hole 11, 12

LP Linear Polarizer 32, 33

MZI Mach–Zehnder Interferometer xiii, 43, 44, 70

NA Numerical Aperture 28

NPBS Non-Polarizing Beamsplitter 34

PBS Polarizing Beamsplitter xiii, 32, 34, 43, 44, 60, 69, 70, 72

PD Photodetector 34

PL Photoluminescence xi, xii, xiv, xv, 16, 18, 23, 27, 28, 33–35, 37, 38, 44, 46–48, 54, 55, 58, 60, 61, 63, 67, 74, 75

PLE Photoluminescence Excitation 48

PM Polarization-maintaining xii, 27, 32, 36, 43

QWP Quarter-Wave Plate 32, 34, 44, 60, 61, 72

RF Resonant Fluorescence xiii, xv, 28, 33, 34, 36, 62–67, 69, 70, 72, 75, 76

S-K Stranski-Krastanov xi, 16–18

SA Selective Area 19

SA-VLS Selective-Area Vapour-Liquid-Solid 19

SEM Scanning Electron Microscope xi, xvi, 20, 25, 54, 76

SF Stacking Faults 20

SFWM Spontaneous Four-Wave Mixing 2, 6

SM Single-mode xii, 21, 27, 36, 37

SNSPD Superconducting Nanowire Single-Photon Detector xiii, 38, 39, 41, 42, 44, 51

SOI Silicon on Insulator xvi, 76, 77

SPDC Spontaneous Down-Conversion 2, 6

TCSPC Time-Correlated Single-Photon Counting 41

TEM Transmission Electron Microscope xi, 20, 53

TMDC Transition Metal Dichalcogenides 2

TMI Trimethylindium 19

TPI Two-Photon Interference 8, 58, 59, 71, 72, 75–77

TRPL Time-Resolved Photoluminescence viii, ix, xiv, 28, 38, 41, 46, 48, 56, 66, 74, 75

VHG Volume Holographic Grating 35

VLS Vapour-Liquid-Solid 19, 20

WZ Wurtzite 20, 24

ZB Zincblende 20, 24

ZPL Zero-Phonon Linewidth 14, 15

List of Symbols

$\boldsymbol{l}$ Orbital Angular Momentum 10, 11

$\boldsymbol{s}$ Electron Spin 10, 11

$\boldsymbol{j}$ Total Angular Momentum 11, 12

Chapter 1

Introduction

Quantum science and technologies have shown their transformative potential across academic research and industries, generating significant excitement in multiple fields. The quantum theory of light can be traced back to when Planck first postulated his hypothesis on quantized energy in particles [8], followed by Einstein's famous proposal on "light quanta" in the early 1900s [9]. Around eighty years later, the concept of single-photon sources emerged. To this very day, single-photon technologies are applied in an expanding range of fields [10]. Here, I will mainly discuss their applications in quantum computing [11, 12], quantum information [13] and cryptography [14].

Quantum information can be encoded in photons as they have various degrees of freedom, allowing them to represent the states of qubits. For example, the horizontal polarization of a photon can represent the qubit state $|0\rangle$ and the vertical polarization can represent the state $|1\rangle$. These photons can be further manipulated by using linear optical elements acting as quantum gates. One of the most common examples is beamsplitters where the photons can interfere with each other. Moreover, photons can be implemented for secure communications due to their quantum properties through, for example, the non-cloning theorem. Many works have used single photons or entangled photon pairs to demonstrate quantum key distribution schemes [15, 16].

One key step to advancing quantum technologies is the development of on-demand single-photon sources with high performance. These sources must exhibit high efficiency, high single-photon purity and the ability to produce indistinguishable photons with a high degree of coherence. Furthermore, their compatibility with optical fibre is essential for ensuring scalability in quantum networks.

1.1 Single-photon generation

Based on the underlying physical processes, single-photon sources can be categorized into two types: deterministic and probabilistic sources. Historically, the sources that generate pairs of entangled photons were first developed in the early 1970s [17, 18]. These are so-called heralded single-photon sources, meaning that they utilize the detection of one photon (i.e. the heralding photon) from a generated pair to ensure the presence of the correlated one (i.e. the heralded photon). This can be achieved by nonlinear optical processes such as spontaneous down-conversion (SPDC) or spontaneous four-wave mixing (SFWM). Particularly, high-energy photons (e.g. lasers) interact with nonlinear materials and generate two photons with different energies, namely an idler/heralding photon and a signal/heralded photon. While the process is inherently random in that the photon-pair generation is probabilistic, these sources can operate at room temperature with a wide range of wavelength tunability, high indistinguishability, high-quality entanglement and broad applications in integrated photonics [19, 20, 21, 22, 23].

Despite the probabilistic sources being well-established and widely applied, the inherent trade-off between their source efficiency and single-photon purity limits their application in many fields [24]. Therefore, on-demand deterministic single-photon sources are more desirable as they can generate one photon at a time in a controllable manner. Solid-state materials have shown their significant potential as such sources [25]. **Trapped atoms and ions** served as the earliest examples of single-photon sources due to their well-defined energy levels [26]. More recent work has shown their ability to generate single photons at telecom wavelengths [27]. However, several disadvantages, including low collection efficiency, complex experimental setups and challenges in integrating with photonic devices, limit their scalability [28]. **Point defects in solids** is another promising technique to realize single-photon generation. This is achieved by introducing localized defects in the crystal lattice of a material to form confined energy levels. Well-known examples include nitrogen-vacancy centers in diamond [29] and silicon-vacancy centers in silicon carbide [30]. Two-dimensional materials such as transition metal dichalcogenides (TMDCs) and defects in hexagonal boron nitride (h-BN) are also prominent hosts for single-photon emitters.

1.2 Semiconductor quantum dots: outline of the thesis

Semiconductor quantum dots, known as "artificial atoms", have shown their extreme potential as deterministic sources to generate high-purity single photons [31] as well as high fidelity entangled photon pairs [32]. They are typically lower bandgap materials embedded within higher bandgap materials, forming spatial confinement for charge carriers with nanoscale dimensions. Single photons can be generated through spontaneous emission when the dots are optically excited by lasers.

One of the common methods to fabricate solid-state semiconductor quantum dots is epitaxial growth where one single-crystalline material (e.g. InAs) is deposited on the surface of another single-crystal material (e.g. GaAs). In particular, the Stranski–Krastanow technique produces quantum dots of random sizes and at random positions through strain-induced nucleation. The major disadvantages of these dots are low collection efficiency and broad photon linewidths. Total internal reflection due to a high index of refraction of the dots results in only a small amount of light being collected from above. The random nucleation leads to the linewidth broadening of the dot emission due to the spectral pollution from adjacent dots. A significant amount of research has been done in the past to address these by cooperating quantum dots with photonic structures [33].

This work, in contrast, presents single-photon sources based on nanowire quantum dots. First, the concept of quantum light is introduced through photon statistics in **Chapter 2**, followed by a detailed background of semiconductor quantum dots. The latter half of this chapter focuses on nanowire quantum dots, covering the growth methods, the source efficiency and the wavelength tunability. **Chapter 3** describes the experimental methods used in this work. In **Chapter 4**, typical optical properties of quantum dot samples grown under different conditions are investigated, including their photoluminescence spectra, excitonic lifetimes and single-photon purities using above-band and p-shell excitation. In particular, the quantum dots operating in the telecom C-band is presented. Further, the coherence properties of different quantum dots emitting below 1 μm are compared using above-band and strictly resonant excitation. Lastly, **Chapter 6** provides a brief conclusion of the experimental results and future research directions.

Chapter 2

Semiconductor Quantum Dots as Single-photon Sources

In this chapter, I will start with the concept of quantum light by discussing photon statistics. Among different types of non-classical light sources, single-photon sources have become one of the most promising candidates for quantum technologies. In the past years, semiconductor quantum dots have shown their significant potential as on-demand single-photon sources, capable of generating high-quality single photons and entangled photon pairs. Such photons can serve as quantum bits for long-distance quantum networks.

Motivated by these, I will provide an overview of semiconductor quantum dots in the second section, covering from the fundamental physics, including their electronic and optical properties, to various types of quantum dots that have been developed to date. Lastly, I narrow the focus to III-V nanowire-based quantum dots, discussing the growth techniques and their corresponding optical performance.

2.1 Photon Statistics

Photon statistics theory provides a framework for distinguishing and characterizing different types of light based on the probability distribution of the number of photons. With a given probability of detecting n photons, on can analyze the variance of detecting n photons ($(\Delta n)^2 \equiv \langle n^2 \rangle - \langle n \rangle^2$) in relation to the mean of photon number ($\langle n \rangle$), to distinguish three different types of light sources; thermal light ($(\Delta n)^2 > \langle n \rangle$), coherent light ($(\Delta n)^2 = \langle n \rangle$)

and quantum light ($(\Delta n)^2 < \langle n \rangle$). Each type of light corresponds to a different photon distribution behaviour: super-Poisson, Poisson and sub-Poisson distribution, respectively.

For the light emitted from a single-mode thermal light source, such as a light bulb, the intensity fluctuates randomly. By cooperating the intensity distribution with Mandel's formula, the probability of finding n photons at a photodetector is given by Bose-Einstein distribution [34]:

$$P_t(n) = \frac{\langle n \rangle^n}{(1 + \langle n \rangle)^{n+1}} \tag{2.1}$$

This distribution implies that the detection of zero photons has the highest probability, as shown in Figure 2.1(a). In this case, the variance is calculated to be $(\Delta n)^2 = \langle n^2 \rangle + \langle n \rangle$.

Single-mode coherent light, e.g. light emitted from a laser, is characterized by the coherent state $|\alpha\rangle$ as a superposition of Fock states $|n\rangle$:

$$|\alpha\rangle = e^{-|\alpha|^2/2} \sum_{n=0}^{\infty} \frac{\alpha^n}{\sqrt{n!}} |n\rangle \tag{2.2}$$

where α is a complex amplitude. Eq. 2.3 shows that the probability distribution in the coherent state is Poissonian:

$$P_c(n) = \frac{|\alpha|^{2n}}{n!} e^{-\langle n \rangle} = \frac{\langle n \rangle^n}{n!} e^{-\langle n \rangle} \tag{2.3}$$

where the probability of finding n photons is maximized at the mean photon number, as shown in Figure 2.1(b). The variance is then calculated as $(\Delta n)^2 = \langle n^2 \rangle$, indicating lower intensity fluctuation than the thermal light.

In contrast to the classical light sources (i.e. thermal light), non-classical light, such as Fock states, allows for a precise definition of the photon number, as shown in Figure 2.1(c). The origin of the photon number state is from the formalism of second quantization. For a single-mode of a Fock state, it satisfies:

$$\hat{n} |n\rangle = n |n\rangle \tag{2.4}$$

where $\hat{n}$ is the number operator and equals to the product of annihilation and creation operators: $\hat{n} = \hat{a}^\dagger \hat{a}$. The probability distribution to find n photons is then:

$$P_q(n) = \begin{cases} 1, & \text{if } n = n'. \\ 0, & \text{otherwise.} \end{cases} \tag{2.5}$$

This sub-Poissonian behavior is the hallmark of quantum light, leading to a minimized variance in photon number with $(\Delta n)^2 < \langle n^2 \rangle$. Therefore, quantum light sources exhibit the lowest photon number fluctuation compared to classical light sources.

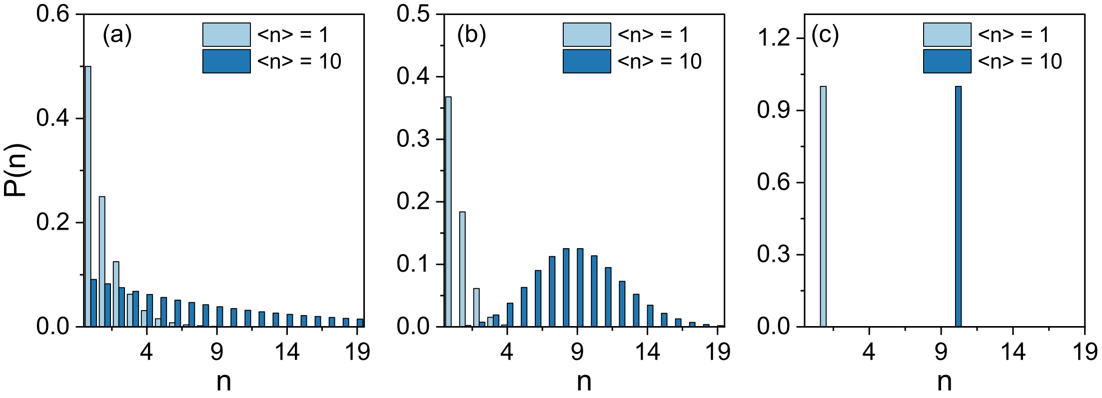

Figure 2.1: Probability distribution of finding n photons from (a) a thermal light source, (b) a coherent light source, and (c) a quantum light source. For each type of light, the distributions are plotted when $\langle n \rangle = 1$ (light blue) and $\langle n \rangle = 10$ (dark blue), respectively.

While thermal and laser light sources are well-studied and widely applied in day-to-day existence and scientific research, the potential of non-classical light in quantum technologies has drawn massive attention in the past decades [35, 36]. Quantum light can be generated through many processes. For example, squeeze states were observed from a sodium atomic beam pumped cavity through SFWM [37]. Heralded photon pairs can be generated from SPDC [19]. Single-photon Fock states emitted from solid-state semiconductors are presented in [25].

In this work, I focus on the optical properties of single-photon emitters, evaluating their performance based on several key criteria: source efficiency, single-photon purity, two-photon indistinguishability, and photon coherence. Source efficiency is influenced by photon generation mechanisms in different devices, while single-photon purity, indistinguishability and coherence serve as universal performance metrics. In the following section, I will define these three metrics and discuss their respective measurement methods.

2.2 Single-photon purity and spectral purity

One requirement for the ideal single-photon source is having high single-purity. This means that the emitter generates one and only one photon at a given time. Mathematically, this is measured by the Glauber correlation function, or a normalized auto-correlation function [38]:

$$g^{(2)}(\tau) = \frac{\langle E^{*}(t)E(t)E^{*}(t+\tau)E(t+\tau)\rangle}{\langle E^{*}(t)E(t)\rangle^{2}} \tag{2.6}$$

which is an average of coincidences of two events that happen at some time t and a delayed time $t + \tau$, normalized to the joint probability distribution. Specifically, the two events refer to the intensity of light at two times, $I(t) = E^{*}(t)E(t)$ and $I(t + \tau) = E^{*}(t + \tau)E(t + \tau)$, respectively. Considering the intensity functions of light as vectors in Hilbert space and applying Cauchy-Schwarz inequality, we obtain that for the results of N measurements of the intensity:

$$\left(\frac{I(t_1) + I(t_2) + ... + I(t_N)}{N}\right)^{2} \leqslant \frac{I(t_1)^2 + I(t_2)^2 + ... + I(t_N)^2}{N} \tag{2.7}$$

Therefore, we have $\langle I(t)\rangle^2 \leqslant \langle I(t)^2\rangle$, which sets a bound at zero time delay ($\tau = 0$) that $g^{(2)}(0) \geqslant 1$. Note that a classical picture cannot explain events where $g^{(2)}(0) < 1$, but these do occur, for example, with Fock states. In this case, Eq. 2.6 can be written in terms of creation and annihilation operators:

$$g^{(2)}(\tau) = \frac{\langle a^{\dagger}(t)a^{\dagger}(t+\tau)a(t+\tau)a(t)\rangle}{\langle a^{\dagger}(t)a(t)\rangle\langle a^{\dagger}(t+\tau)a(t+\tau)\rangle} \tag{2.8}$$

Using the above equations, one can show that $g^{(2)}(0) = \frac{\langle n(n-1)\rangle}{\langle n\rangle^2} = \frac{\langle n^2\rangle - \langle n\rangle}{\langle n\rangle^2}$. With this expression, one can calculate the second-order correlation at $\tau = 0$ for the different types of light, as summarized in Table 2.1. Experimentally, second-order correlations are measured using a Hanbury-Brown and Twiss (HBT) setup [39] with one 50:50 beam splitter and two detectors, as shown in Figure 2.2. When a series of photons enter one port of a beam splitter, each photon has an equal chance of being directed to either detector 1 or detector 2. A counting module is connected to the two detectors to register each detection event. If the source emits only one photon at a time, the detection at one detector triggers a timer ("start"), while the subsequent detection at the other detector serves as a "stop"

Light	$g^{(2)}(0)$	Phenomena
Thermal light	2	Bunching
Coherent light	1	Uncorrelated
Ideal single-photon	0	Antibunching

Table 2.1: A summary on $g^{(2)}(0)$ values for thermal light, coherent light and ideal single-photon source.

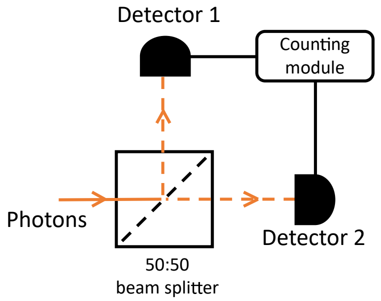

Figure 2.2: An illustration of the HBT setup.

signal. The counting module records coincidences as a function of relative delay between detection events in the two detectors. Consequently, at zero time difference, ideal single photons cannot be registered at both detectors, leading to $g^{(2)}(0) = 0$.

In addition to single-photon purity, indistinguishability and coherence also lie at the heart of photon-based quantum technologies [40, 41]. Photons are, in general, characterized by the degrees of freedom, including temporal and spatial modes, frequencies (or wavelengths) and polarization. Two photons are said to be indistinguishable when they carry the same properties [42]. Experimentally, this is quantified by the visibility in a two-photon interference (TPI) measurement. When two photons are sent into two ports of a 50:50 beam splitter, they should always exit at the same port if they are perfectly identical, otherwise, the two photons may exit from different ports, as illustrated in Figure 2.3. This is known as the Hong-Ou-Mandel effect [43, 44, 45, 46].

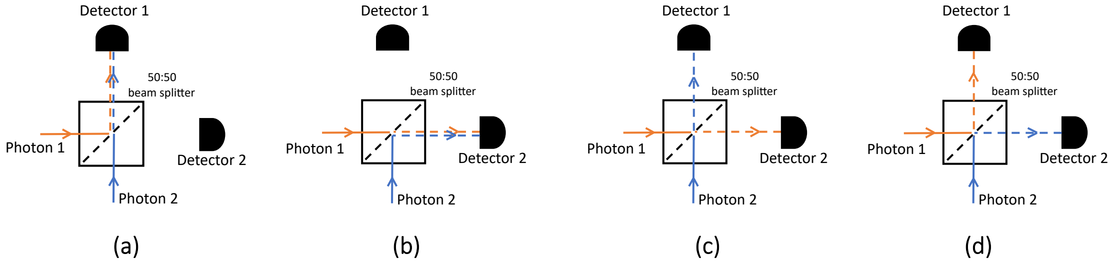

Figure 2.3: The four possibilities for two photons being captured by two detectors after entering the 50:50 beam splitter. If the two photons are non-identical, cases (a), (b), (c) and (d) have an equal probability of happening; however, if the photon 1 and 2 are perfectly indistinguishable, outcomes (c) and (d) will destructively interfere and no coincidences will be registered.

Next, photon coherence is defined as the stability of the photon's phase over time, where a more stable phase means a higher coherence to ensure a higher degree of indistinguishability. Mathematically, the coherence is expressed by the normalized first-order correlation function:

$$g^{(1)}(\tau) = \frac{\langle a^{\dagger}(t)a^{\dagger}(t+\tau)\rangle}{\langle a^{\dagger}(t)a(t)\rangle} \tag{2.9}$$

According to the above, the coherence time is then defined as the time over which a photon maintains a certain phase. One method to obtain information on coherence is to perform an interference measurement using a Michelson interferometer, as described in detail elsewhere [47]. In this thesis, however, I will focus on investigating the sources of the decoherence processes through linewidth measurements. If the photon emitted from a quantum emitter has a long coherence time, it will have stable energy and present as a sharp peak in the dot emission spectrum. In other words, the linewidth of a photon is inversely proportional to its coherence time, meaning that a narrower linewidth corresponds to a higher degree of coherence. Therefore, decoherence in photon emission will result in a broadening in the linewidth. The broadening mechanisms of the linewidth vary across different sources. In the following section, I will present one of the most representative single-photon emitters: semiconductor quantum dots, introducing their electronic and optical properties.

2.3 Background of semiconductor quantum dots

Quantum dots are known as semiconductor artificial atoms whose optical properties are strongly size-dependent, a phenomenon resulting from the quantum confinement effect [48, 49, 50, 51, 52]. The critical size for observing such an effect originates from the Heisenberg uncertainty principle. Consider the simplest case where a particle with mass m is restricted to move in one dimension, then the relation between the uncertainty in the position Δx and the momentum Δp_x satisfies:

$$\Delta x \cdot \Delta p_x \geqslant \frac{\hbar}{2} \tag{2.10}$$

The kinetic energy due to the confined motion can be estimated by Δp_x that

$$E_{confined} \approx \frac{(\Delta p_x)^2}{2m} \approx \frac{\hbar^2}{2m(\Delta x^2)} \tag{2.11}$$

In the classical regime, the equipartition theorem states that particles in a thermal equilibrium system have a continuous energy spectrum evenly distributed in all degrees of freedom [53], expressed as

$$E_{thermal} = \frac{k_B T}{2} \tag{2.12}$$

Therefore, when the confinement energy is greater than the thermal energy, the size of the confinement will have a significant impact on the energy of the system due to the presence of discrete energy levels [54, 55]. The critical value is then given by:

$$\Delta x \leqslant \sqrt{\frac{\hbar^2}{m k_B T}} \approx \lambda_{DB} \tag{2.13}$$

where λ_{DB} is the De Broglie wavelength. In this case, quantum dot systems can be analogous to the problem of a "particle in a box", where the nanoscale semiconductor materials offer confinement of the spatial motion of electrons and holes. Depending on the structure, the confinement can be zero to three-dimensional and the energy distribution (or the density of states (DOS)) can vary [54], as is shown in Figure 2.4. The bulk material has a density of states proportional to the square root of energy. In the case of a quantum well, a lower bandgap material is embedded in a bulk with a higher bandgap, resulting in discrete energy levels in the vertical direction. With further constrain in the lower bandgap material, the motion of electrons/holes is restricted in two dimensions (case of quantum wire in Figure 2.4). In this case, the DOS is inversely proportional to the square root of energy levels. Finally, quantum dots with confinement in all dimensions lead to discrete energy levels in all directions.

2.3.1 Confinement in quantum dots

Typically in the III-V semiconductors, the spin-orbit interaction can be significant when containing materials with relatively heavy atomic mass, leading to a coupling between the electron spin ($\boldsymbol{s}$) and the orbital angular momentum ($\boldsymbol{l}$). The Hamiltonian of such an interaction then takes the form [56]:

Structures		Density of states (DOS(E))
Bulk (Zero confinement)		$\propto \sqrt{E}$
Quantum well (1D confinement)	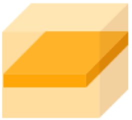	$\propto H(E - E_i)$
Quantum wire (2D confinement)	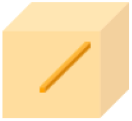	$\propto \dfrac{H(E - E_i)}{\sqrt{E - E_i}}$
Quantum dot (3D confinement)	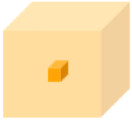	Discrete in all degree of freedom

Figure 2.4: Different structures with 0, 1, 2, and 3-D confinement with their corresponding density of states. In the case of a quantum well and a quantum wire, $H(E - E_i)$ is the Heaviside step function which indicates the levels of quantized energy.

$$H_{so} = \lambda \boldsymbol{l} \cdot \boldsymbol{s} \tag{2.14}$$

where λ is the coupling constant. Eq. 2.14 therefore has eigenstates of total angular momentum j and the component being projected on the z-axis j_z. In III-V semiconductor bulk materials, the bottom level of the conduction band has s-like symmetry with $\boldsymbol{l} = 0$. Together with $\boldsymbol{s} = \pm 1/2$, the total angular momentum for the ground level in the conduction band is then $\boldsymbol{j} = \boldsymbol{l} + \boldsymbol{s} = \pm 1/2$. However, the situation in the valence band is more complicated as the top level of the valence band has p-like symmetry with $\boldsymbol{l} = 1$. Thus the total angular momentum for a hole state can be $\boldsymbol{j} = \boldsymbol{l} \pm \boldsymbol{s} = 3/2$ or $1/2$. One can see from here that the spin-orbit interaction splits the top valence band into two. The one with $\boldsymbol{j} = 1/2$ is called the split-off band and is typically hundreds meV below the $\boldsymbol{j} = 3/2$ band. Moreover, the $\boldsymbol{j} = 3/2$ band consists of a heavy hole (HH) band with $j_z = \pm 3/2$ and a light hole band (LH) with $j_z = \pm 1/2$ [56], which are degenerate at the Brillouin zone centre (Γ). Figure 2.5(a) shows a typical band structure of III-V semiconductor bulk materials. The energy band gap and the separation between the bands depends on the materials, the crystal structures and the strain.

For a strongly confined system, as in a quantum well with sufficiently strong confinement in the ẑ-direction, the degeneracy of the $\boldsymbol{j} = 3/2$ band will be removed, separating the LH and HH bands by tens of meV [57, 58]. This means that only the HH is confined, whilst the LH band is found at higher energies and can be neglected. This is the case for the quantum dots studied here, which are strongly confined in ẑ with a height of a few nanometres. Therefore, when considering a quantum dot, the lowest energy confined levels can be discussed in terms of an s-type electron level and a heavy hole subband. Finally, the lateral confinement of the quantum dots from reduced in-plane dimension further splits these states into s-, p-, and d-shells, as shown in Figure 2.5(b).

In general, the energy levels in a quantum dot can be expressed as:

$$E_l = \frac{\pi^2\hbar^2}{2m^*}\left(\frac{l_x^2}{w_x^2} + \frac{l_y^2}{w_y^2} + \frac{l_y^2}{w_y^2}\right) \tag{2.15}$$

where $l_i = 0,\ 1,\ 2$, etc. are the quantum numbers for each dimension w_i with $i = x,\ y,\ z$. And m is the effective mass of the carrier. Consequently, we can obtain the spin states of electrons: $|1/2, 1/2\rangle$, $|1/2, -1/2\rangle$, and the heavy holes: $|3/2, 3/2\rangle$, $|3/2, -3/2\rangle$. In terms of total angular momentum, we have $|\uparrow\Uparrow\rangle$, $|\uparrow\Downarrow\rangle$, $|\downarrow\Uparrow\rangle$, $|\downarrow\Downarrow\rangle$ with single arrows indicating the electron spin states and the double arrows representing the hole states.

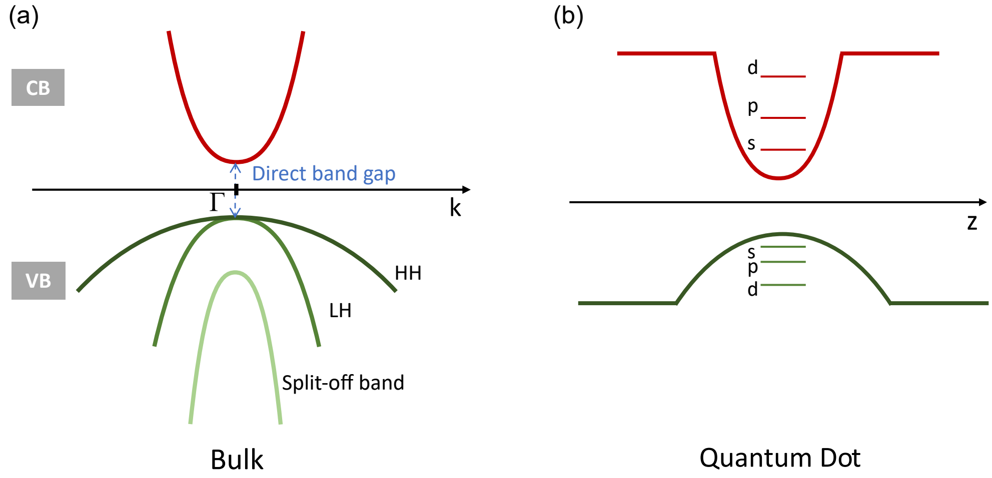

Figure 2.5: Schematic band diagram of (a) a III-V semiconductor bulk material in k-space and (b) a quantum dot with s-, p- and d-shells in the ẑ direction.

By populating the energy levels using a laser, optical transitions can occur through relaxation and recombination. Specifically, if we use the laser to excite the system above the bulk material bandgap, the electrons in the valence band will be excited to the conduction band by absorbing photons with energy greater than the band gap, leaving behind positively charged holes in the valence band. These freely moving electrons and holes can be individually trapped in the quantum dot and radiatively recombine within sub-nanoseconds to a few nanoseconds to emit a photon. Due to the conservation of angular momentum, optical transitions are only allowed for the states with the total angular momentum of ± 1, which are $|\uparrow\Downarrow\rangle$ and $|\downarrow\Uparrow\rangle$. They are also called the "bright excitons", resulting in the emission of photons with right- or left-hand circular polarization. The other two, $|\uparrow\Uparrow\rangle$ and $|\downarrow\Downarrow\rangle$ are referred to as "dark excitons", meaning that they tend to be optically inactive due to weak interaction between electronic spin and photons. They can be visible, however, if one of the spins is flipped when an external field, such as a magnetic field, is applied, allowing radiative recombination to occur.

With different charge and spin configurations in the s-shell, the Coulomb interactions are different, leading to different binding energies. A maximum of two electrons and two holes can be held in the ground state (s-shell). Based on the Pauli exclusion principle, Figure 2.6 illustrates the possible excitonic complexes: the positively and negatively charged exciton (X^+ and X^-), the neutral exciton (X) and the biexciton (XX).

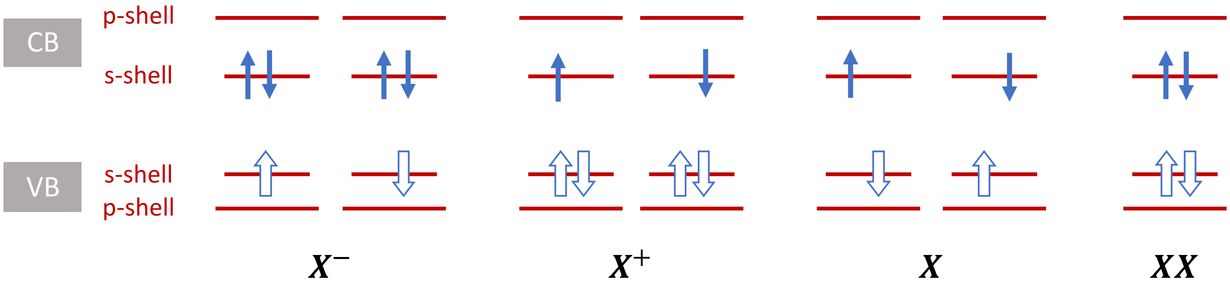

Figure 2.6: Illustration of different charge complexes, where the electrons (solid arrows) are found in the s-shell conduction band and the holes (hollow arrows) are found in the s-shell valence band. The charged excitons are formed by either two electrons and one hole (X^-) or two holes and one electron (X^+). A neutral exciton consists of one electron and one hole, whilst two electrons and two holes form a biexciton.

i. Fine structure splitting and linewidth of excitonic complexes

The charged excitons have either antiparallel electron spins or hole spins which form spin-singlet states that suppress the electron-hole interaction. The emission from the charge excitons is then achieved by decaying directly to the ground state with either a single electron or a single hole, each through a single decay path. The neutral exciton is composed of one electron and one hole, in the form of $|\uparrow\Downarrow\rangle$ or $|\downarrow\Uparrow\rangle$. The two states are, in principle, degenerate for a quantum dot with perfect symmetry around its growth axis. In practice, however, an asymmetry in the confining potential from some anisotropy in the system will lead to a fine structure splitting (FSS). Lastly, the biexciton formed by two electrons and two holes will decay to one of the neutral exciton states by emitting an electron-hole pair. Therefore, it also exhibits a splitting in the emission peak.

Such splittings can be observed as two emission peaks with an energy difference ranging from a couple μeV to a hundred μeV, which depends on various dot structures as well as the effect of external fields [59].

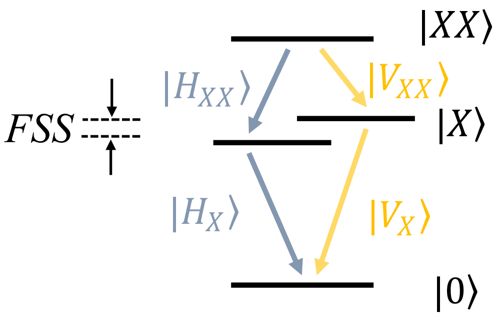

Figure 2.7: Schematic of the biexciton-exciton cascade in the presence of a FSS in the intermediate state.

As mentioned in the previous section, the linewidth of an emission peak from the single-photon source is inversely proportional to the coherence time. In quantum dots, the linewidth of excitonic emission can be expressed as [60]:

$$\gamma = \frac{1}{T_2} = \frac{1}{2T_1} + \frac{1}{T_2^*} \tag{2.16}$$

where T_2 is the coherence time, T_1 is the exciton radiative decay lifetime and T_2^* is the pure dephasing time. Note that without the presence of a decoherence process, i.e. $1/T_2^* = 0$, the linewidth reaches the transform-limited value. Therefore, by investigating the broadening of the photon linewidth, we are able to gain insights into the decoherence of the photon generated by the source.

As a direct result of the Heisenberg uncertainty principle ($\Delta E \Delta t \geq \hbar$), the emission peak of an excitonic complex exhibits a finite width in the energy spectrum, which is limited by its radiative lifetime. This is known as the zero-phonon line (ZPL), and the peak has a Lorentzian shape. While the peak with natural linewidth originates from the intrinsic energy difference between the excited and the ground state, as well as the decay mechanism in the device, the interactions with its environment inevitably broaden the ZPL. In general, there are several factors that lead to either inhomogeneous or homogeneous broadening of the ZPL.

Inhomogenous linewidth broadening is caused by, for example, the charge noise, the spin noise, and inelastic phonon scattering. Due to imperfect material, defects may exist in the bulk material to trap the electrons introduced by the laser pump, leading to a time-varying electric field. Moreover, atomic nuclei carry spin which fluctuates due to thermal or spin-spin interactions and can cause changes in the local magnetic field. The optical transitions of the quantum dot are, therefore, influenced by these sources of noise and the emission energy fluctuates around the central peak. This is referred to as spectral wandering or spectral diffusion [61], which is the main source of linewidth broadening at cryogenic temperatures. The extent of such effect depends on the excitation power [61] as shown in Figure 2.8(a), the excitation method [60, 62], as well as the sample fabrication [63, 64]. Effects of phonon scattering may also play a role in energy shifts in the emission spectrum. Even at low temperatures, longitudinal acoustic photons can be absorbed or emitted during the exciton recombination process, referred to as inelastic phonon scattering. This leads to additional photon emissions at either higher (from absorbing phonons) or lower (by emitting phonons) energies than the radiative recombination energy, appearing as two side lobes around the emission. These are known as phonon sidebands as indicated in Figure 2.8(b).

Furthermore, pure dephasing due to elastic scattering of the phonon can lead to homogeneous broadening of the linewidth. With increasing phonon energy at a higher temperature, the coupling strength between the excitons and the phonons becomes greater. As a result, a linear [65] or a non-linear [66] increase in linewiths is typically observed in the emission from the quantum dot system. Figure 2.8(c) shows a strongly non-linear increase in linewidth as a function of temperature, measured on a nanowire quantum dot. Previous work has shown that such behaviour can be modelled by incorporating the independent boson model with two types of competing exciton-phonon coupling mechanisms, namely the deformation potential coupling and the piezoelectric coupling [1].

2.3.2 Types of quantum dots

Quantum dots can generally be categorized into two types based on the confinement methods: gate-defined quantum dots and material-defined quantum dots.

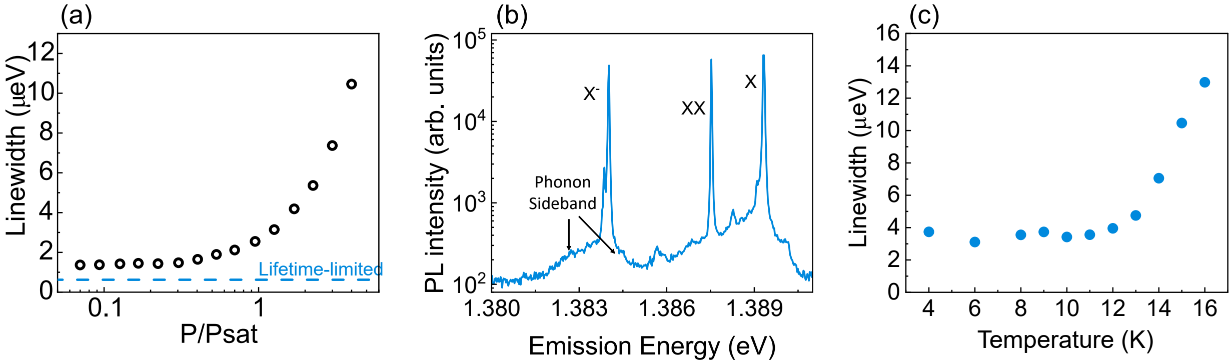

Figure 2.8: Examples of the linewidth broadening mechanisms: (a) inhomogeneous linewidth broadening due to increased excitation power, measured at 4K (adapted from [1]); (b) PL spectrum plotted in a semi-log scale showing the phonon sideband; (c) homogeneous linewidth broadening due to increased temperatures.

As the name implies, the gate-defined quantum dots precisely control the potential of the dot and the number of electrons confined in the dot by manipulating the voltage applied to the gate electrodes. Top-down approaches such as electron-beam lithography are typically employed to fabricate these dots. To characterize such devices, transport spectroscopy is used to measure the tunnelling currents through the dots. Based on the flow direction of the tunnelling current, they can be categorized as vertical or lateral dots [67], as shown in Figure 2.9(a) and (b), respectively. An example of vertical dots is given by Tokura *et. al* [2], who used a double-barrier heterostructure (DBH) to fabricate a pillar-shaped InGaAs/AlGaAs dot, sandwiched in thick layers of n-doped GaAs acting as drain and source. A side gate is additionally placed around the DBH pillar, allowing a reduction in both the quantum dot size and number of electrons, when a negative voltage is applied. The lateral quantum dots, however, are usually built upon the principle of a two-dimensional electron gas (2DEG) formed between a GaAs and an AlGaAs layer where electrons are only allowed to move in-plane [68]. At the surface of the heterostructure, the gates are fabricated with the source and the drain electrodes being applied on the right and left sides of the dots. When a negative voltage is applied, electrons can be depleted or added in a fully controlled manner [69].

On the other hand, the material-defined quantum dots are grown using a bottom-up technique, mostly through epitaxy. One traditional example is self-assembled dots, formed during the growth of lattice mismatched layers [70]. This growth technique, known as Stranski-Krastanov (S-K) growth, starts by depositing a single-crystalline III-V or II-IV semiconductor material on a monolayer substrate to form a strained 2-D layer (so-called

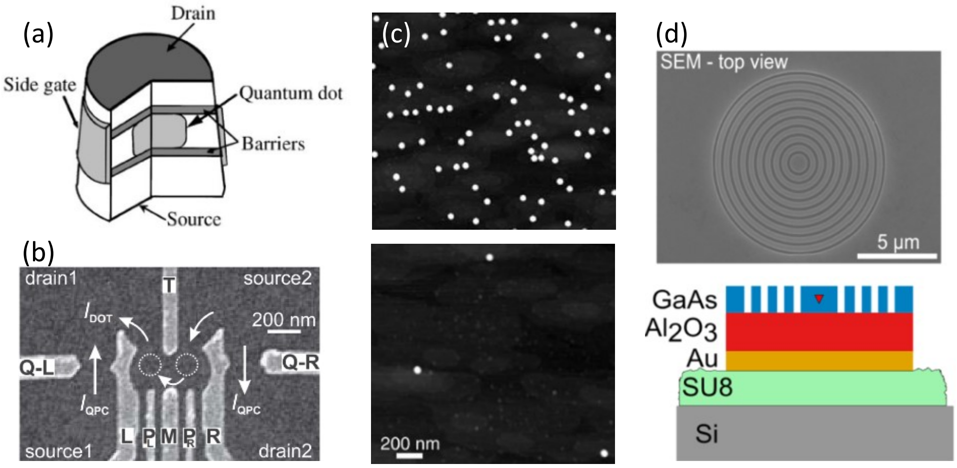

Figure 2.9: Some examples of dots: (a) Vertical, gate-defined quantum dot, adapted from [2]; (b) Lateral, gate-defined quantum dot, adapted from [3]; (c) AFM image showing a top-view of self-assembled S-K quantum dots with high (upper panel) and low (lower panel) dot density, adapted from [4]. (d) An example of cooperating self-assembled quantum dots in a photonic cavity, adapted from [5].

wetting layer). The strain is accumulated as the layers are added until it is sufficiently large and they are energetically favourable to nucleate 3-D islands. Figure 2.9(c) shows an atomic force microscopy (AFM) image of a top view of quantum dots grown using the S-K method [4]. The upper panel shows a larger number of randomly nucleated dots within a certain area, indicating a higher surface density, whilst the lower panel shows a much lower density with a few dots presented within the same area. Optical measurements are typically performed on such dots to examine their performance as non-classical light sources, regarding the brightness, two-photon indistinguishability and single-photon purities.

One of the disadvantages of the S-K emitters is the low collection efficiency due to the high index of refraction of the host material. Total internal reflection can occur, limiting the amount of light emitting out of the samples and being collected from above. The most common solution to address this issue is to incorporate the dots within photonic cavities. Figure 2.9(c) shows an example of embedding the quantum dot in a circular Bragg grating, which significantly improves the spontaneous emission rate of the emitters through Purcell enhancement [5]. While a Purcell factor of 4 is achieved, spatial overlap between the emitter and the cavity mode can be technically challenging.

Therefore, quantum emitters with high spontaneous emission rates and optical mode coupling efficiencies are desired for future applications. Starting from the following section, a nanowire-based quantum dot system will be introduced and presented in detail.

2.4 Nanowire-based quantum dots

The previous section briefly introduced various types of quantum dots defined by gates or materials. While the conventional S-K dots are widely studied, including their incorporation within photonic structures, the random nucleation may limit their optical performance. To address this, this work will focus on a position-controlled quantum dot system, namely nanowire-wire quantum dots. Particularly, this device is made of a disk-shaped indium arsenide (InAs) quantum dot embedded within an indium phosphide (InP) nanowire core with the same diameter as the dot. This core is clad with an InP shell to form a photonic nanowire waveguide.

The following section will discuss the details of the growth technique of InAs/InP nanowire quantum dot devices. Additionally, the generic optical characterization of the emitters will be presented, including the source efficiency in relation to the waveguide geometry, the photoluminescence (PL) spectra, and the single-photon purity of the source.

2.4.1 Growth methods

Prior to the growth of the nanowire, patterned substrates are prepared. To begin with, a 20 nm thick silicon dioxide (SiO_2) mask is deposited on a (111)B surface of an InP wafer, followed by spin-coating of an e-beam compatible positive photoresist. E-beam lithography is then utilized to create arrays of circular patterns through which the SiO_2 is subsequently wet-etched in buffered hydrofluoric acid to form openings. As a result, the InP substrate is exposed exclusively through the openings, providing growth selectivity. This means that no parasitic growth occurs on the SiO_2 mask, allowing for better control of the growth process. The thickness of the SiO_2 mask and the etching time determine the diameter of the openings in the mask, which assists in defining the base diameter of the nanowire waveguide. Afterwards, a thin layer of gold is deposited on top, and the openings in the photoresist allow the Au particles to settle on the InP substrate. The diameters of the Au particles typically range from 5 nm to 20 nm, depending on the thickness of the gold layer, and will define the diameter of the nanowire core and the quantum dots. A cross-section of the layered substrate with openings is shown in the left panel of Figure 2.10. The patterned substrate is finished by a lift-off process to remove the resist and the gold layer, leaving the Au nanoparticles to sit inside the holes, as shown in the right panel of 2.10.

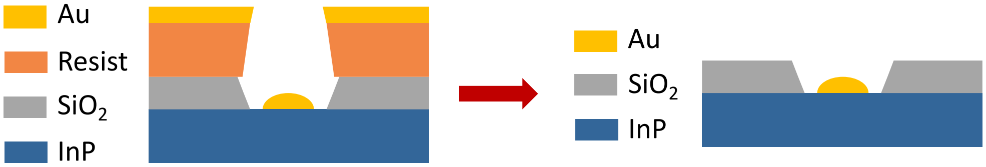

Figure 2.10: The substrate preparation before growing the nanowire quantum dots. The left figure shows a cross-sectional area of a patterned substrate, before the lift-off process. The right figure shows the cross-sectional illustration of a finished one after lift-off, which only consists of a masked InP substrate with Au particles sitting in the middle of an opening.

The growth technique, in a generalized term, is called nanoparticle (Au) catalyzed selective-area vapour-liquid-solid (SA-VLS) epitaxy [71]. This is carried out using chemical-beam epitaxy (CBE) with trimethylindium (TMI), phosphine (PH_3) and arsine (AsH_3) as sources of In, P and As, respectively. The devices are grown in two steps. In the first step, a nanowire core with a section of quantum dot is grown using VLS epitaxy. In this process, the material is only incorporated at the metal/semiconductor interface. As such, the growth is axial, and the diameter of the core is given by the diameter of the gold catalyst. The VLS growth is promoted using appropriate growth conditions, namely low sample temperature ($\sim$ 435°C) and lower group V flux. First, an InP base of the nanowire core is grown by introducing TMI and PH_3 into the reactor. After the growth of $\sim 1\,\mu$m InP, a section of $InAs_xP_{1-x}$ quantum dot is grown by switching from PH_3 to AsH_3 gas. The thickness of the dot will affect the vertical confinement of the charge carriers and can be controlled by the growth time of the section. After a desired amount of time, the PH_3 gas is introduced back into the reactor and AsH_3 is evacuated, leading to a finished nanowire core with a typical height from 4 to $5\,\mu$m, as depicted in Figure 2.11(b).

In the second step, the nanowire core is clad with a shell of InP, as shown in Figure 2.11(c). This radial growth is promoted using different growth conditions: a higher temperature and higher group V flux, i.e. the SA growth mode. This shell defines a waveguide that is required to confine a mode into which the quantum dot can effectively emit. Through careful control of these two growth modes (i.e. by not completely suppressing the VLS mode during the growth of the cladding), the nanowire waveguide can be grown with a tapered tip. The overall height of the tapered nanowire is around $\sim 20\,\mu$m. The inset of Figure 2.12(a) shows a top view of one nanowire. Hexagonal layers with decreasing diameters can be observed, indicating the tapering to the tip. The finished samples consist of 10 by 10 arrays of nanowires, as shown in Figure 2.12(b).

It is worth noting that the crystal structure, the composition of the binary III-V material

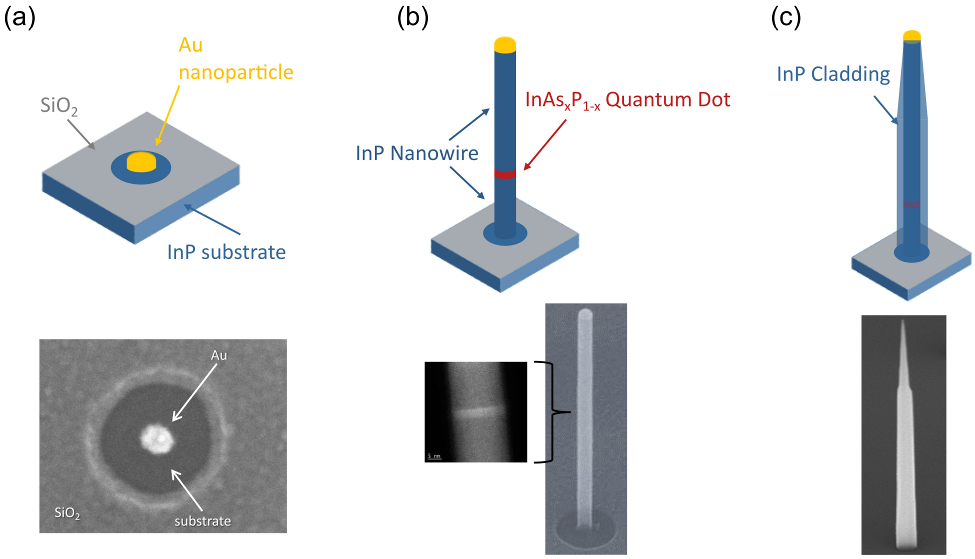

Figure 2.11: Schematics of the growth steps of the nanowire quantum dot devices. (a) illustrates the patterned substrate with a gold particle sitting at the centre of the opening. The SEM image at the bottom shows a top view of the prepared substrate. (b) The growth of a nanowire core with a dot embedded in the middle. The SEM image shows the core and a transmission electron microscopy (TEM) image on the side shows the QD section. (c) The growth of nanowire cladding with a tapered tip is shown in the drawing at the top and the SEM image at the bottom.

and the geometry of the waveguide, work complementarily to affect the optical performance of the device. Particularly, a defect-free sample is preferred as the defects in the nanowire can lead to energy shifts due to the presence of trapped charges. In the nanowire quantum dot samples, traps and defects can exist within the InP core-shell structure and at the sidewalls of the waveguide. The bottom-up epitaxial growth can introduce impurities and defects in both the nanowire core and the surrounding shell, resulting in, for example, shallow donor and acceptor (D-A) levels. Moreover, stacking faults (SF) is a common problem in VLS growth. These are crystal phase transitions between small sections of zincblende (ZB) crystal phase and the predominant wurtzite (WZ) structure. The band alignment of these two crystal phases can also act to trap carriers.

Furthermore, the coupling efficiency to external optics relies significantly on the aspect ratio and the tailoring of the nanowire waveguide geometry. A more detailed discussion of the source efficiency and related optical properties is presented in the following section.

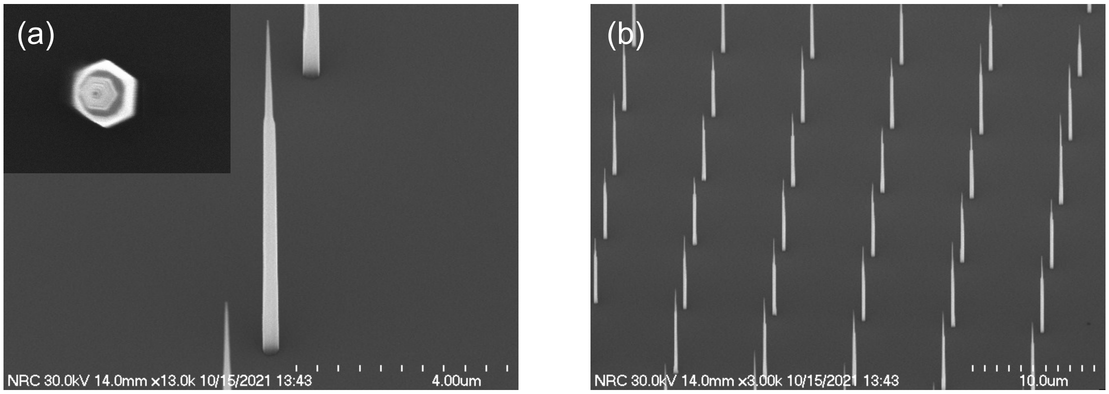

Figure 2.12: SEM images of the nanowire quantum dot sample. (a) A single nanowire viewed at 40° showing a tapered tip. The inset shows a top view of the nanowire, indicating the hexagonal-shaped nanowire core and cladding; (b) An array of nanowire quantum dots, pitched at $7.5\,\mu$m.

2.4.2 Source efficiency

One desirable property of solid-state quantum light emitters is that they can be made highly compatible with single-mode channels, such as optical fibres for long-distance applications or integrated waveguides for on-chip processing [72]. In the nanowire quantum dot system, the mode in which the quantum dot emits is the fundamental waveguide mode HE_{11} confined by the nanowire. Such a mode is preferred as the maximum collection can be achieved with single-mode (SM) fibres.

In this case, we define the source efficiency (η) as the percent of the photons emitted from the dot and being collected at the first lens. By assuming that the internal quantum efficiency of the dot is 100% (i.e. the dot will emit a photon every time it is excited), the source efficiency depends on the fraction of the spontaneous emission from the dot into the fundamental waveguide mode, HE_{11} ($\beta_{\mathrm{HE}_{11}}$):

$$\eta = \alpha\beta_{HE_{11}}; \quad \beta_{HE_{11}} = \frac{\Gamma_{HE_{11}}}{\Gamma_{HE_{11}} + \gamma} \tag{2.17}$$

where α is the fraction of photons collected into the desired external channel, which is maximized at 50% as we assume half of the photons emitted by the QD are guided upwards while the rest are to the substrate. $\Gamma_{\mathrm{HE}_{11}}$ is the spontaneous emission rate from the dot into the HE_{11} mode and γ refers to the spontaneous emission rate into all other modes. Finite-difference time-domain (FDTD) simulation of emission rates $\Gamma_{\mathrm{HE}_{11}}$, γ, and the coupling efficiencies $\beta_{\mathrm{HE}_{11}}$ as a function of normalized waveguide diameter, D/λ, have been done in the past [73] and are plotted in Figure 2.13. Calculated results show that $\beta_{\mathrm{HE}_{11}}$ remains 97% over a large range of D/λ values.

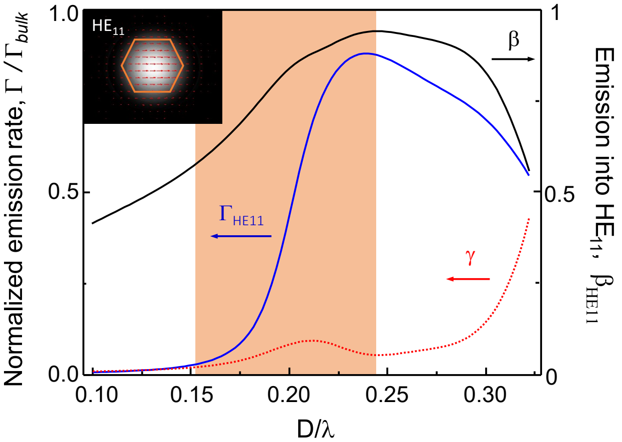

Figure 2.13: Left axis: Results of FDTD simulations of the emission rate into HE_{11} ($\Gamma_{\mathrm{HE}_{11}}$) normalized to the bulk Γ_{bulk} and into all other modes (γ) as a function of normalized waveguide diameter (D/λ). Right axis: Results of FDTD simulation of the dot to HE_{11} coupling efficiency, $\beta_{\mathrm{HE}_{11}}$

Within the presented range of D/λ values, we prefer both a maximized spontaneous emission rate, $\Gamma_{\mathrm{HE}_{11}}$, and coupling efficiency, $\beta_{\mathrm{HE}_{11}}$. One can notice from the plot that a high $\beta_{HE_{11}}$ is obtained for $0.2 < D/\lambda < 0.3$, whilst it is limited at large waveguide diameter by emitting into other modes, and at lower diameter by a small overlap with the dot dipole. Lastly, the requirement on the sources to operate at a high repetition rate gives the best choice for a normalized waveguide diameter of $D/\lambda \approx 0.24$. Overall, this simulation not only provides an insight into the relationship between optical mode coupling and the size of the InP nanowire but also sets a boundary on the waveguide diameter for optical efficiency optimization.

2.4.3 Quantum size effect on the emission energies

After discussing the dependence of collection efficiency and emission rate on the waveguide geometry, I shall discuss the impact of quantum dot dimensions on their optical emission energies. In Eq 2.15, it is easy to notice that energies are discrete and directly related to the size of the quantum dot, which implies that the emission wavelength can be tuned by changing the dot confinement. Indeed, a comprehensive study by Cygorek *et. al* in [74] presents the influence of the atomistic structure on the optical properties of nanowire quantum dots. In particular, the energy gap is larger for the thinner dots, leading to a blue-shift in emission wavelength. The energy splitting between the laterally confined s- and p-type states is, however, strongly dependent on the diameter of the dot where a smaller diameter will result in a larger splitting. Therefore, changing the size and the aspect ratio of the dots not only allow us to tune the ground state emission from 890 nm to 980 nm, but also control the number of confined states.

In the following, I will describe three different quantum dot structures that were studied, labelled A, B, and C. Figure 2.14(a) shows the schematic geometries of the three samples and Figure 2.14(b) shows the corresponding band structures. Table 2.2 summarizes the AsH_3 flow used, the height (H_{dot}) and the diameter (D_{dot}) of the dots from each sample. All the dots are located in the core 1 μm above the substrate and embedded in a waveguide with base diameter $D_B \approx 250$ nm. In sample A, the dots with 20% As concentration, diameters of ∼20 nm and heights of ∼10 nm are targeted. In this case, the confined orbitals are typically s, p, and d-shells [75]).

Sample	**AsH_3 concentration (% of the full scale of the flow)**	**H_{dot} (nm)**	**D_{dot} (nm)**
A	20%	5	20
B	11%	10	10
C	11%	5	10

Table 2.2: A summary of the AsH_3 flow and the dot dimensions of three nanowire quantum dot samples shown in Figure Figure 2.14.

In sample B, a thinner Au layer was deposited compared to sample A, resulting in a nanowire core with a smaller diameter. Additionally, a lower As concentration (<20%) with a longer growth time is used to grow the dot. The dots from this sample are, therefore, expected to have a larger band gap as well as larger s-p splitting according to [74], as shown in Figure 2.14(b). Lastly, in sample C, the As concentration and the diameter of the dot was kept as in sample B but the dot growth time was halved, leading to a smaller dot (H_{dot} ∼5 nm) and corresponding larger energy gap. Using this dot geometry, it is expected that only the s-shell is confined.

The emission energies are manifested through micro-PL measurements. The spectra of three dots, one from each sample, taken with the above-band excitation, are shown in Figure 2.15. More details on how these spectra were taken will be discussed later. Here, using an excitation power saturating the s-shell emission, it is easy to notice that the ground state emissions shift to shorter wavelengths (i.e. higher energy) for the smaller dots with lower As concentration. For all these samples, no clear signs of a broad feature around 860 nm typically associated with recombination from shallow D-A levels are observed. We obtain an s-p splitting of around 30 meV in the dot from sample A and around 60 meV in sample B. However, no p-shell emission is observed in the dot from sample C, which is consistent with the predicted result discussed above. On top of the dot emission, some other emission features are present in samples B and C. Stacking faults that arise from the inserts of ZB crystalline phase between the WZ phase result in emissions ranging from ∼840 nm to ∼860 nm that varies from nanowire to nanowire. The emission from bulk ZB InP at ∼875 nm, is also observed in sample C [73].

One key requirement in producing scalable single-photon devices for long-distance applications is compatibility with fibre networks. Therefore, it is ideal to push the emission into the telecom O-band (1260 ∼ 1360 nm) and C-band (1530 ∼ 1565 nm), where the signal attenuation is minimized. In the nanowire quantum dot system, it is difficult to achieve an As concentration in the dot required for telecom emission without sacrificing source performance, in particular brightness [76]. An alternative route to achieving telecom emission is to employ a dot-in-a-rod (DROD) structure. This is achieved by growing a section of $\mathrm{InAs}_y\mathrm{P}_{1-y}$, (a "rod"), both prior to and after the growth of $\mathrm{InAs}_x\mathrm{P}_{1-x}$ dot [77, 6, 78]. A schematic of such a design with the corresponding band structure is shown in Figure 2.16(a). For the DROD structure, a large cladding, base diameter ∼310 nm, was used for optimizing the collection and the emission rate (see Figure 2.13). Previous work has demonstrated that by employing such a dot structure and waveguide geometry, the emitters can operate in the telecom O-band at a count rate over 1 Mcps when excited at 80 MHz using a pulsed laser [6]. In Chapter 4.4, I will present the details of the growth technique and the optical characterization of the dot emitting in the telecom C-band, incorporating the DROD structure.

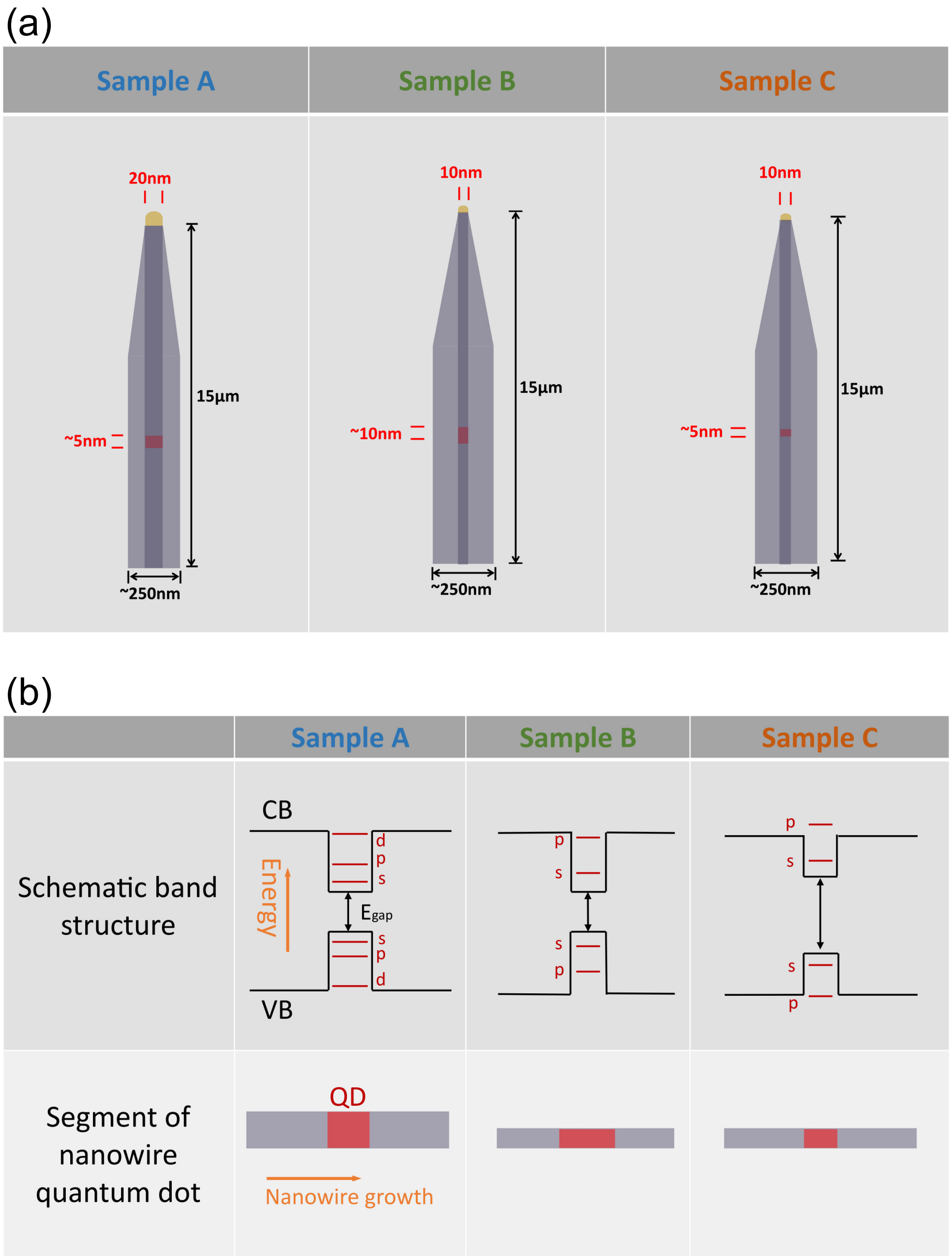

Figure 2.14: Various geometries of quantum dots in nanowire waveguides. (a) shows schematics of the samples with waveguide dimensions based on SEM images. The lower table shows simplified band structures, corresponding to each sample.

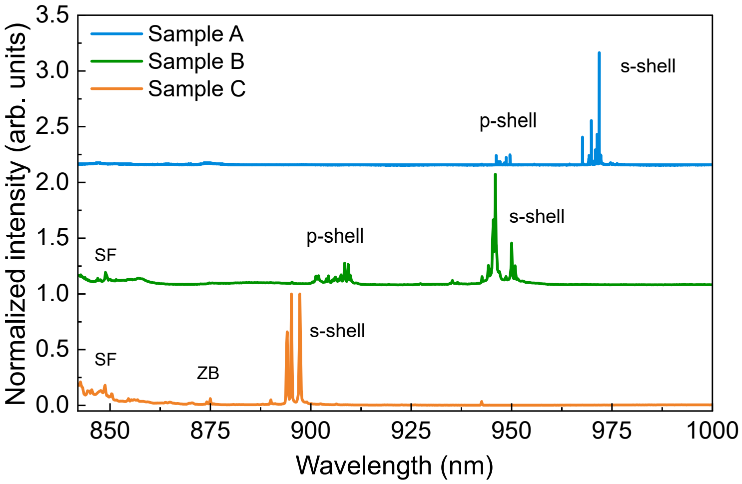

Figure 2.15: The PL spectra of each sample listed in Figure 2.14. Due to the different geometries, the wavelengths of the dot emission shift from below 900 nm to around 975 nm. No p-shell emission is observed in sample C (the orange line), consistent with the band structure as shown in Figure 2.14. Additionally, the s-p splitting in sample B (in green) is larger than that in sample A (in blue) due to a smaller dot diameter in the latter.

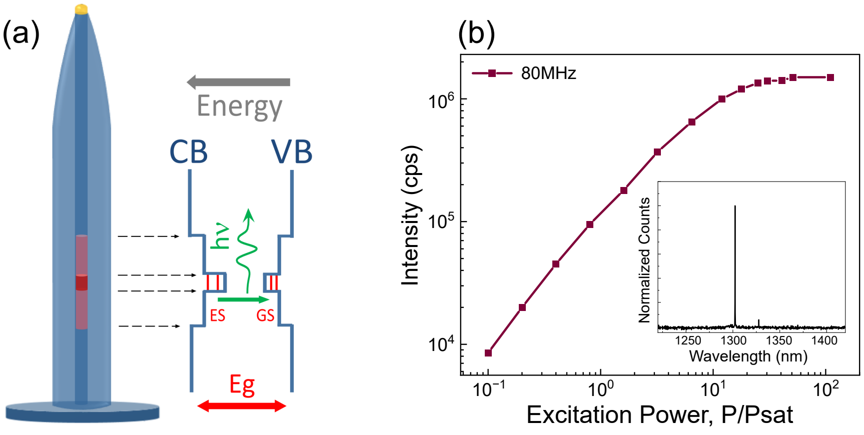

Figure 2.16: (a) Schematic of a dot-in-a-rod structure and band diagram used for quantum dot emission at telecom wavelengths. (b) Count rate as a function of excitation power from an O-band emitter (see inset) grown using the DROD approach, adapted from [6].

Chapter 3

Experimental Methods

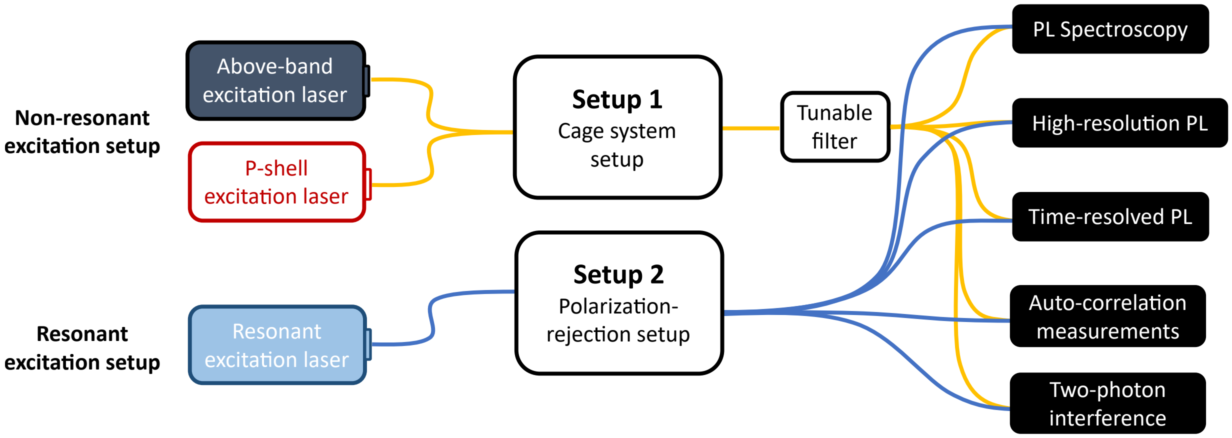

Figure 3.1: An overview of the micro-PL setup with different excitation schemes. The coloured lines indicate the fibre connections with either SM fibres (yellow) or PM fibres (blue). The cage systems for non-resonant excitation and for resonant excitation using polarization rejection consist of free-space optics. A fibre-based tunable filter is used under a non-excitation regime to isolate a single emission line.

In this chapter, I will discuss the equipment and the experimental methods that are used in the optical measurements. Figure 3.1 shows an overall experimental setup. In general, a half-fibre-half-free-space optical setup is used in the experiments, where lasers are guided through SM or polarization-maintaining (PM) fibres to free-space optics and used to excite the quantum dots. The dot emission is then coupled back into fibre and routed to various detection systems to conduct the measurements such as PL spectroscopy, high-resolution photoluminescence (HRPL), time-resolved photoluminescence (TRPL), autocorrelation measurements, and two-photon interference. In these measurements, three excitation schemes are implemented through two distinct free-space setups, shown as Setup 1 and Setup 2 in the figure. A Thorlabs cage system is used in the non-resonant excitation scheme (including the above-band and p-shell excitation) whilst in resonant fluorescence (RF), additional polarization optics are required to reject the pump laser.

3.1 Cryostat

In the experiments presented in this thesis, the quantum dot samples are cooled below 4 Kelvin by using an attoDRY800 helium-based closed-cycle cryostat (see Figure 3.2). Specifically, the cryostat is integrated into a floating optical table with minimized vibrations between the coldhead and the sample space. The compressor, cold head and vacuum pumps are located under the table. The vacuum shroud is located above the table and connected to the cold head via a hole. Inside the shroud, the nanowire sample is mounted on a piezo-based nanopositioner stack that controls the in-plane motion. The objective is mounted on the z-positioner attached at the back of the xy positioners. An apochromatic objective is used which has lower chromatic focal displacement over a broad range of wavelengths compared to a simple aspheric lens, making the alignment robust against different wavelengths. A numerical aperture of NA ≈ 0.81 is chosen to optimize the collection. While the quantum dot sample space is at cryogenic temperature, the external optics are set up outside the shroud on the optical table at room temperature.

3.2 Excitation system

Three typical excitation schemes to populate the charge carriers in the quantum dot systems are above-band excitation, quasi-resonant excitation and strictly resonant excitation, see Figure 3.3.

Above-band excitation generates charge carriers in the bulk material which are subsequently trapped by the quantum dot and relax to the lowest energy levels. The trapped carriers can form excitons which can radiatively decay and produce photons. This excitation process introduces excitation timing jitter, including carrier capture times and relaxation times. In addition, the large number of carriers introduced into the system increases the likelihood of charges trapped close to the quantum dot which can lead to

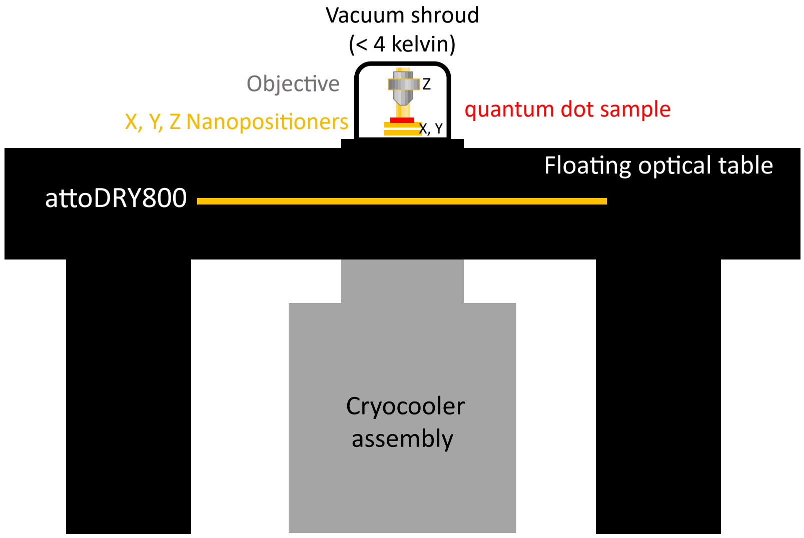

Figure 3.2: Schematic of the He-based closed-cycle cryostat integrated with an optical table. Under the optical table is the cryocooler assembly, and on top of the table is the vacuum shroud containing both the sample and the objective.

greater spectral wandering. For quasi-resonant excitation, charge carriers are directly absorbed into the p-shell of the quantum dot, eliminating some of the effects mentioned above. As the carriers are directly excited inside the quantum dot, the excitation timing jitter and the fluctuations in charge environment are both reduced. In the resonant excitation regime, the excitation energy is tuned to precisely match one of the transitions, and a further reduction in charge noise can be achieved. One of the main challenges of this method is suppressing the excitation laser from the overlapping emission signal as insufficient rejection raises the likelihood of multi-photon emission, degrading the single-photon purity.

3.2.1 Optical setups

The excitation-collection setup for the non-resonant excitation is fully established by using the Thorlabs cage system, as illustrated in Figure 3.4. The fibre-coupled pump laser is coupled into the cage system through a collimator, a silver-coated mirror and subsequently on a dichroic mirror. A dichroic mirror is chosen with a cut-off wavelength such that the laser is reflected and the dot emission is transmitted. Additionally, an imaging system containing two beamsplitters (BS), one with R:T = 10:90 for directing a white light source

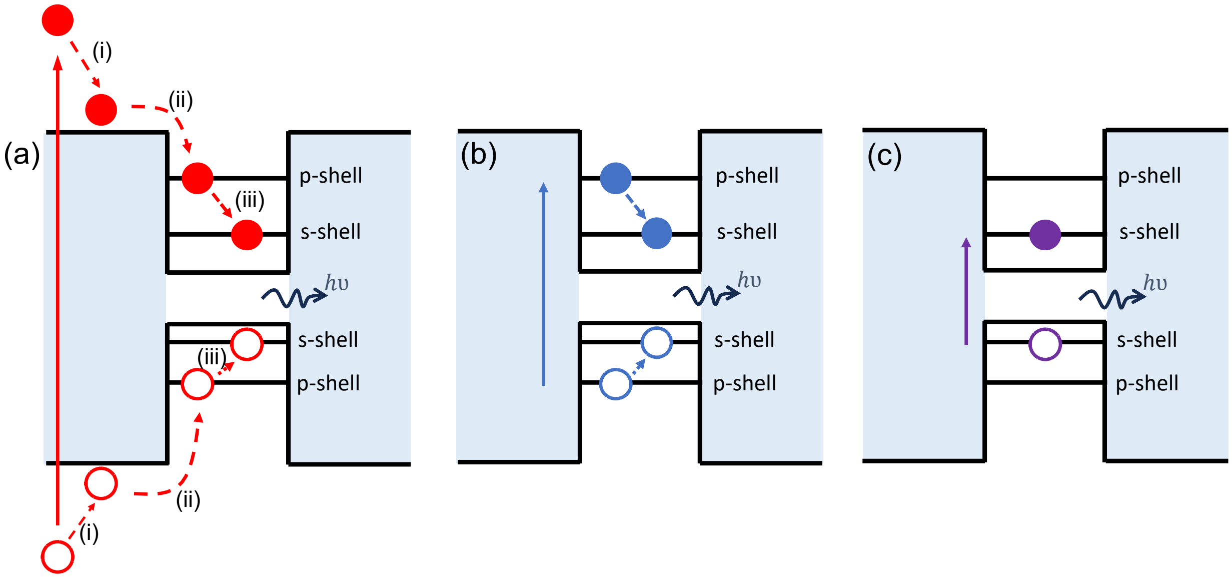

Figure 3.3: Excitation schemes. (a) Above-band excitation, (b) p-shell excitation, and (c) resonant excitation. Solid straight arrows indicate the excitation from the laser and dashed arrows indicate different carrier relaxation processes: (i) relaxation to band-edge; (ii) carrier capture into the dot, and (iii) relaxation to the ground state. Carrier recombination results in the emission of a photon with energy $h\nu$.

to illuminate the sample and a R:T = 50:50 to direct the reflected light to a complementary metal-oxide-semiconductor (CMOS) camera. The imaging system is used to monitor the substrate, helping with system alignment and ensuring only a single dot is excited at a time. The two rectangular plate BSs are mounted on the removable inserts that sit inside two 60 mm cage cubes. After the system is well-aligned, these are removed to maximize the collection during the measurements.

Owing to the difficulty of spectral separation, several methods have been presented to perform resonant excitation on quantum dots to distinguish the laser and the emission signal. One example is to set up orthogonal paths for the pump and collection [62, 79], shown in Figure 3.5(a). In this case, a laser beam is directed in the plane of the quantum dot sample, allowing the dot emission to be collected perpendicular to the sample surface while keeping laser light travelling through the plane. However, it is challenging to apply this technique to the nanowire quantum dot system. First, it is hard to excite the dot from the side of the nanowire due to technical challenges such as optical alignment. Secondly, pumping from above the nanowire will result in almost no emission from the side, as the

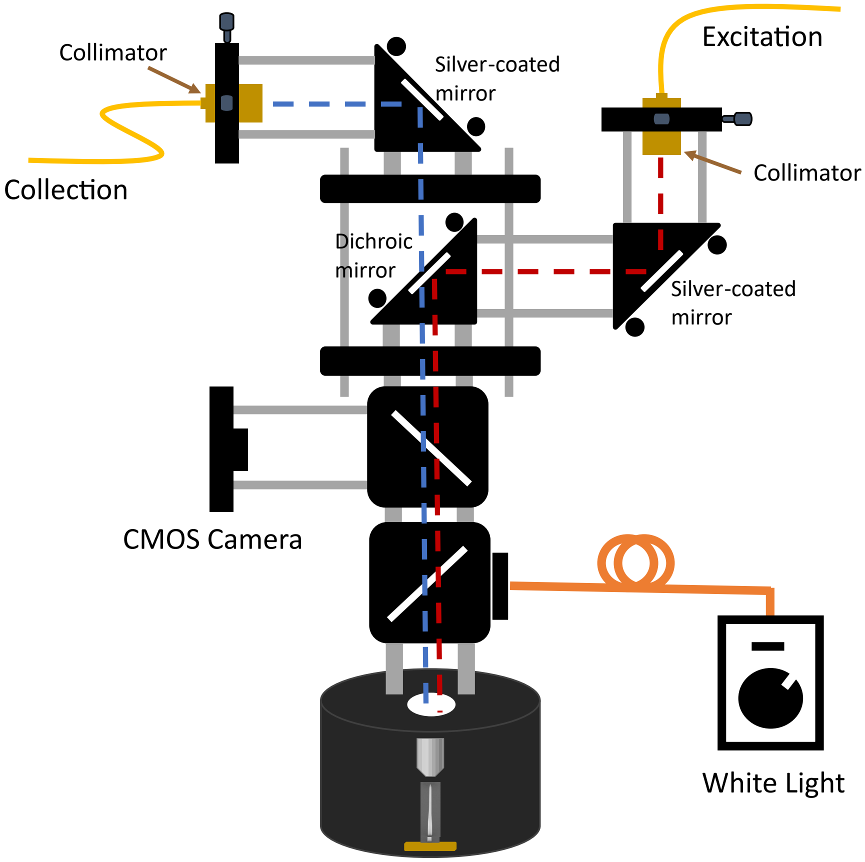

Figure 3.4: Schematic of the cage system setup for non-resonant excitation. The red dashed line indicates the input laser and the blue dashed line indicates the dot emission. The black cylinder represents the sample space where the both objective and sample are placed inside the cryostat.

waveguide geometry is specifically designed to direct the mode either upward or downward along the nanowire, as discussed in the previous chapter. Another example is using two-photon excitation [80], where the energy of each photon is tuned to half of the biexciton energy level, (see Figure 3.5(b)). The laser is therefore able to excite the biexciton and can be optically filtered on the collection path. In this work, we are going to implement a third technique based on the polarization rejection to realize strictly resonant excitation, which has been commonly applied by others [81, 82].

The polarization rejection technique is shown in Figure 3.5(c) where a linear polarized laser with s-polarization is used to excite a quantum dot. Consider the two excitons in the dot as two orthogonal dipoles that can emit in two orthogonal polarizations with random orientation. Depending on the orientation of the dipoles, the laser can excite one or a combination of the two. However, any polarized photon from the dot whose polarization is aligned to the laser will be rejected in the collection path. As a result, optimal signal collection occurs when the dipoles are oriented 45° relative to the laser. This limits collection compared to excitation without polarization-based rejection to 50 %.

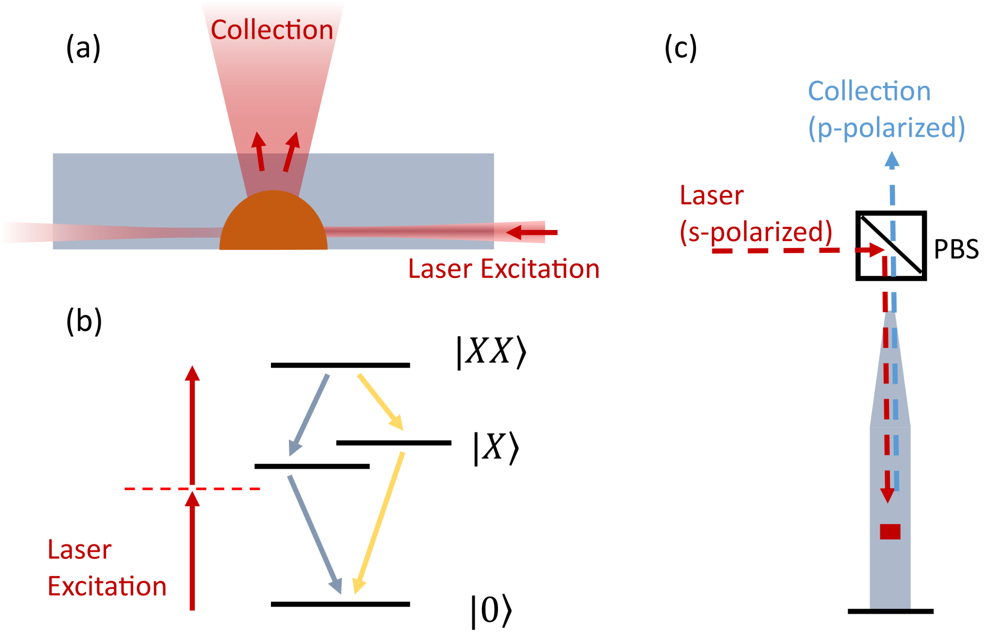

Figure 3.5: Three different resonant excitation schemes. (a) Off-axis excitation on the quantum dot sample. (b) Two-photon excitation to excite the biexciton. (c) Strictly resonant excitation on a nanowire quantum dot using polarization rejection.

A polarization-rejection setup is established in this work (see Figure 3.6) and is based on the work done by Warburton's group [81]. Specifically, a PM single-mode fibre is utilized for guiding the fibre-coupled laser into the free-space setup. The laser is collimated and directed by a dielectric mirror to a linear polarizer (LP). The polarization of the laser is aligned to the s-polarization axis of the polarizing beamsplitter (PBS). The PBS directs the laser through a zero-order quarter-wave plate (QWP) before going into the cryostat to excite the nanowire quantum dot. The QWP and two PBSs in the collection path realize the laser suppression by restricting transmission to the polarization orthogonal to the laser. The same imaging system as the non-resonant setup is used after the BS to observe the spot of the reflected laser [7, 82]. Using this imaging, one can verify the system alignment.

For perfect cross-polarized conditions, one expects the pattern shown in Figure 3.7(a), whilst for the co-polarized case, the image in Figure 3.7(b) should be observed. The dot emission is coupled into the PM single-mode fibre, which acts as a spatial filter for further rejection.

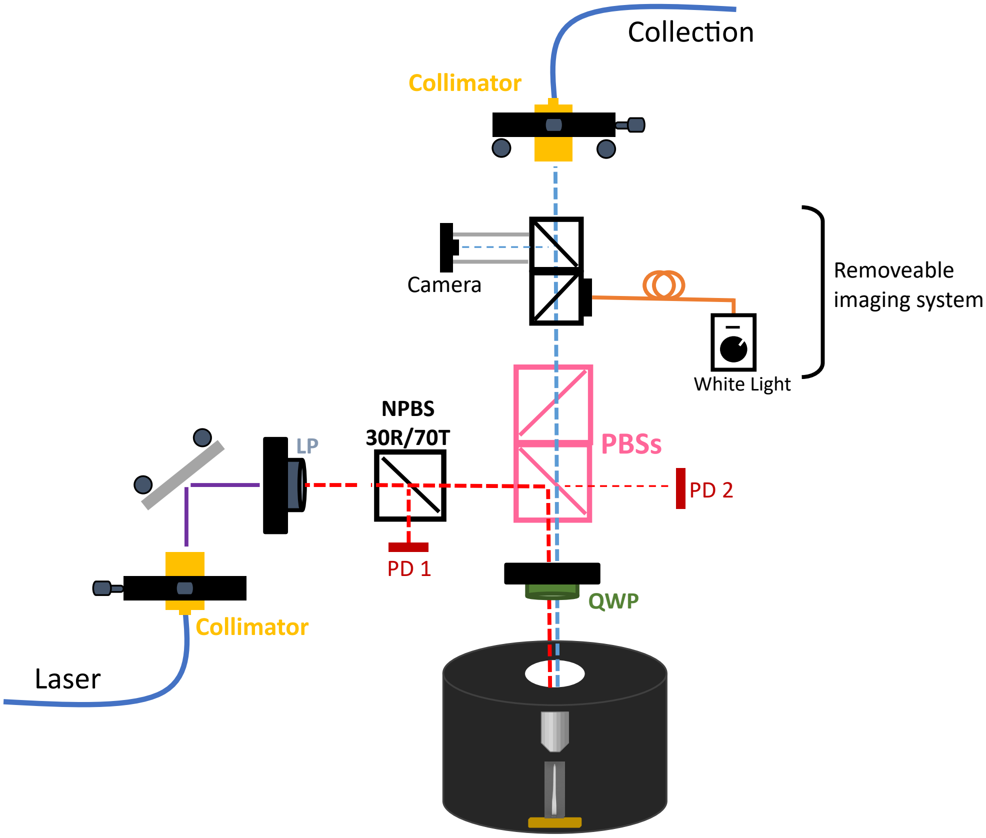

Figure 3.6: Schematic of the experimental setup for RF. The dashed line indicates s-polarization from the laser (red) and the collected p-polarization from the dot (blue). The black cylinder represents the sample space where objective and quantum dots are placed inside the cryostat.

The alignment process starts with the co-linear and confocal configuration of the excitation and the collection paths. For resonant excitation, the collimators for both the excitation and the collection are set to the emission wavelength. Laser light is sent through both the excitation and collection arms of the PL setup. The collimators and beam paths are precisely aligned to achieve perfect overlap and identical focus of both beams on the sample surface, maximizing signal collection efficiency. The LP is mounted on a piezo motor-driven rotator with a minimum incremental move of 1 mdeg and is rotated to align the laser polarization to the s-polarization of the first PBS by minimizing the transmitted power using a photodetector (PD 2). A power control setup with a R:T = 30:70 non-polarizing beamsplitter (NPBS) and PD 1 is additionally set up on the excitation path before the PBS. A p-i-d control program is used to stabilize any input power fluctuations induced by the polarization drift of the laser itself. Any birefringence in the optical path (e.g. from the multicomponent apochromatic objective or the nanowire waveguide geometry) may introduce ellipticity in the polarization. This will result in a degraded laser extinction ratio. To correct for any induced ellipticity, a QWP is inserted between the PBS and the cryostat. Rotation of the QWP is used to regain a linear polarized laser aligned to the s-polarization axis of the PBS.

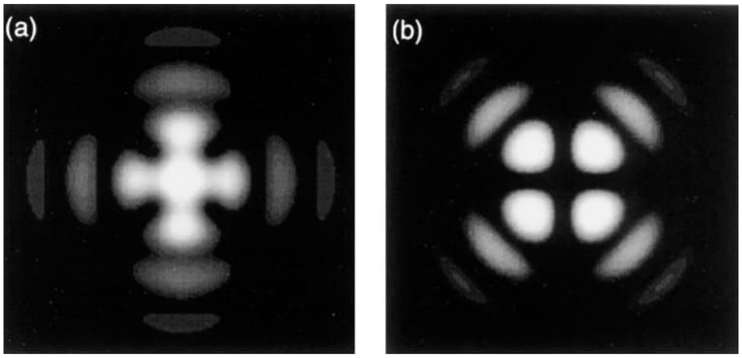

Figure 3.7: Simulated pattern of reflected in-focus laser that is (a) in the direction of the incident polarization and (b) perpendicular to the incident polarization, adapted from [7].

3.2.2 Excitation Lasers

In this work, nanowire quantum dots are excited using continuous-wave (CW) and pulsed lasers. For non-resonant excitation, CW lasers are used for PL spectroscopy, whilst the time-resolved PL and auto-correlation measurements are performed using a pulsed laser with a tunable repetition rate. In RF, a pulsed laser was used in combination with a pulse slicer for both time-integrate and time-resolved PL as well as auto-correlation measurements.

Above-band excitation

- **Thorlab 780 nm CW laser:** This is a Thorlabs FPV785P fibre-pigtailed laser with characterized center wavelength at ∼780 nm. The laser uses a volume holographic grating (VHG) to stabilize the laser diode, providing narrow-bandwidth single-frequency operation. This is achieved by placing a transmission grating with a periodic index of refraction in front of the laser diode output, which only allows the wavelengths satisfying the Bragg condition to be reflected into the laser cavity and reinforces the lasing at a specific wavelength. The laser is further installed in a Newport laser diode mount connected to a current and a temperature control module.

- **PicoQuant 670 nm pulsed laser:** This device contains an LDH-P-C-670 picosecond diode laser head with a pulse width of less than 70 ps and a maximum repetition rate of 80 MHz, along with a PDL 800-D laser driver. The driver can set the power from 0.5 to 2 mW, and a repetition rate from 5 to 80 MHz. It also provides external trigger output and synchronization output at any repetition rate listed above for time-resolved PL measurements.

P-shell excitation

- **Toptica CTL 950 CW laser:** This is a continuously tunable laser with a wavelength scanning range of $910 \sim 990$ nm and a typical linewidth of 10 KHz. It consists of a laser diode featuring a grating at the output of the semiconductor chip. The frequency tuning is achieved by adjusting the external grating. To minimize mode hopping during a wide range of wavelength tuning, the laser uses an active control loop to both analyze the signals in the laser head and optimize the tuning element. In this case, the laser can be tuned with an accuracy ~ 0.1 nm.

Resonant excitation

- **Spectra-Physics Mai Tai pulsed laser:** This is a Ti:Sapphire mode-locked pulsed laser, which is pumped by a continuous-wave 532 nm diode laser. The output pulses have a bandwidth of ∼70 fs and a fixed repetition rate of 80 MHz, and is tunable from 690 nm to 1040 nm in increments of 1 nm.

3.2.3 Pulse slicer

As the ultrafast pulsed laser is used for resonant excitation, the beam has a broad spectral pulse width of around 20 nm. In order to reject the laser more easily, a motorized pulse slicer is used to cut out a narrow bandwidth in the spectral domain from the Mai Tai output pulses before sending them into the optical setup. In the experiments, an A. P. E. pulseSlicer is used for fine-tuning the laser wavelength with a precision of 0.001 nm as well as the spectrum slicing. The wavelength tuning range is 680 nm ∼ 1080 nm with a minimum spectral bandwidth of less than 0.03 nm at a centre wavelength of 950 nm. Figure 3.8 shows a schematic of the slicer components. The output laser beam from the Mai Tai is sent into the slicer (red line) and is subsequently dispersed into its wavelength components using a grating. A motorized slit is used to select the desired part of the spectrum. The mirror behind the slit reflects the sliced beam back to the grating a few millimetres below the incoming beam and out to the output iris (blue line). The output beam is coupled to an SM or PM fibre and delivered to the RF setup.

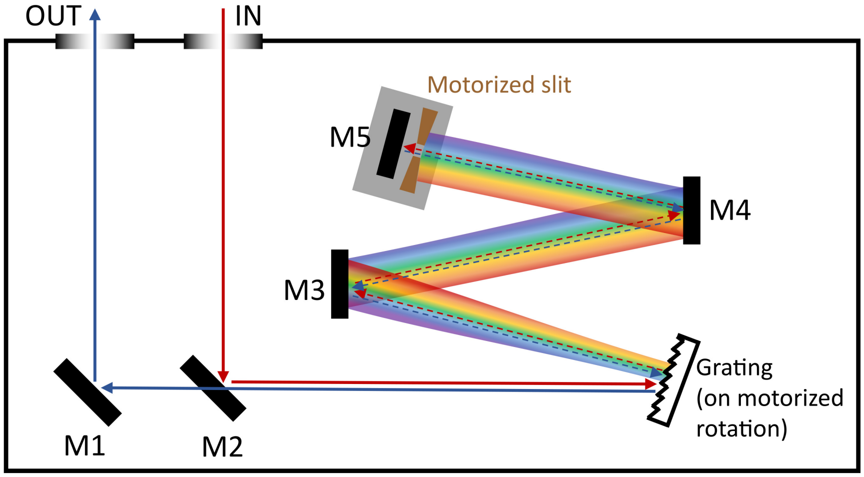

Figure 3.8: Schematic of the pulse slicer. The red line indicates the laser beam directly coming out from the Mai Tai, while the blue line indicates the laser beam after the spectral slicing. The centre wavelength incident on the slit is set by the grating position whilst the spectral width is controlled by the slit width.

3.3 Detection system

3.3.1 Filters

With non-resonant excitation, both the reflected laser from the sample substrate and the emission from the dot will be collected. In order to isolate a single s-shell emission line, two different fibre-based tunable filters are used in the detection path. For the dots emitting around 890 $\sim$ 980 nm, electrically tunable optical filters from WL Photonics Inc. are used. For the dots emitted at the telecom C-band, a manually tunable filter from EXFO is used.

- **WL photonics bandpass tunable filter:** The filters have integrated SM fibres as input and output. When the incoming light is sent into the device, it is diffracted by an integrated grating and is directed to a movable slit that is driven by a motor. By connecting to the computer, a python-based graphical user interface (GUI) is used to precisely control the centre wavelength, the tuning direction and the tuning steps. Based on the emission wavelengths from the dots, two filters with tunable ranges of 890 $\sim$ 950 nm and 920 $\sim$ 980 nm are used, respectively. Both of them have a bandwidth of 0.1 nm.
- **Exfo XTM-50 ultrafine tunable filter:** This filter is used for isolating single emission lines from telecom quantum dots. It is tunable from 1480 nm to 1620 nm and has a tunable bandwidth from 4 GHz to 80 GHz. The filter has integrated mating sleeves to allow for fibre connections. This device is, however, completely manual and it requires using a spectrometer to monitor the tuning process.

3.3.2 Spectrometer

For time-integrated PL spectroscopy of the quantum dot emission, a diffraction grating spectrometer with a 0.75 m focal length is used (Teledyne SpectraPro HRS 750), as shown in Figure. 3.9(a). It contains two entrance ports that are compatible with both fibre-based and free-space setups, as well as two exit ports that allow for connecting two detectors. Inside the spectrometer, an interchangeable triple-grating turret is mounted on a rotation stage. The turret is loaded with three gratings having groove densities of 150 g/mm, 1000 g/mm, 1200 g/mm, allowing different spectral ranges and resolutions. In this work, only the 150 g/mm, and the 1200 g/mm gratings are used. The 150 g/mm grating has a blaze wavelength at 1250 nm, and a spectral range of 80 nm, providing a quick glance of the nanowire device emission across a broad spectral range. The 1200 g/mm grating, is blazed at 1250 nm and has a spectral range of around 22 nm with a resolution of $\sim 25\,\mu$eV, which offers detailed spectra of the s-shell transitions.

Two detectors are used, depending on the emission wavelength. One detector is a thermoelectric-cooled charge-coupled device (CCD) with the name brand PIXIS. It is a 2D array with a size of 1340×100 pixels. The operating temperature is -75°C to minimize the dark current. Additionally, it has over 80% quantum efficiency over a broad spectral range from 400 nm to 930 nm and over 50% efficiency between 930 nm and 950 nm. The second detector is a nitrogen-cooled linear InGaAs photodiode array with 1024 pixels (PyLon-IR). This detector has a quantum efficiency greater than 60 % at 1.5 μm, therefore, and is used to measure the PL spectra of the telecom quantum dots.

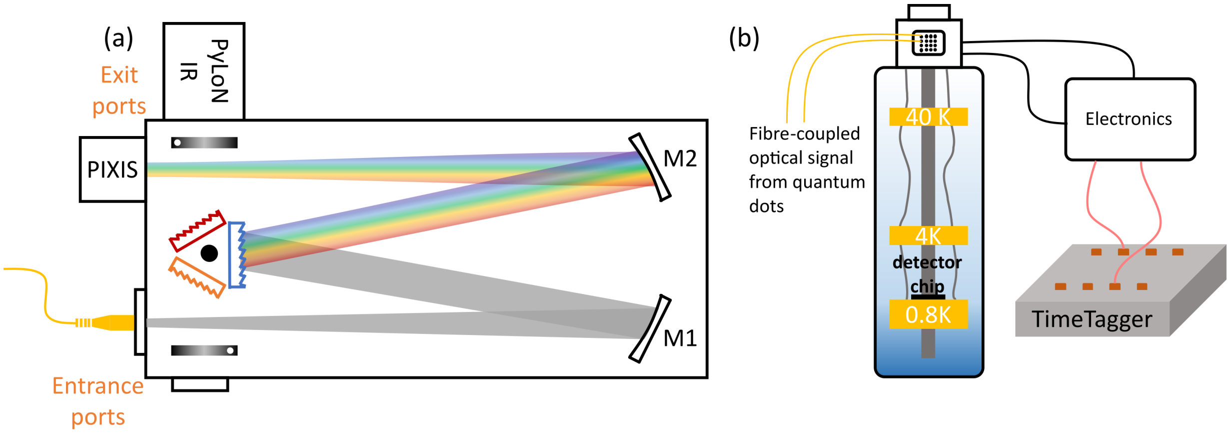

Figure 3.9: Detection systems. (a) Schematic of the spectrometer. The collected light is guided through a SM fibre into the spectrometer, and collimated by a concave mirror (M1) with a focal length of 0.75 m. The collimated beam is then diffracted by one of the three different gratings (coloured in blue, red and orange) and then focused onto either the PIXIS or the PyLoN-IR detector by M2 with the same focal length. (b) Schematic of fibre-based SNSPD with a counting module (TimeTagger).

3.3.3 Superconducting nanowire single-photon detectors

Optical measurements of a single emission line from a quantum dot (e.g. HRPL, TRPL and auto-correlation measurements) are conducted using superconducting nanowire single-photon detectors (SNSPDs)[1] along with a counting module (TimeTagger), see Figure

---

[1] Note that the "nanowire" in the context of SNSPDs refers to thin meanders of superconducting material and is completely different from our nanowire sample.

3.9(b). The detectors are comprised on meandering lines of superconducting material (e.g. NbN) which are cooled to 0.8 K. The lines remain superconducting until a photon hits the meander to break the Cooper pairs. The disruption forms a hotspot and results in a resistive barrier. The sudden increase in resistance generates a voltage pulse that is delivered to the counting module and registered as a photon detection. The resistive barrier will subside rapidly and the meanders will recover to the superconducting state for the next photon [83]. The false detections due to noise are defined as dark counts. The SNSPDs used in the following experiments have jitter time of $\sim 100\,\mathrm{ps}$ and dark counts of 100~300 counts per second.

i. HRPL spectroscopy with a Fabry-Pérot (FP) etalon

Information on the emission linewidth can be extracted using various techniques. For example, linewidths can be obtained by fitting the emission spectrum with a high-resolution spectrometer [84] when the emission lines are sufficiently separate from each other and sufficiently broad to be observed [85]. In recent years, advancements in growth techniques have enabled the production of high-quality quantum dots with linewidths approaching the transform limit [86]: ranging from sub-GHz to a few GHz. Consequently, measurement techniques that have higher resolution and precision are required.

A Fabry-Pérot etalon operates based on multiple-beam interference and can be used to perform high-resolution spectroscopy. This is achieved by measuring the transmission peaks from a high-reflective cavity that consists of two parallel mirrors. Figure 3.10 shows a schematic of such a cavity having two mirrors with reflectivity R, placed in parallel at a distance L. When light with electric field amplitude E_0 is incident on the left mirror at an angle θ, a portion of the light transmits into the cavity and propagates to the right mirror. Due to the high reflectivity, only a small portion of the light (E_1) transmits through the mirror whilst the rest is reflected back. Inside the cavity, multiple reflections result in an equal phase delay between each round trip. The path length difference between the subsequent output beams can be expressed as:

$$\Delta d = 2L\ cos(\theta) \tag{3.1}$$

The power transmission function ($T(\nu)$) is given by the square of the field transfer function ($H(\nu)$) which is the ratio between the transmitted amplitude of the optical field after N roundtrips and that of the incident field [87]:

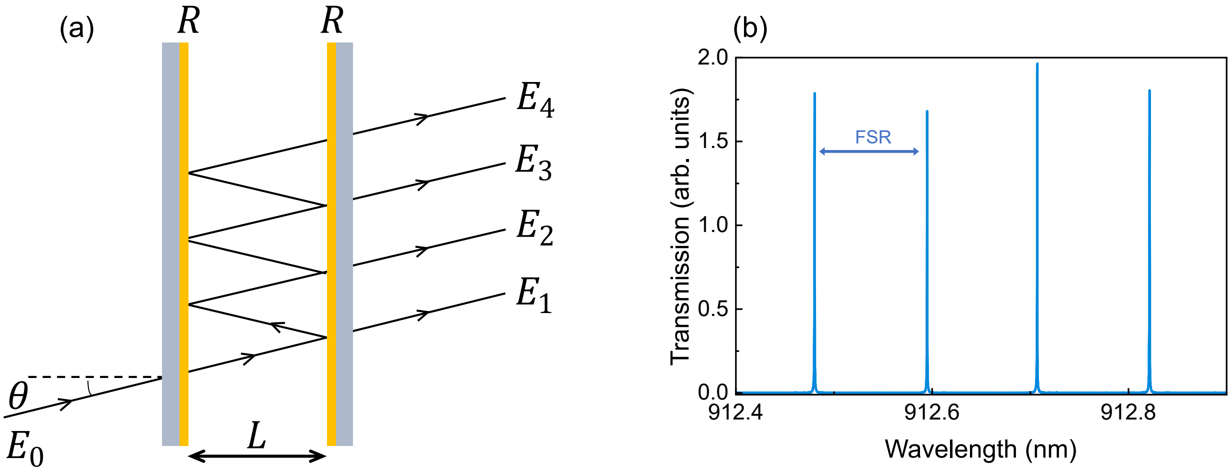

Figure 3.10: (a) Schematic of an etalon, with a light beam E_0 incident on the left plate. Multiple reflections happen inside the cavity, indicated by the arrows. The transmitted peaks after each round of reflection are labelled as E_i where $i = 1, 2, 3, 4$. (b) An exemplar transmission as a function of wavelength. The transmission spectrum is measured by scanning the Toptica CTL laser through the fibre-based FP etalon.

$$T(\nu) = |H(\nu)|^2 = \left|\frac{E_N(\nu)}{E_0(\nu)}\right|^2 = \frac{(1-R)^2}{(1-R)^2 + 4R\ sin^2(\frac{2\pi\nu}{2c} n\Delta d)} \tag{3.2}$$

where ν is the frequency of the light, n is the index of refraction of the cavity[2]. The transmitted field is maximized when the path difference between the two consecutive reflections matches the integer number of wavelengths. In the case where the light is incident perpendicular to the input mirror (i.e. $\theta = 0$), Eq 3.2 is simplified to:

$$T(\nu) = \frac{(1-R)^2}{(1-R)^2 + 4R\ sin^2(\frac{2\pi\nu}{c} nL)} \tag{3.3}$$

The free spectral range (FSR) is defined by the separation between the transmitted peaks, as shown in Figure 3.10(b). It can be expressed as $\Delta\nu_{FSR} = c/2nL$. Furthermore, the full-width half maximum (FWHM) of the transmission peak (i.e. the bandwidth) can be calculated by using the small angle approximation[3]:

---

[2] Note that it is not the index of refraction for the mirror but the material in between.

[3] $sin(\theta) \approx \theta$

$$\Delta\nu = \frac{c(1-R)}{nL\sqrt{R}} \tag{3.4}$$

For the experiments presented in this thesis, precise measurements on linewidths are performed using a fibre-based scanning Fabry-Pérot etalon, as shown in Figure 3.11. This device is designed based on the piezoelectric effect. It employs a cavity formed by two coated fibre ends placed in-plane on a piezoelectric material. When a direct voltage is applied by the external electronics onto the piezo material, its length will be expanded, leading to a small change in the cavity length, thereby providing scanning capabilities. By measuring the transmission with an SNSPD, a HRPL spectrum of a single emission line can therefore be obtained.

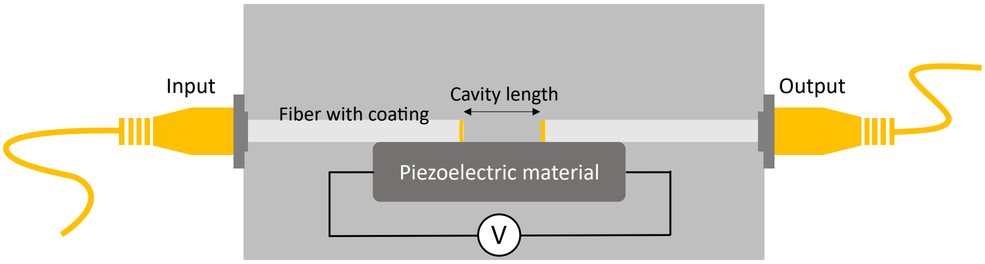

Figure 3.11: Schematic of the fibre-based etalon used for the linewidth measurements, composed of two fibres with coated facets facing each other to form the cavity.

ii. TRPL measurements

As mentioned in section 2.3, radiative lifetime is defined as the time it takes for an exciton to decay radiatively, emitting a photon. Single-photon generation is sequential, meaning that a new photon cannot be produced until the previous recombination process is complete. Therefore, a shorter exciton lifetime indicates a higher photon generation rate. To measure the lifetime, we use the time-correlated single-photon counting (TCSPC) method.

In this measurement, a pulsed laser is used to both excite the quantum dot and generate a trigger signal for the TimeTagger, initializing the counting event. The arrival of the photon from a single emission line is then recorded as a "stop" after the laser "start" signal. By collecting the data from many such detection events, a histogram of photon arrival times relative to the trigger signal is constructed. Figure 3.12(a) shows an exemplary result from the lifetime measurements. The radiative decay lifetime can be extracted by fitting the experimental data with the function [88]:

$$I(\tau) \propto e^{-(\tau-\tau_d)/\tau_r}\left[erf\left(\frac{\tau-\tau_d}{\sqrt{2}\sigma}\right)+1\right] \tag{3.5}$$

where τ_d is an offset delay time, τ_r is the radiative decay time. The $erf()$ is the error function with a rise time of $\sqrt{2}\sigma$ originating from the instrumental response function and the excitation timing jitter.

iii. Auto-correlation measurements

From section 2.2, we outlined that single-photon purity is a crucial metric for evaluating the performance of a single-photon source and that is determined through auto-correlation measurements. In these experiments, a fibre-based HBT setup is utilized. The isolated single exciton emission is passed through a 50:50 fibre BS, directing photons to two SNSPDs. The TimeTagger records the time delay between one photon being captured by one detector (used as the "start") and the sequential detection on the other detector (as the "stop"), which constructs a bi-directional histogram, showing the correlation between detection events.

When single photons are produced from quantum dots, they can only take one path through the splitter and so can only arrive at one detector. This means that for a perfect single-photon source, the probability of detecting photons on both detectors at zero time delay (i.e. at the same time) is zero. When a CW laser is used to excite the system, one will observe a gradual decrease in the coincidence counts near the zero delay meaning a decreasing probability of detecting two photons close to the same time. A dip will therefore form at the zero delay. If a pulsed laser is utilized, the probability of simultaneously detecting photons at two detectors is highest at the time of each pulse, resulting in peaks appearing at intervals that match the repetition rate of the laser.

Figure 3.12(b) and (c) respectively show exemplary simulations of ideal $g^{(2)}(\tau)$ measurements under CW and pulsed laser excitation. The fitting functions for the two cases are expressed as [89, 6]:

$$g^{(2)}_{CW}(\tau) = 1 - e^{-|\tau|(1/\tau_r+R)} \tag{3.6}$$

$$g^{(2)}_{pulsed}(\tau) \propto g^{(2)}(0)e^{-|\tau|/\tau_r} + \sum_{n\neq 0} e^{-|\tau+NT|/\tau_r} \tag{3.7}$$

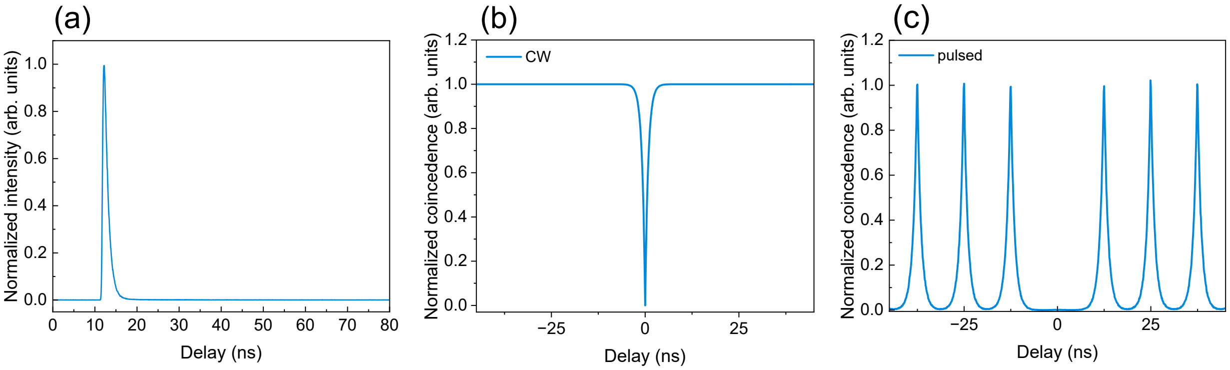

Figure 3.12: Examples of (a) a lifetime measurement and auto-correlation measurements under (b) CW excitation or (c) pulsed excitation.

where τ_r is the radiative decay time, R is the excitation rate, N is the number of pulses, and T is the pulse period. In Eq 3.7, the first term represents the correlation near zero-delay, accounting for the possibility of multiphoton detection which can happen in both above-band and resonant excitation. The second term corresponds to all the side peaks occurring at $\pm nT$.

iv. Hong-Ou-Mandel interferometry

As mentioned in the section 2.2, the indistinguishability between two photons can be measured based on the HOM effect and is quantified by the visibility of the two-photon interference, expressed as [89]:

$$V(\tau) = \frac{g_{\perp}^{(2)}(\tau) - g_{\parallel}^{(2)}(\tau)}{g_{\perp}^{(2)}(\tau)} \tag{3.8}$$

where $g_{\parallel}^{(2)}(\tau)$ measures the correlation between two interfering photons with the same polarization and $g_{\perp}^{(2)}(\tau)$ measures the correlation when they are cross-polarized. In this work, this is conducted using a Mach–Zehnder interferometer (MZI) setup involving both free-space optics and fibre connections, as shown in Figure 3.13.

Using pulsed excitation, a sequence of photons emitted from the dot is launched from a PM fibre and subsequently split into two paths by a PBS cube. A half-wave plate (HWP 1) is placed in front of the PBS to equalize the intensity between the two paths by rotating the polarization. The photons with s-polarization will be reflected and hit the retroreflector that is mounted on a linear delay stage. These are back reflected from the dielectric mirror, returning to the PBS through the same path. The QWP in this path is used to rotate the polarization of the beam from s to p for maximum transmission through the PBS. On the other path, the photons with p-polarization directly pass through the PBS. The photons coming from the two paths are then sent into the two arms of the fibre-coupled BS with another two half-wave plates being placed before the collimators. While one of them (HWP 2) is used to align the photon polarization of incoming photons to the slow axis of the PM fibre, the other one (HWP 3) allows for a change of the polarization of the two interfering photons from parallel to perpendicular to each other. The outputs of the second BS are connected to two SNSPDs and the TimerTagger as in the HBT setup.

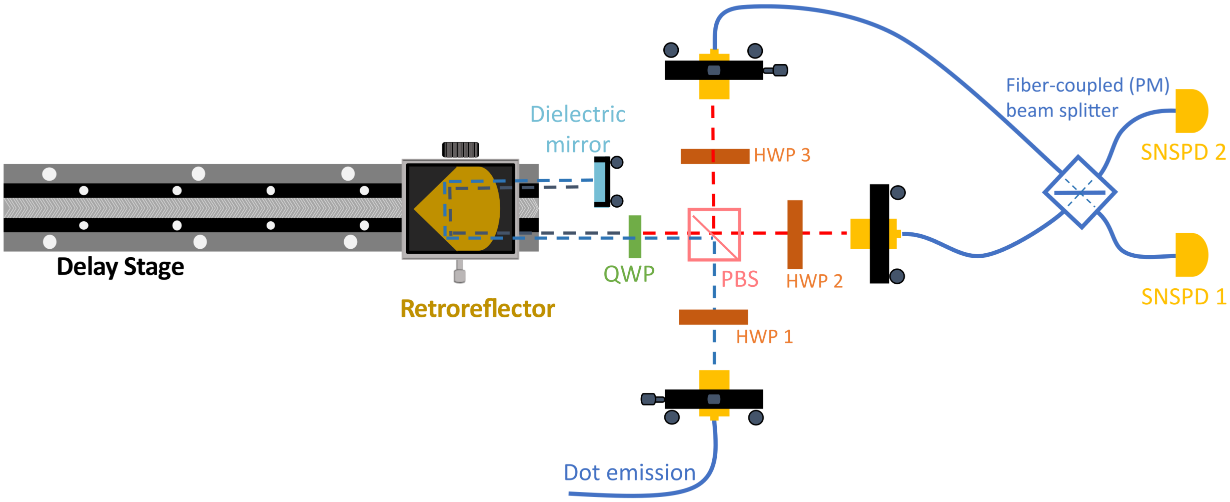

Figure 3.13: MZI setup for the two-photon indistinguishability measurements. The first half of the setup uses free-space optics with a PBS. The temporal alignment is achieved by using a delay stage to match the separation of the excitation pulses. The second half uses a fibre-coupled BS avoiding spatial misalignment of the two interfering photons.

The position of the retroreflector is determined by matching the separation between sequential pulses. By sending the excitation pulses directly to the input of the MZI, one can observe the path difference on the time-resolved PL after the first PBS, presenting as a time delay between two sequences of peaks. To match the delay, we can move the retroreflector while monitoring the change in one sequence, until the two completely overlap with each other. The polarization of the two interfering photons is determined by measuring the outputs of the first PBS on a polarimeter. Ideally, when the interfering photons from the same emission peak are set to be co-polarized, they are indistinguishable from each other and will always exit through the same port, as shown in Figure 2.3. This leads to $g_{\parallel}^{(2)}(0) = 0$. However, if the two photons are cross-polarized, there is only a 50% probability that they will exit through the same port, hence $g_{\perp}^{(2)}(\tau) = 0.5$. The visibility, $V(\tau = 0)$, is bound between 0 and 1, where 0 indicates perfectly indistinguishable photons and 1 means that the photons are completely distinguishable.

Chapter 4

Optical Properties of Quantum Dots with Non-resonant Excitation

Section 2.4 discussed the growth techniques of nanowire quantum dot samples. In general, disk-shaped quantum dots embedded within nanowires are grown on patterned substrates, enabling site-controlled epitaxial growth. The design of the nanowire waveguide can optimize the coupling efficiency of the dot emission into the fundamental mode of the waveguide, allowing efficient collection from the top. Additionally, I have highlighted the effects of growth conditions on the optical properties, as variations in confinement energy within the dots result in different emission wavelengths.

In the first half of this chapter, I will provide an overview of the optical properties of three different quantum dots, each grown under different conditions as detailed in Figure 2.14. By using above-band or p-shell excitation, emission spectra, the radiative lifetimes and single-photon purities were measured. In this part, the experiments were performed by me independently, including the dree-space optical setup (see Figure 3.4), the PL spectra, the TRPL and the auto-correlation measurements. I also analyzed and plotted the data presented in this part independently.

While the typical design of the nanowire quantum dots realizes tunable wavelengths from 890 nm up to 1 μm, with such dots proven to be promising single-photon sources [90], it is beneficial to extend the single photon emission to telecom wavelengths for future applications, such as long-distance communications. In the latter half of this chapter, I will present a nanowire quantum dot device emitting in the telecom C-band by incorporating a modified structure, namely the dot-in-a-rod structure. There, an overview of the dot-in-a-rod growth technique will be provided, followed by the typical optical characterization of this sample using only the above-band excitation. These experimental results are covered in a recently published work entitled ***Single photon emission in the telecom C-band from nanowire-based quantum dots*** [78], where all the work was equally contributed by Andrew and me.

4.1 Spectroscopy

The PL spectra are acquired using the SpectraPro HRS 750 spectrometer equipped with a PIXIS detector where the 1200 g/mm grating is chosen for higher resolution. Two excitation lasers are employed for different excitation regimes: the Thorlabs 780 CW laser for above-band excitation, and the Toptica CW tunable laser for p-shell excitation. By using the 780 nm CW laser, Figure 4.1 presents the s-shell emission spectra of the dots from samples A, B and C, each showing multiple peaks under the two excitation powers. The identification of the dominant peaks is based on the systematic analysis by Laferriére *et. al* [91] and are labelled in the plots as excitons (X), biexcitons (XX) and charged excitons (X^-). Since different complexes saturate at different powers [92], spectra were recorded at a saturation power ($\mathrm{P_{sat}}$) for X^-, as well as at 0.5 $\mathrm{P_{sat}}$, to optimize observation of these complexes. Results across the three samples show that at lower power, the X^- or X peaks are dominant, while the intensity of the XX emission notably increases as the power is doubled. Such a difference in power dependence between X^-, X and XX is expected, see [91].

In sample A, several emission peaks appear in addition to the labelled excitonic emissions, though identifying each of them is not trivial. These emission lines likely originate from carriers occupying higher energy states, forming different charge complexes and charge configurations. In contrast, the emissions from samples B and C are much cleaner, even at the $\mathrm{P_{sat}}$, suggesting more consistent charging of the quantum dots. However, in sample B, the XX emission appears at the left of the X (i.e. at higher energy) compared to samples A and C. This has also been observed and reported in previous work, known as unbounded XX [93, 75]. This shift is likely due to a much higher aspect ratio of this dot ($H_{dot}/D_{dot} \approx 1$), as opposed to the aspect ratios in the other two dots. Despite these variations, the energy spacing between the X and the X^- consistently remains around 6 meV, in agreement with the previous systematic study of the emission spectra [91].

Next, we perform p-shell excitation on sample A using the Toptica tunable laser. Figure 4.2(a) shows a zoomed-in spectrum of the p-shell emission from this dot under the above-band excitation. The p-shell emissions range from approximately 942.26 nm to 947.49 nm and more lines are observed as compared to the s-shell emission. This is consistent with

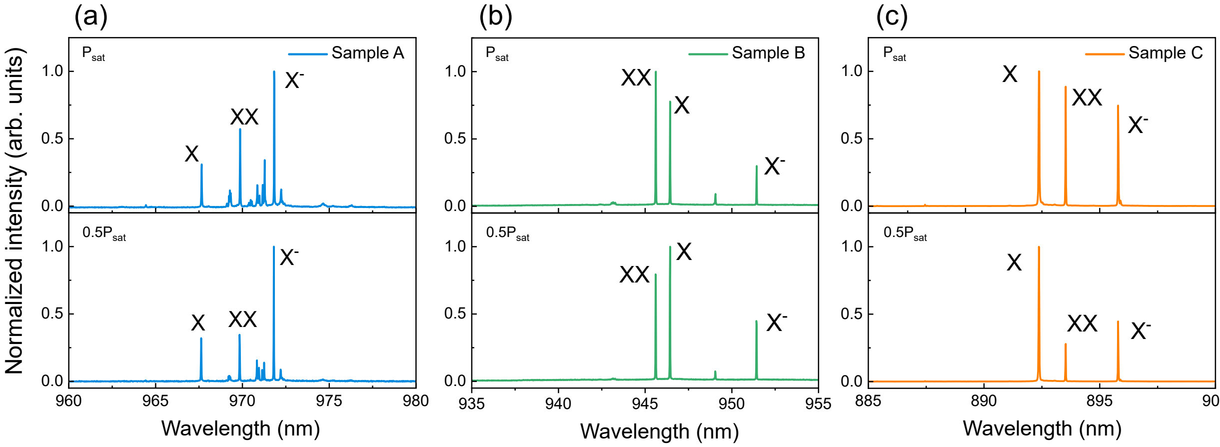

Figure 4.1: Normalized PL spectra of the s-shell emission from the quantum dot in (a) sample A, (b) sample B, and (c) sample C. The upper panels show the spectra at the saturation power P$_{\text{sat}}$ for the X^-, while the lower ones are recorded at half of the P$_{\text{sat}}$.

the symmetry of an interacting 2-D strongly confined system where higher complexity in the p-shell levels provides more recombination pathways than the s-shell.

While scanning the laser through the p-shell and monitoring the ground state emissions on the spectrometer (i.e. photoluminescence excitation (PLE)), one can identify p-shell levels associated with specific s-shell transitions. A pumping wavelength at 948.50 nm is identified as optimal for generating the brightest X^- emission. In this case, the p-shell excitation is less efficient than the above-band excitation as a significantly higher power is required to saturate the X^-. This high excitation power is associated with strong background emission, observed in Figure 4.2(b).

4.2 TRPL: lifetime measurements

The radiative lifetime of an exciton is defined as the time it takes for the electron-hole pair to recombine and emit a photon. This limits the emission rate of a single-photon source. Interactions between the dot and its environment (e.g. charge fluctuations and phonon scattering) can degrade the indistinguishability and coherence of the emitted photon through energy and phase relaxation processes. Therefore, a shorter lifetime compared to the timescale at which spectral wandering and dephasing occur is desired for single-photon sources to maintain a high repetition rate and coherence.

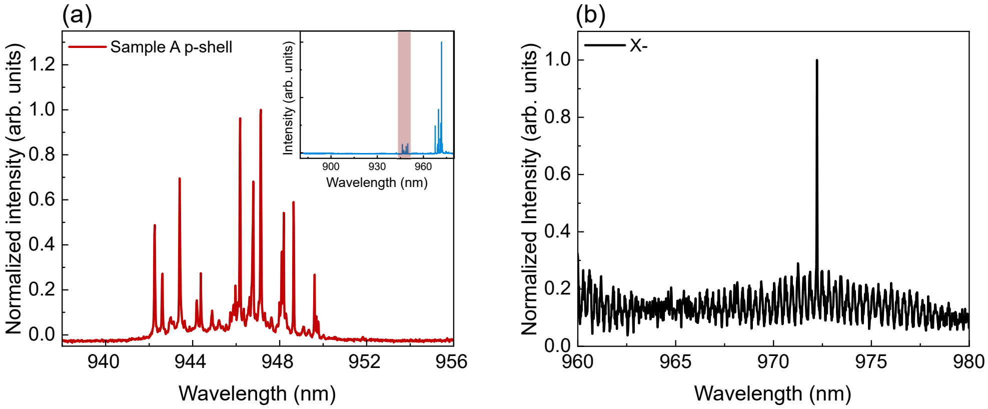

Figure 4.2: (a) P-shell spectrum from sample A. The inset shows the full spectrum with the p-shell highlighted. (b) The s-shell spectrum under p-shell excitation shows just X^- emission line.

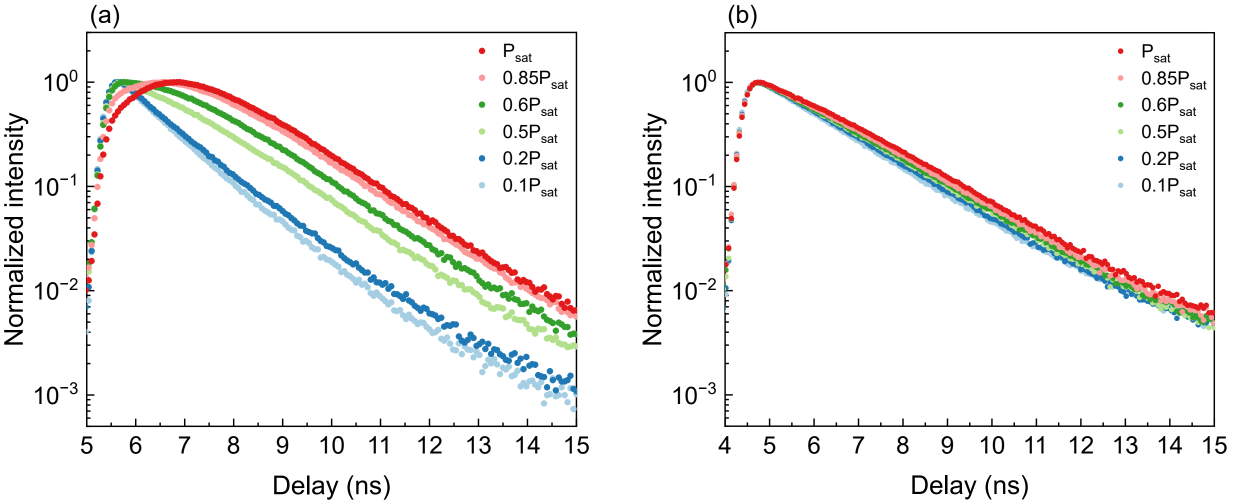

Figure 4.3: Power-dependent lifetime measurements plotted in a semi-log scale under (a) above-band excitation and (b) p-shell excitation.

The radiative lifetime can be obtained by performing the time-resolved photoluminescence measurements using a pulsed laser. The experimental results of lifetime measurements of the neutral exciton, X, from sample A dot are shown in Figure 4.3. Using a pulsed laser with a repetition rate of 80 MHz, the dot was pumped using both above-band and p-shell excitation. The measurements are conducted under six different powers in the two excitation schemes, all showing a monotonic decay of the neutral exciton. This means that only the bright states are observed at cryogenic temperature without applying external fields. In general, observation of the dark exciton is due to a spin-flip process of the electron or the hole, which is slower than the radiative decay of the bright states and requires a much longer time for it to be observed as a second decay [94].

When the dot is excited above the bandgap, free electron-hole pairs are generated in the materials surrounding the quantum dot, i.e. in the conduction and valence band of the InP bulk material. It takes time for these carriers to be captured in the quantum dot and recombine. A higher excitation power leads to overfilling the charges in the higher energy levels of the quantum dot. This can limit the observation of the ground state emission, manifesting as a delay in the excitation process, as shown in Figure 4.3(a). Such delays are less obvious with p-shell excitation (see Figure 4.3(b)), as the free carriers are generated directly in a higher energy level of the quantum dot.

	above-band		**p-shell**	
Power	$\sqrt{2}\sigma$ (ns)	τ_r (ns)	$\sqrt{2}\sigma$ (ns)	τ_r (ns)
$0.5\,\mathrm{P_{sat}}$	0.187	1.038	0.194	1.090
$0.6\,\mathrm{P_{sat}}$	0.251	1.154	0.195	1.120
$0.85\,\mathrm{P_{sat}}$	0.555	1.123	0.196	1.122
$\mathrm{P_{sat}}$	0.715	1.053	0.199	1.170

Table 4.1: "Rise" ($\sqrt{2}\sigma$) and "decay" (τ_r) time for different excitation powers and different excitation methods extracted from a model fit using Eq 3.5.

By fitting each decay curve with Eq 3.5, both the "rise time" (corresponds to $\sqrt{2}\sigma$) and the "decay time" (τ_r) using different pumping schemes and powers are extracted, as summarized in Table 4.1. While the extracted rise times for above-band and p-shell excitation are consistent at $0.5\,\mathrm{P_{sat}}$, they diverge as the excitation power increases, as expected. However, the model fits yield different values of decay times for the two pumping schemes at different powers. This outcome contradicts expectations, as the radiative lifetime is an intrinsic property of an exciton and should remain independent of the excitation methods. One explanation is that the fitting model oversimplifies non-resonant excitation schemes by independently parametrizing the excitation jitter and the radiative decay time. In other words, the radiative lifetimes appear to be correlated with excitation timing jitter under non-resonant pumping, necessitating a more sophisticated model to extract these values accurately.

4.3 Single-photon purity: auto-correlation measurements

Section 2.2 highlighted that single-photon purity is one of the most important metrics for examining the performance of single-photon sources and is measured using an HBT setup. In the auto-correlation measurement, the 670 nm pulsed laser at a repetition rate of 40 MHz was used to excite the dot from sample C. The fibre-based tunable filter was used to isolate the X photon before directing the emission to the SNSPDs. Figure 4.4 presents the experimental result of the $g^{(2)}(\tau)$ measurement using an excitation power at P_{sat} (blue symbols). The model fit (black line) is used to obtain the coincidence counts in the zero delay peak, i.e. the $g^{(2)}(0)$ value. It uses a stochastic model to simulate the excitonic emission and detection process. Specifically, re-excitation of the quantum dot within one laser pulse is modelled as a competition between the band-edge decay rate, the carrier capture rate into the dot, and the radiative decay rate of the dot [95, 96]. Figure 4.4 shows a well-matched simulation with the experimental data, obtaining a $g^{(2)}(0) \approx 0.01$. This value is similar to previous measurements on nanowire quantum dot systems [90].

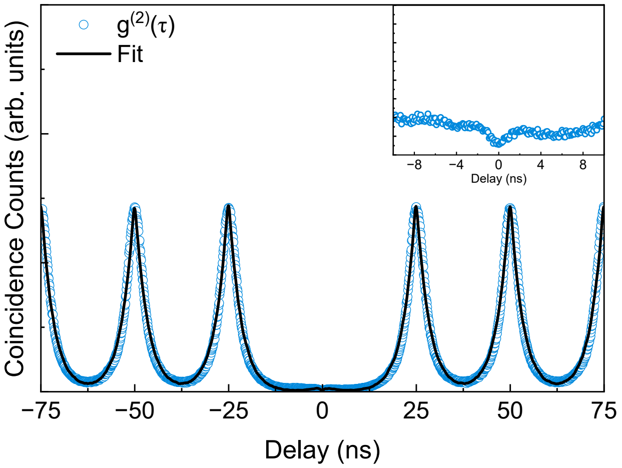

Figure 4.4: Auto-correlation measurement using above-band excitation. The circles are the experimental results and the black curve indicates the model fit. The insert plot shows coincidence counts around zero delay.

The inset of Figure 4.4 shows a zoomed-in plot around zero delay. One can observe a dip at $\tau = 0$ where detected coincidences are nearly zero, indicating that the probability of simultaneously detecting photons on the two detectors is negligible, i.e. high single-photon purity. Note that the side peaks at $\tau = NT$ ($N > 0$) are broadened by the excitation timing jitter, each shown as a Gaussian convolved Laplacian distribution. This broadening results in a raised background, manifesting as tails between the side peaks, as well as on both sides of the dip at $\tau = 0$. Consequently, the side lobes usually observed around $\tau = 0$ in above-band excitation (i.e. the re-excitation process) are hidden in the background (see inset), making it difficult to accurately extract coincidences in the zero delay peak. Possible solutions to minimize the excitation timing jitter are either decreasing the excitation power or reducing the pulse repetition rate, to obtain a more accurate and potentially lower number of coincidences in the zero delay peak.

4.4 Towards Telecom C-band Emission

Silica-based optical fibres have become the backbone of telecommunications due to their significant advantages over traditional electric means. High bandwidth, high security, low signal loss and reduced single interference are the key attributes of long-distance data transmission. While the O-band ($\lambda : 1260 - 1360\,\text{nm}$) is the first wavelength band utilized for telecommunication for its low signal attenuation and dispersion, telecom C-band ($\lambda : 1530 - 1565\,\text{nm}$) is recognized for providing the lowest loss window for long-haul transport applications [97]. Therefore, achieving high compatibility with terrestrial fibre networks is one of the long-term objectives for the development of single-photon sources.

InAs-based quantum dots have shown significant potential for on-demand operation near the telecom C-band [98, 99]. Current platforms primarily utilize Stranski–Krastanov nucleation or droplet epitaxy for quantum dot growth, resulting in randomly positioned dots on the substrate. In contrast, I will present a source based on a position-controlled nanowire quantum dot that achieves single-photon emission in the telecom C-band. As previously discussed, the emission wavelength of nanowire quantum dots can be tuned from 900 nm up to 1 μm by varying the dot size and the As concentration. Here we modify the nanowire quantum dot geometry and the As flow rate to extend the s-shell emission to ≈ 1530 nm.

4.4.1 Dot-in-a-rod structure

The SA-VLS technique mentioned in section 2.4 offers a position-controlled growth of quantum dots via patterning the substrate prior to the epitaxial growth. Using InAsP quantum dots with low As concentration, tunable emission energies were demonstrated through the modifications of the dot confining potential. While a larger aspect ratio of the quantum dot (H_{dot}/D_{dot}) helps to push the emission to longer wavelengths, a significant reduction in emission efficiency hinders the performance of the devices [76].

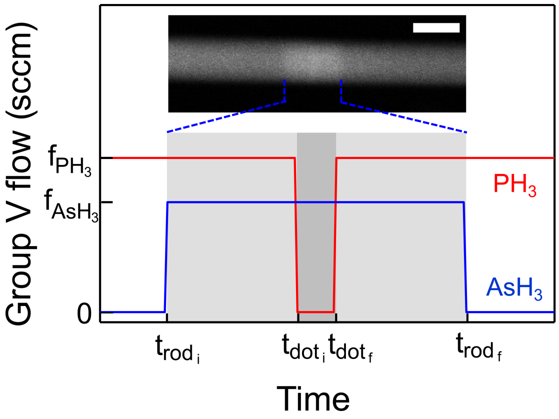

Figure 4.5: Plots of the flow rate of AsH_3 (in blue) and PH_3 (in red) as a function of growth time. The rod is represented by the light grey region and the dot is shown as the darker grey region. The inset shows a transmission electron microscopy (TEM) image of the grown structure.

The DROD structure has been implemented in previous work to obtain bright emission [77]. To grow this structure, AsH_3 is introduced into the reactor while maintaining the PH_3 flow. This is done after the growth of an InP nanowire core base and so forms a section of $InAs_yP_{1-y}$ rod at the top of the base. Subsequently, the PH_3 flow is interrupted to grow the $InAs_xP_{1-x}$ dot with a higher As concentration i.e. $x > y$. The nanowire core is then capped with another section of $InAs_yP_{1-y}$. Figure 4.5 shows the switching sequence of the group V material for growing the DROD structure. The thickness of the whole structure is determined by the growth time $t_{DROD} = t_{rod_f} - t_{rod_i}$, and the thickness of the dot is determined by $t_{dot} = t_{dot_f} - t_{dot_i}$. The DROD structure is in the nanowire core and is clad with an InP shell and grown to a height of 10$\sim$15 μm with the top tapered as before. To optimize the coupling of the spontaneous emission from the dot into the fundamental mode of the nanowire waveguide, a nanowire waveguide base diameter of $320 \sim 390$ nm is targeted to keep $D/\lambda \approx 0.25$.

As summarized in Table 4.2, we implement the DROD structure with different As concentrations and growth times for the rod and the dot to grow four different samples. All samples are grown using a PH_3 flow rate of $f_{PH_3} = 2$ sccm. Sample I through III have dots grown for $t_{dot} = 3.5$ s corresponding a thickness of $\sim$ 3.5 nm from transmission electron microscopy (TEM) measurements. These are embedded in rods grown for $t_{rod} = 17.5$ s corresponding to a total rod thickness of 20 nm. Sample I through III have incrementally increasing AsH_3 flow rates, f_{AsH_3}.

Sample	f_{PH_3} (sccm)	f_{AsH_3}(sccm)	t_{rod} (s)	t_{dot}(s)
I	2	1	17.5	3.5
II	2	1.5	17.5	3.5
III	2	2	17.5	3.5
IV	2	1.5	20.5	6.5

Table 4.2: Summary of the growth conditions for four different samples. f_{PH_3} and f_{AsH_3} indicate the flow rates of the group V materials, in units of standard cubic centimetre per minute (sccm). t_{rod} and t_{dot} are the growth times of the rod and the dot, respectively.

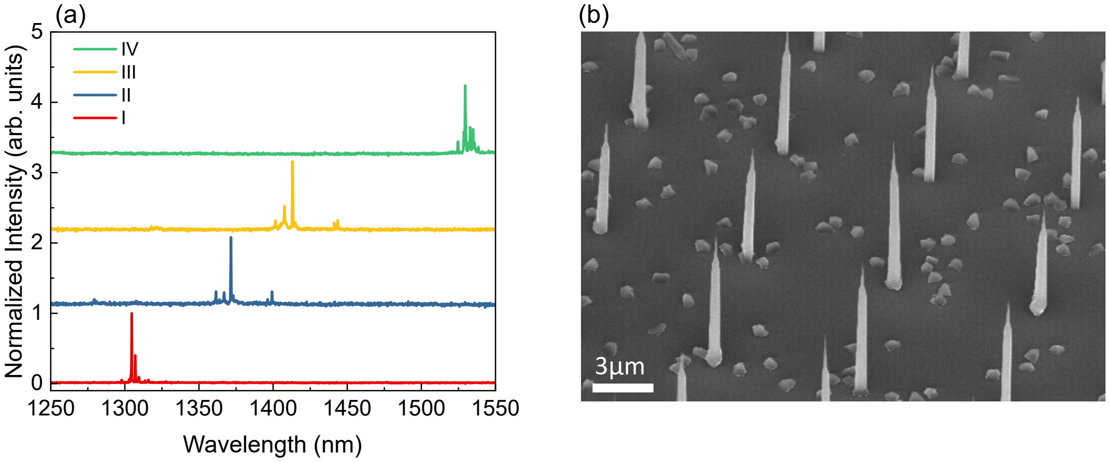

Figure 4.6: (a) PL spectra from each sample measured at excitation powers close to saturation, showing a wavelength shift from 1300 nm to 1530 nm. (b) SEM image imaged at 45° of an array of nanowires corresponding to sample D.

As studied in [74], an increase in As concentration will lead to a decrease in the band gap, hence a red shift in wavelength. As can be seen from Figure 4.6(a), the magnitude of the redshift per unit increase in AsH_3 flow diminishes. Therefore in sample IV, the AsH_3 flow is kept the same as for sample II but the growth time of the dot is increased to 6.5 s. The resulting decrease in confinement shifts the emission wavelength to the telecom C-band. Figure 4.6(b) is an SEM image of sample IV taken at 45°, showing an array of nanowires pitched at 7.5 μm. Based on the image, we measure a nanowire base diameter $\sim$ 490 nm. The parasitic growth observed on the oxide surface is a consequence of insufficient selectivity and is typically observed when growing structures requiring AsH_3 flows for more than a few seconds.

4.4.2 Optical characterization

In this section, optical measurements made on the C-band emitter, sample IV, are discussed. Above-band excitation with the 780 nm CW laser or the 670 nm pulsed laser is used. For the micro-PL measurements, the 150 g/mm grating blazed at 1250 nm and the InGaAs detector are used. Figure 4.7(a) presents the power-dependent spectra of the s-shell transition from a dot in sample IV. It can be seen that six peaks are present even at the lowest excitation power, instead of the typical three emission lines from the dots discussed previously.

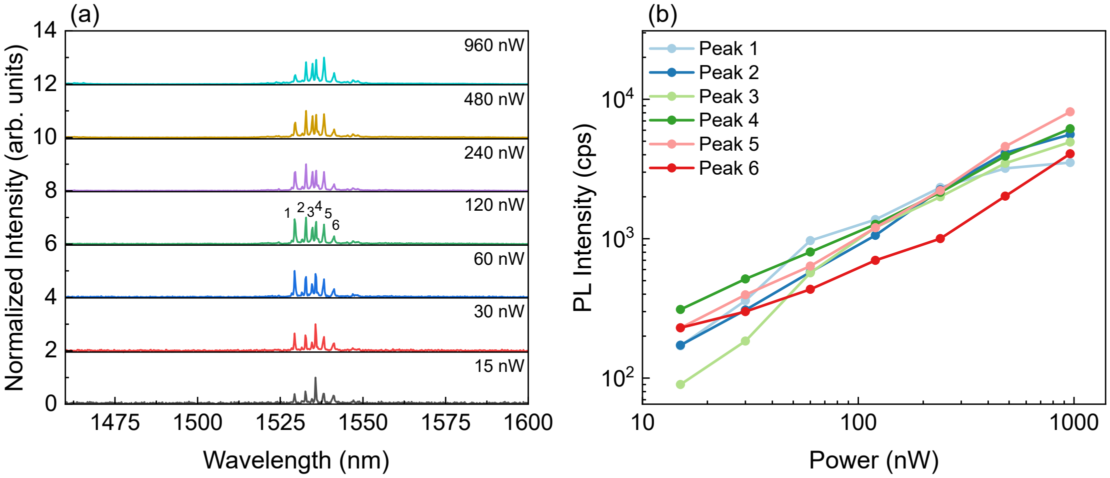

Figure 4.7: (a) Power-dependent PL spectra of the s-shell emission from the dot in sample IV. At higher power, six peaks are observed and labelled in the plot. (b) Integrated intensities (extracted from (a)) for each peak plotted as a function of excitation power.

To identify each peak, power-dependent measurements of the peak intensities were performed, as shown in Figure 4.7(b). The intensity of each peak was determined by integrating the PL count rates (i.e., calculating the area under each peak) at different powers. The previous study demonstrated that peaks can be differentiated based on their power dependence. For example, the biexciton exhibits a stronger dependence on excitation power than the neutral or charged exciton. However, all the peaks shown in the plot exhibit similar behaviour as the pump power is increased, making it difficult to identify them. Additionally, a drastic decrease in count rates for each peak was observed compared to the dots emitting below the telecom C-band, in particular by a factor of 50× compared to the optimized O-band emitter. To gain additional insight into this behaviour, auto-correlation measurements were conducted on these emission lines, where each of them exhibits low coincidence counts at $\tau = 0$, i.e. $g^{(2)}(0) < 0.5$. By using a notch filter with a bandwidth of 12 nm, $g^{(2)}(\tau)$ measurements were also made on the sum of all peaks. In this case, a $g^{(2)}(0)$ value of 0.5 was obtained.

One possible explanation for these emission lines is that they arise from mutually exclusive transitions, each corresponding to a different charge configuration. Although identifying each transition is challenging, the true emission intensity is expected to be the sum of all photons emitted from these transitions. A potential factor contributing to the observed reduction in count rate is the nanowire waveguide geometry. Specifically, the larger base diameter results in $D/\lambda \sim 0.32$, compared to the optimized value of 0.24. As a result, the coupling efficiency into the fundamental mode $\beta_{HE_{11}}$ drops to around $\sim 65\%$ according to Figure 2.13. Additionally, the taper geometry of the nanowire may not be optimal for C-band emission, reducing the fraction of the dot emission that can be coupled to the external system. This reduction further decreases the overall collection efficiency.

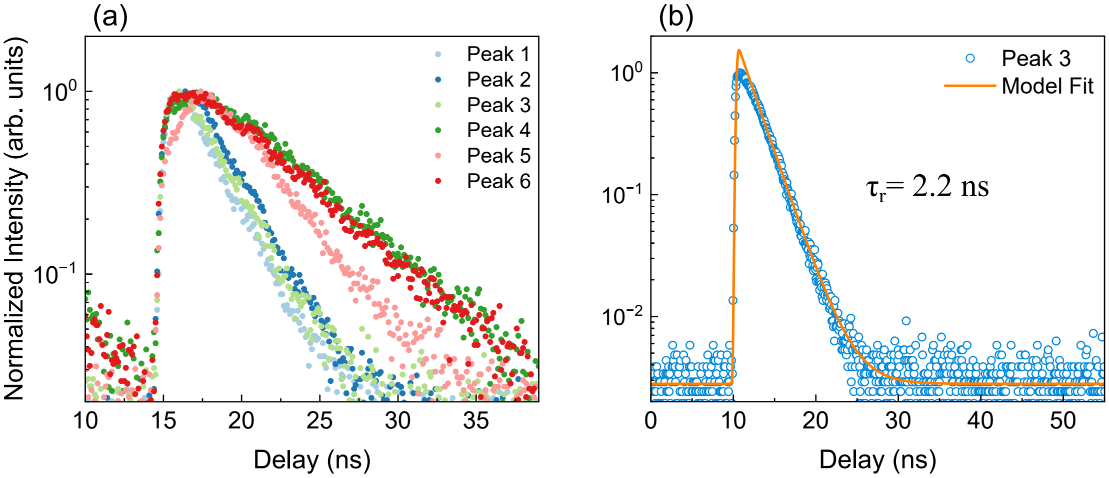

Figure 4.8: TRPL measurements on the dot form sample IV. (a) The experimental results of each peak when the dot is excited using a pulsed laser. (b) The lifetime of a single peak (peak 3) with a model fit based on Eq 3.5.

Next, the TRPL measurements were conducted using the pulsed laser at a repetition rate of 40 MHz, with the excitation power set to P_{sat} for each peak. To isolate each peak, we use the manually tunable filter with a narrow bandwidth of 4-80 GHz. Shorter decay times are observed in peaks 1, 2 and 3, while peaks 4, 5 and 6 have longer decay times. The different decay times support the association of the different peaks with different charge complexes. Additionally, the excitation timing jitter of peak 5 is substantially longer than the others. Since peak 3 (emitting at 1531 nm) exhibits a relatively high emission intensity and short lifetime, the measurement on this peak was also made at a low excitation power ($0.2\,\mathrm{P_{sat}}$) using a repetition rate of 5 MHz to reduce the excitation timing jitter. By fitting the experimental data with Eq. 3.5, a radiative lifetime with value $\tau_r = 2.2\,\mathrm{ns}$ was extracted. This value is slightly larger than that observed in the quantum dot samples emitting below $1\,\mu$m due to the larger nanowire structure and is consistent with the large D/λ ratio.

Lastly, the single-photon purity of peak 3 was measured with the dot excited at $\mathrm{P_{sat}}$ and a repetition rate of 20 MHz. As shown in Figure 4.9, a significant reduction can be observed at zero time delay compared to the side peaks, indicating high-purity single-photon emission. The stochastic model mentioned in section 4.3 is used to fit the experimental data. Here, a raw value of $g^{(2)}(0) = 0.097$ is obtained, which is reduced to $g^{(2)}(0) = 0.062$ after background subtraction.

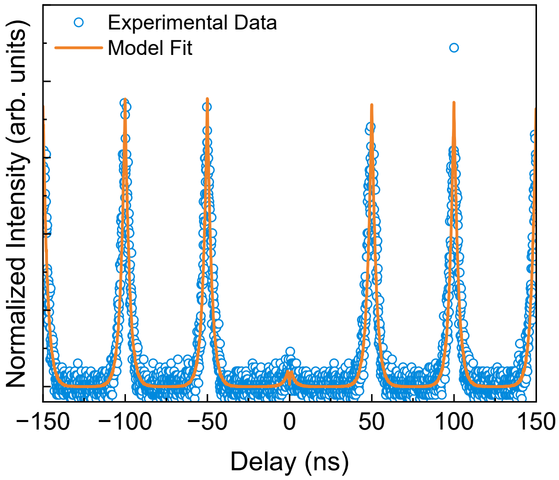

Figure 4.9: Auto-correlation measurements of the peak at 1531 nm excited using a pulsed laser at a repetition rate of 20 MHz (blue circles), fitted with the stochastic model (orange curve).

4.5 Summary

In this chapter, I have presented the optical properties of three different nanowire quantum dot samples at cryogenic temperatures, evaluating their performance as single-photon sources. By changing the size, the aspect ratio, and the As concentration of the dot, the ground state emission wavelength can be tuned from 890 nm to 980 nm. By using non-resonant excitation, PL spectra, radiative decay times and single-photon purities were measured under non-resonant excitation. A significant reduction in excitation timing jitter was observed using p-shell excitation compared to above-band excitation. The auto-correlation measurements indicate that re-excitation is the main factor degrading the single-photon purity.

Single-photon sources emitting in the telecom C-band were also demonstrated. To extend the emission wavelength beyond 1 μm, a DROD structure was employed. This structure offers the opportunity to introduce a higher As concentration in the dots, while maintaining a dot thickness below 10 nm. The C-band emission is achieved by growing a thicker dot compared to the ones emitting in the O-band. A larger base diameter of the nanowire waveguide was targeted to optimize the spontaneous emission rate into the fundamental mode. However, the grown sample had a thicker than optimal base diameter resulting in a potential reduction of the dot-waveguide coupling and emission.

Two important properties that have not been discussed thus far are indistinguishability and coherence properties of the photons generated by the nanowire quantum dot emitters. As mentioned in Chapter 2, the coherence is linked with the emission linewidth. Therefore, we will present the results from both the TPI measurements and the linewidths measurements in the next chapter.

Chapter 5

Coherence Properties at Cryogenic Temperature

In the previous chapter, the optical properties of the quantum dots using non-resonant excitation schemes were demonstrated, with particular emphasis on the influence of quantum confinement on photon emission energies. While non-resonant excitation allows for a comprehensive analysis of optical characteristics, one major drawback is a reduction in the photon indistinguishability since it may introduce additional charge fluctuations around the quantum dot. Excessive excitation timing jitter and re-excitation are additional undesired effects present with above-band excitation. Intuitively, a promising approach to improve indistinguishability is to use strictly resonant excitation. In this case, Sayan and I equally contributed to the resonant excitation project, including the establishment of the optical setup (see Figure 3.6) and all the experiments shown in this chapter.

In this chapter, I will discuss the coherence properties of the quantum dots under different excitation schemes. First I will introduce the resonant excitation technique using the polarization-rejection setup shown in section 3.2.1. I will examine the performance of this setup in three ways: i) the signal-to-noise ratio measured on the spectrometer; ii) the Rabi oscillations of both charged and neutral excitons; and iii) power-dependent autocorrelation measurements to investigate multi-photon emission from the uncorrelated source (i.e. laser leakage). In the latter half of this chapter, I will compare experimental results of linewidth and TPI visibilities using above-band and resonant excitations.

5.1 Resonant Excitation

Resonant fluorescence is performed on a dot from sample C which exhibits similar emission features to the one in Figure 4.1(c). In this dot, the emission wavelengths for X, XX, and X^- are 895.51 nm, 896.99 nm and 898.71 nm, respectively, as shown in Figure 5.1. By using the Mai Tai pulsed laser and the pulse slicer, the excitation wavelength can be precisely tuned to the X or the X^- emission, as required to realize resonant excitation.

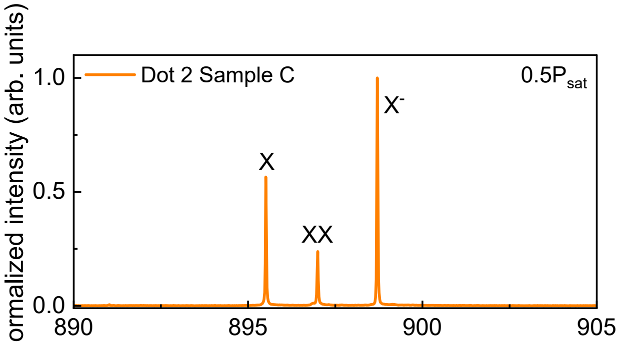

Figure 5.1: The PL spectrum of the dot from sample C under above-band excitation. The excitation power is 0.5 P_{sat}, where P_{sat} is the power saturating the charged exciton emission.

5.1.1 Laser rejection in resonant fluorescence

Owing to the energy overlap between the excitation and the emission, the laser has to be rejected with high efficiency to avoid degrading the single-photon purity of the source. As discussed in section 3.2.1, this is achieved by using two PBSs and one QWP. The rejection process is initialized by first performing the confocal alignment using the Mai Tai laser to optimize collection efficiency. The center wavelength of the laser is tuned close to an excitonic emission and the bandwidth is set by the pulse slicer to approximately 23 ps. After the confocal alignment is achieved, the QWP is rotated to reduce the reflected laser power after fibre coupling. When sufficient excitation power is applied (tens of nW), and the reflected laser polarization is restored to linear and orthogonal to the incident beam, the "clover leaf" pattern can be observed with the laser focused on the nanowire, see Figure 5.2(a). This pattern, however, deviates from the calculated pattern shown in Figure 3.7 due to some unavoidable laser scatter from the nanowire structure. This scatter can degrade the rejection efficiency and result in a remaining portion of the laser after polarization filtering. Further rejection is achieved through spatial filtering using a PM single-mode fibre with a mode field diameter $\sim 5\,\mu$m, which acts as a pinhole, helping to reject residual laser scatter while accepting the Gaussian QD emission profile [82].

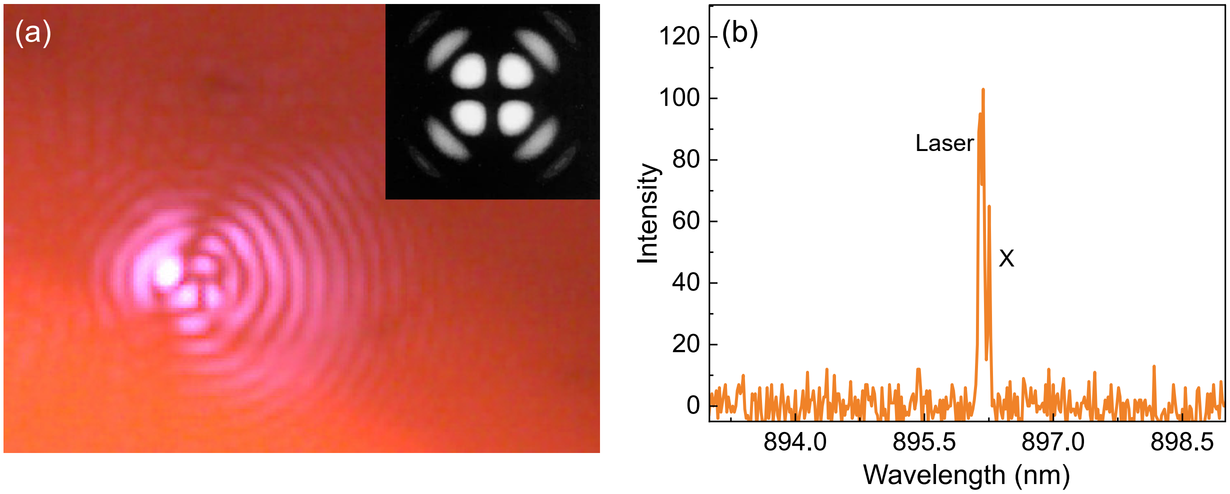

Figure 5.2: (a) The "clover leaf" pattern observed with the laser on the nanowire. The pattern is distorted compared to the simulated result shown in the inset (adapted from [7]) which originates from the undesired laser scattering off the nanowire. (b) PL spectrum showcasing an example of slightly off-resonant laser excitation of the X line when the reflected laser is minimized.

Once the clover leaf pattern is observed, the two beamsplitters for imaging are removed, and the laser power is reduced to a few nanowatts for performing the micro-PL measurements. The laser is tuned to within 0.1 nm of the excitonic emission peak, ensuring excitation occurs via the tail of the laser. At this stage, we iteratively fine-tune the focus (i.e., the height of the objective) and make incremental adjustments to the QWP to maximize the suppression of the laser while maintaining the intensity of the quantum dot emission. Figure 5.2(b) illustrates an example of the laser minimized when detuned from the neutral exciton. Note that a split in the laser peak may occur when the center wavelength of the slicer is detuned by a few nanometers from the laser wavelength, as observed in the figure. For the spectrum in Figure 5.2(b), the laser-to-signal ratio is about 1:1. Both the cloverleaf pattern and the minimized laser intensity confirm an effective laser suppression using the cross-polarization setup. Table 5.1 summarizes one of the best results where the intensity of the laser and the dot PL are recorded for off- and on-resonance conditions. Assuming that the laser intensity remains the same in both cases, a signal-to-laser ratio on the order of $\sim 10^3$ is achieved for RF on the neutral exciton.

	laser intensity (counts/s)	X intensity (counts/s)
off-resonant	~ 10	≤ 150
on-resonant	N/A	~ 12000

Table 5.1: A summary of the reflected laser and the X peak intensities when the excitation laser is 0.1 nm detuned or on-resonant, measured on the spectrometer. Data is recorded at an excitation power corresponding to a π-pulse.

A similar process is implemented on the X^- peak; however, a significantly lower excitation efficiency was observed. This is because the X^- formation requires an additional electron compared to the X. Therefore, a few picowatts of the 780 nm laser is introduced, inaddition to the resonant laser, to provide extra charges and facilitate X^- formation. The above-band laser power is kept below the threshold required to excite the quantum dot and a tunable filter is added before any detection system to filter out the laser. To further confirm the success of resonant fluorescence and effective laser suppression, both single-photon purity and coherent control were established for both X and X^- emission lines.

5.1.2 Coherent Control

When a two-level system interacts with an external oscillating field that is resonant with the system's transition energy, the system will periodically undergo a transition between the ground ($|g\rangle$) and the excited states ($|e\rangle$). Consequently, the probability of finding the system in the excited state depends on time and the strength of the interaction and the system is said to undergo Rabi oscillations [38]. In a semi-classical framework, this probability is typically expressed as

$$P_{|e\rangle}(t) \propto sin^2\left(\frac{\Omega_R t}{2}\right) \tag{5.1}$$

where Ω_R is the Rabi frequency, which is proportional to the field strength (i.e. the square root of the excitation power). In semiconductor quantum dots, Rabi oscillations can be observed in the excitonic emission when the quantum dots are resonantly driven by optical pulses [100, 101, 102]. In other words, power-dependent resonant fluorescence measurements will show an oscillatory behaviour in the emission intensity as a function of pulse area. However, Eq. 5.1 does not account for dephasing effects. Due to the interactions between the quantum dot and its environment, for example, charge noise, decoherence occurs over time. This dampens the visibility of the transitions between the ground and the excited state, leading to a decrease in the amplitude of the oscillation. At long time scales, i.e. much greater than the coherence time, the oscillations will disappear and the probability of finding the system in the excited state converges to 0.5.

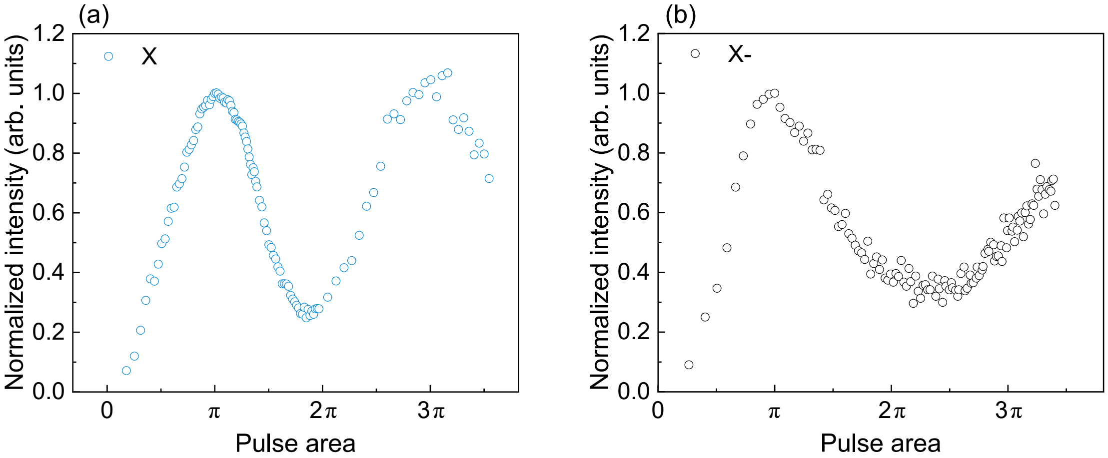

Figure 5.3: Rabi oscillation of (a) the neutral exciton and (b) the charged exciton from the same quantum dot where the intensity was measured using the spectrometer.

To measure the Rabi oscillations of the neutral and the charged excitons in the dot from sample C, a photodetector in combination with the p-i-d program (see Figure 3.6) were used to control the excitation power and record the integrated PL intensity. The RF intensities of X and X^-, plotted as a function of the square root of the excitation power, are shown in Figure 5.3. Rabi oscillations up to a pulse area of $3.5\,\pi$ were measured in the neutral exciton with population inversion occurring at a power of $\sim$ 33.6 nW, known as a π-pulse. An interesting observation is that the intensity at a pulse area of $3\,\pi$ exceeds that of the π-pulse, contrary to expectations, and is a consequence of laser leakage. In the following section, this is further examined through power-dependent $g^{(2)}(\tau)$ measurements to assess the multi-photon emissions.

For the charged exciton, Rabi oscillations were measured up to a pulse area of $3.5\,\pi$, with the π-pulse recorded at $\sim$ 46.7 nW, slightly higher than the X as expected. It is notable that the curve shows increased noise at higher power, as more data points were collected around $2\,\pi$. This noise likely results from power fluctuation caused by polarization drift from the 780 nm laser as the optical setup currently uses only one p-i-d control to monitor the combined excitation power. To improve the power stability in future measurements, an independent p-i-d system could be set up for each laser source.

The demonstration of Rabi oscillations on two excitonic complexes indicates the effectiveness of the resonant excitation technique on the nanowire quantum dot. Next, we perform the second-order correlation measurements to evaluate the single-photon purity of the quantum dot emission under resonant excitation.

5.1.3 Single-photon purity and lifetime using resonant excitation

Auto-correlation measurements using RF were performed on both the neutral and the charged exciton from the same dot. Since a weak 780 nm laser was used to efficiently excite the X^-, an additional tunable filter was used in the detection path. The measured results at $1/3\,\pi$-pulse with model fits are shown in Figure 5.4. From these measurements, coincidences in the zero delay peak of $g^{(2)}(0) \approx 0.032$ for X and $g^{(2)}(0) \approx 0.023$ for X^- were extracted.

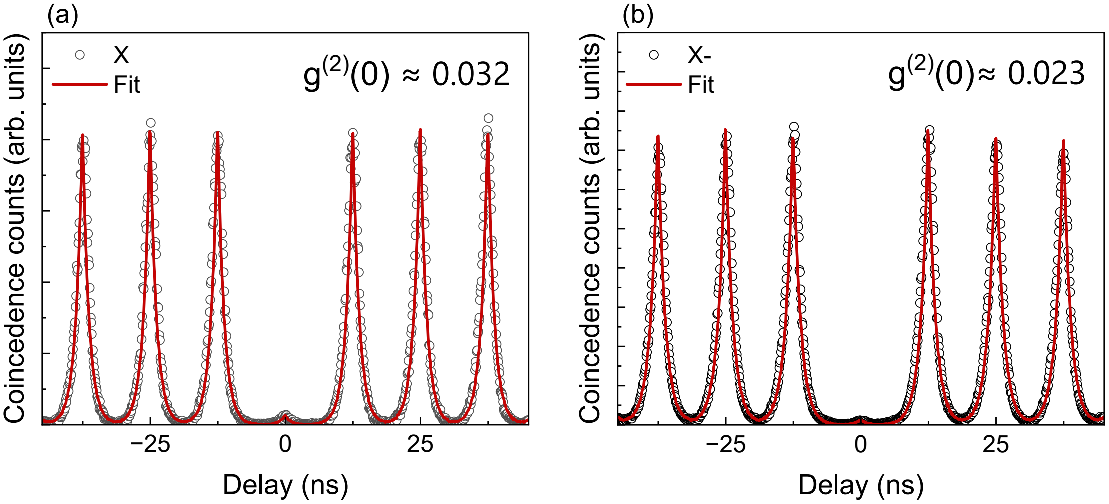

Figure 5.4: Auto-correlation measurement on (a) the neutral exciton and (b) the charged exciton using resonant excitation. The excitation power is at $1/3\,\pi$-pulse for each complex.

Figure 5.5 shows a comparison in the coincidence counts of the neutral exciton around zero time delay using above-band (orange symbols) and resonant (blue symbols) excitation. As discussed in section 4.3, a dip observed at $\tau = 0$ for the AB case indicates a high single-photon purity and the side lobes (re-excitation processes) were hidden in the side plateaus

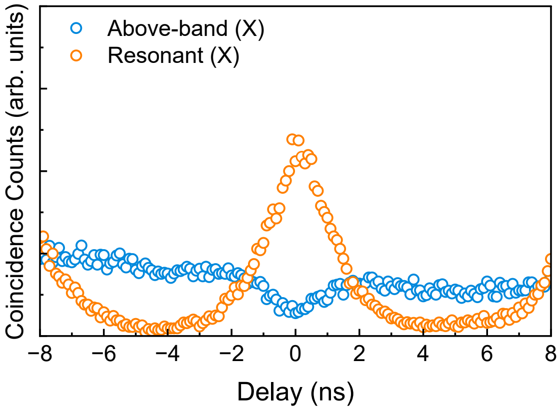

Figure 5.5: Comparison of the coincidence counts around zero delay for auto-correlation measurements of the neutral exciton, X, using above-band and resonant excitation. The dip at $\tau = 0$ in the case of above-band excitation indicates minimal uncorrelated emission whereas the hint of side lobes at $\tau = 2\,\text{ns}$ indicates some re-excitation. For RF, no re-excitation events were observed but the peak at $\tau = 0$ indicates non-negligible uncorrelated emission.

(excitation timing jitter). In contrast, a peak presents at $\tau = 0$ in the RF measurements. There are two possible reasons of observing this peak: (a) the instrumental timing jitter is too long to resolve the dip; (b) multi-photon emission events from an uncorrelated source, i.e. laser leakage.

To further understand this, power-dependent $g^{(2)}(\tau)$ measurements were performed with the RF power ranging from a pulse area of $0.25\,\pi$ to $1.5\,\pi$ in steps of $0.25\,\pi$. The normalized data is plotted in Figure 5.6(a). As can be seen, the peak at zero time delay rises as the excitation power is increased, implying that laser leakage gradually dominates the quantum dot emission and degrades the single-photon purity. The values of $g^{(2)}(0)$ at each power were extracted from the model fit and are plotted versus pulse area in Figure 5.6(b). While a $g^{(2)}(0) \leq 0.07$ on the X photon for pulse areas up to π, coincidence in the zero delay peaks increase nonlinearly with excitation powers. This is consistent with the behaviour observed in the Rabi oscillations in the previous section.

In resonant excitation, multi-photon emission is mainly attributed to imperfect laser filtering i.e. one expects a strongly reduced re-excitation probability. Better laser suppression can be achieved, for example, by using polarizing beamsplitters with higher extinction ratios, or through exact mode-matching of the dark-field microscope with the fundamental mode of the nanowire waveguide.

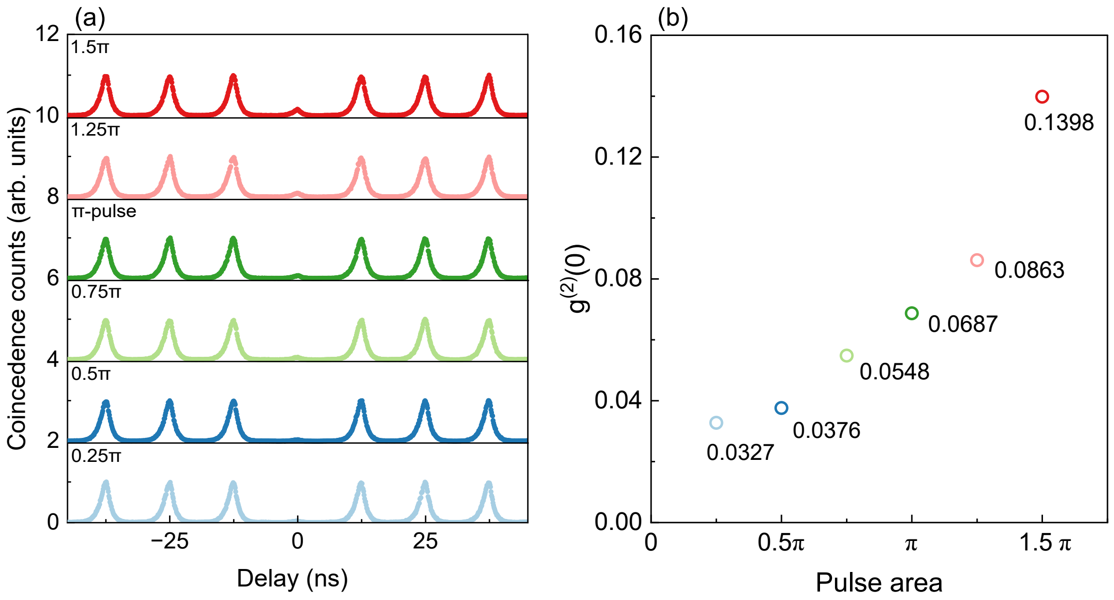

Figure 5.6: (a) Power-dependent normalized auto-correlation measurements on the neutral exciton using resonant excitation. (b) Power-dependent $g^{(2)}(0)$ values extracted from fits using the stochastic model.

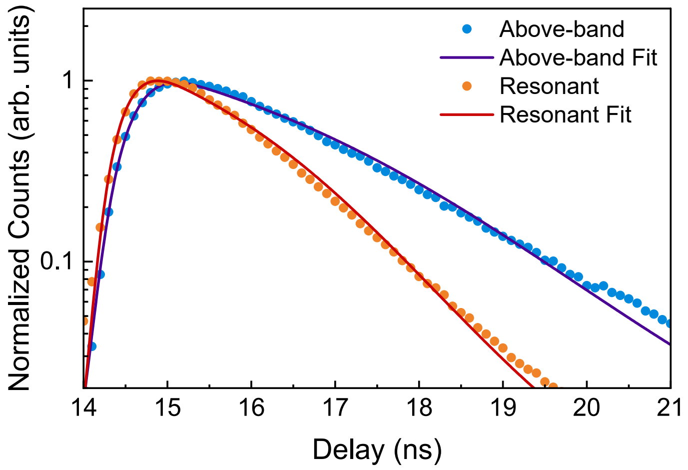

Figure 5.7: Lifetime measurements of the neutral exciton with above-band (blue symbols) and RF (orange symbols). The curves are model fits using Eq 3.5.

Next, the lifetime of the neutral exciton from the same dot under above-band and resonant excitation were compared. TRPL measurements for both excitation schemes are plotted in Figure 5.7 with model fit using Eq 3.5. Both the extracted "rise times" ($\tau_e^{AB} \approx 0.365\,\text{ns}$ for above-band and $\tau_e^{RF} \approx 0.298\,\text{ns}$ for RF) and the decay times ($\tau_r^{AB} \approx 1.833\,\text{ns}$ and $\tau_r^{RF} \approx 1.182\,\text{ns}$) are markedly shorter with resonant excitation. Note that the observed difference in radiative lifetimes is likely due to the limitations of the model used. As a result, the lifetime extracted for the above-band case likely includes a component associated with the excitation timing jitter. Therefore, a better description of the experiment would consider a convolution of a Gaussian function (describing the excitation jitter) and an exponential decay (describing the radiative recombination). Such a model was employed to describe the second-order correlation measurements. Regardless, the faster time scale observed with RF is consistent with an excitation process whereby carriers are populated directly in the lowest energy level in the dot, eliminating excitation jitter.

5.2 Linewidth and Indistinguishability

Spectral purity is another indicator of the quantum performance of the single-photon emitter, as it influences the indistinguishability of the emitted photons. Indistinguishable photons play important roles in quantum computing and quantum cryptography since they can assure reliable operations through perfect interference and prevent eavesdroppers from eavesdropping on secured communications. This section will discuss the indistinguishability of photons generated from excitonic complexes in quantum dots through both linewidth and HOM interference measurements.

In general, crystal defects and impurities exist in semiconductor materials and will result in the creation of carrier trap levels. When the quantum dot is excited above the band gap and if these traps are located close to the quantum dot, their time-varying occupation will produce a varying electric field and shift excitonic emission lines (i.e. spectral wandering) through the Stark effect. Consequently, the emitted photons will have a Voigt lineshape due to this charge noise, i.e. a Gaussian spectral wandering convolved with the Lorentzian homogeneous linewidth [103]. A great deal of work has been done in the past to grow high-quality nanowire quantum dots to reduce charge noise, achieving linewidths as narrow as 2× the lifetime limit [1]. Such narrow linewidths are measured using a voltage-controlled scanning Fabry-Pérot etalon. The transmitted peaks from the etalon are detected on the SNSPD and provide time-integrated high-resolution PL.

First, the linewidths of all three charge complexes from the dot in sample A dot were revisited using the above-band excitation with the 780 nm CW laser. Figure 5.8 shows the measured linewidths of the three charge complexes, X, XX and X^-, at $0.2\,\text{P}_{\text{sat}}$. FSS presents in both XX and X photons with two peaks in each complex corresponding to

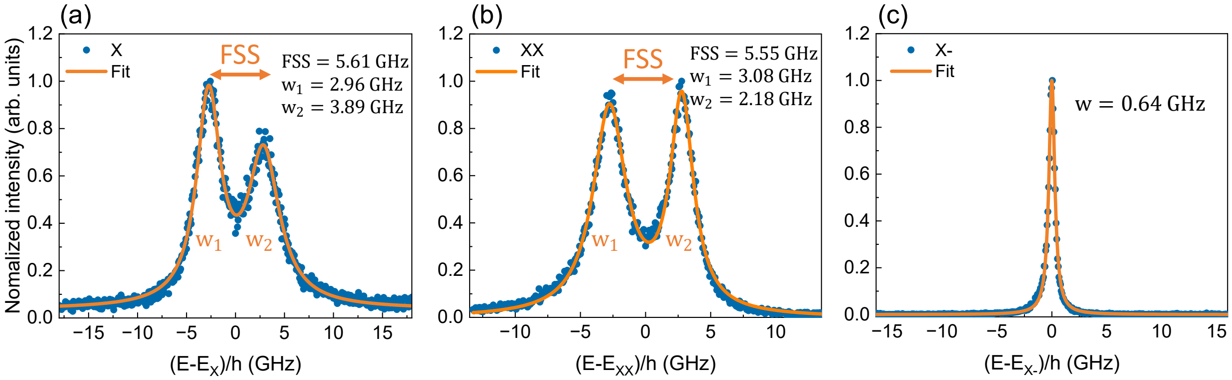

Figure 5.8: Linewidth measurements of the (a) neutral (X), (b) biexciton (XX) and (c) charged exciton (X^-) at an excitation power of $0.2\,\mathrm{P_{sat}}$ (blue symbols). Each experimental data is fitted with a Lorentzian function (orange curves).

the two spin configurations, whilst no FSS is observed in the X^- emission. This result is consistent with the discussion in section 2.3.1. Each peak is well described by a Lorentzian function from which linewidths and FSSs are extracted. The neutral exciton exhibits a FSS of around 5.61 GHz with linewidths of the two peaks $w_1 \approx 2.96\,\mathrm{GHz}$ and $w_2 \approx 3.89\,\mathrm{GHz}$. Similar results are extracted for XX, where $FSS_{XX} \approx 5.61\,\mathrm{GHz}$, $w_1 \approx 3.08\,\mathrm{GHz}$, and $w_2 \approx 2.18\,\mathrm{GHz}$. These FSS values are larger than expected, and likely arise from an asymmetric distribution of As composition along the growth direction due to a long gas switching time in the gas manifold. In contrast, a narrow single linewidth was obtained for X^- emission with a value $\approx 0.64\,\mathrm{GHz}$ with no FSS observed as described in section 2.3.1. This value, after deconvolving with the etalon linewidth, reached $\sim 2\times$ the lifetime-limited value [1].

This dot was also investigated using p-shell excitation, as shown in Figure 5.9(a), which presents power-dependent linewidth measurements. Linewidths are extracted at each excitation power using the same fitting function as in the above-band measurements and are plotted in Figure 5.9(b). The blue curve shows a nonlinear increase in the linewidth of the charged exciton using above-band excitation, whilst no broadening is observed using p-shell excitation (see green curve). Note that linewidths extracted using quasi-resonant excitation are significantly broader compared to above-band excitation. This was initially associated with the cool-down cycle: the sample had been cooled down several times prior to performing the quasi-resonant measurements. It has been observed that each cool-down "freezes in" a different charge environment as evidenced by shifts in emission energies. It was thus thought that each cooling cycle may introduce additional traps, particularly on

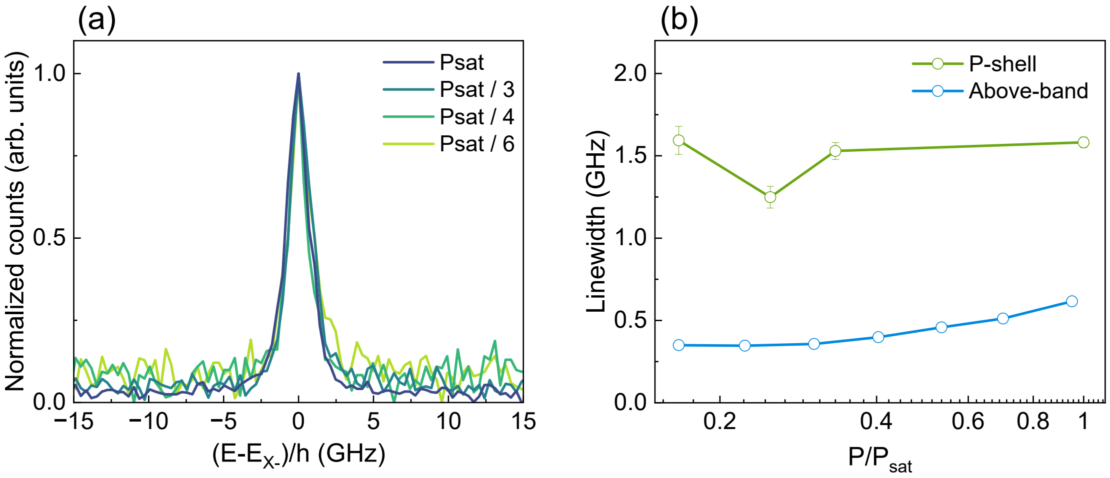

Figure 5.9: (a) HRPL spectra of the X^- photon for different p-shell excitation powers. (b) Extracted Lorentzian linewidths as a function of excitation power using above-band (blue) and p-shell (green) excitation.

the nanowire surface, leading to additional linewidth broadening. However, it appears that some above-band excitation may be important in stabilizing the charge environment. This is discussed below in the context of resonant excitation.

Strictly resonant excitation is one solution for mitigating the charge noise in solid-state systems. It leads to fewer interactions between the dot and the surrounding material. As such, one would expect a reduction in the linewidth using RF compared to above-band and p-shell excitation. The polarization-rejection optical setup is used to conduct the linewidth measurements using both the above-band (670 nm pulsed laser) and the resonant (Mai Tai laser) pumping schemes. In both cases, only one polarization from the emission can be observed as the other one is rejected by the PBSs.

Figure 5.10(a) shows power-dependent linewidths of the neutral exciton from the dot in sample C using the two excitation schemes, where each data point was extracted from a Lorentzian fit. The blue symbol refers to the extracted linewidth measured using the above-band laser at a power of 0.5 $\mathrm{P_{sat}}$. The orange symbols are the linewidths measured using RF at different excitation powers. Interestingly no significant reduction in the X photon linewidths is observed using RF. For the case of X^-, a broader RF linewidth was observed compared to above-band excitation. This is shown in Figure 5.10(b) where the linewidth measurements on the X^- photon using above-band (at 0.1 $\mathrm{P_{sat}}$, upper panel) and resonant excitation (at 0.1 π-pulse, lower panel) are compared. Here, a Lorenzian fit was used for AB measurements, obtaining a linewidth value ∼1.17 GHz. However, to extract a

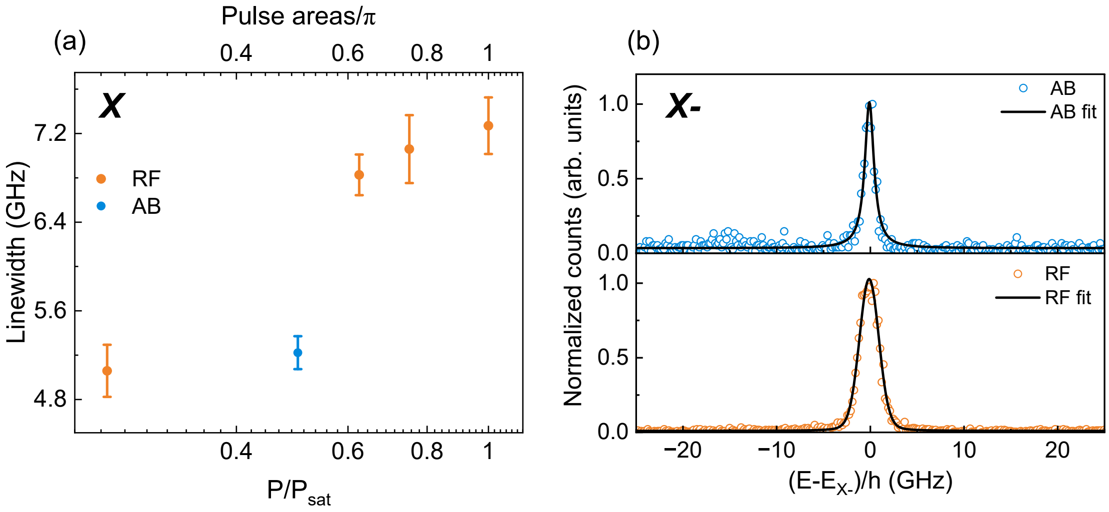

Figure 5.10: (a) Measurements of the X emission line with different pumping conditions. (b) Measured linewidths of the X^- emission peak for above-band (AB) and resonant (RF) excitation.

more accurate value for RF linewidths, a Voigt function was applied, yielding a Lorentzian linewidth $w_L = 0.34\,\text{GHz}$ and a Gaussian linewidth $w_G = 2.28\,\text{GHz}$. This result suggests that rather than mitigating charge noise, RF applied to nanowire quantum dots actually increases charge noise, in contrast to other quantum dot systems [104]. This is particularly true for the charged complex. It is speculated that the requirement of a weak above-band pump for observing charged complexes with RF may not be ideal for stabilizing the charge environment. Further, it has been observed previously in nanowire systems that a strong above-band pumping can minimize charge fluctuation by filling all traps [103].

Next, the indistinguishability between sequentially emitted photons separated by the laser repetition rate of 12.5 ns is determined for both X and X^- above. The measurements are made using a MZI as described in section iv. and the same lasers are used as in the linewidth measurements. For the above-band excitation, a fibre-based polarization controller is added between the tunable filter and the MZI, making sure the input polarization is linear. Figure 5.11 and 5.12 shows the measured coincidences $g^{(2)}_{\perp}(\tau)$ (in black shaded area) and $g^{(2)}_{\parallel}(\tau)$ (in red shaded area) of X and X^-, respectively. In all cases, coincidence counts of 0.75 are recorded at $\tau = \pm T$ relative to $\tau = \pm 2T$. This is due to the absence of simultaneous photons incident on the PBS [89]. The peaks at $\pm T$ are uneven because of the unbalanced counts in the two arms of the interferometer. For two perfectly indistinguishable photons, one should observe the centre peaks $g^{(2)}_{\parallel}(0) = 0$ and

$g^{(2)}_{\perp}(0) = 0.5$. Here, significant coincidences are observed for $g^{(2)}_{\parallel}(0)$ in all cases, indicating low TPI visibility. By integrating the area of the co-polarized and cross-polarized data across the zero delay window (-6.25 ns to +6.25 ns), we obtain the visibilities for the neutral exciton $V_X^{AB}(0) \approx 0.8\%$ and $V_X^{RF}(0) \approx 21.7\%$. For the X^-, the extracted visibilities are $V_{X^-}^{AB}(0) \approx 8.37\%$ and $V_{X^-}^{RF}(0) \approx 14.4\%$, respectively.

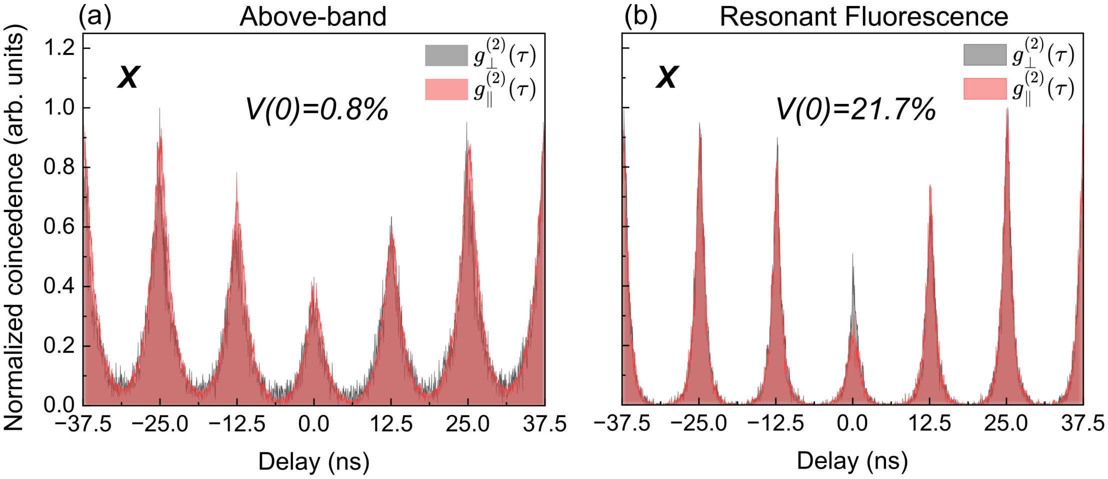

Figure 5.11: HOM measurements of the X peak using (a) above-band excitation at $\mathrm{P_{sat}}/5$, and (b) resonant excitation at $1/5\,\pi$-pulse.

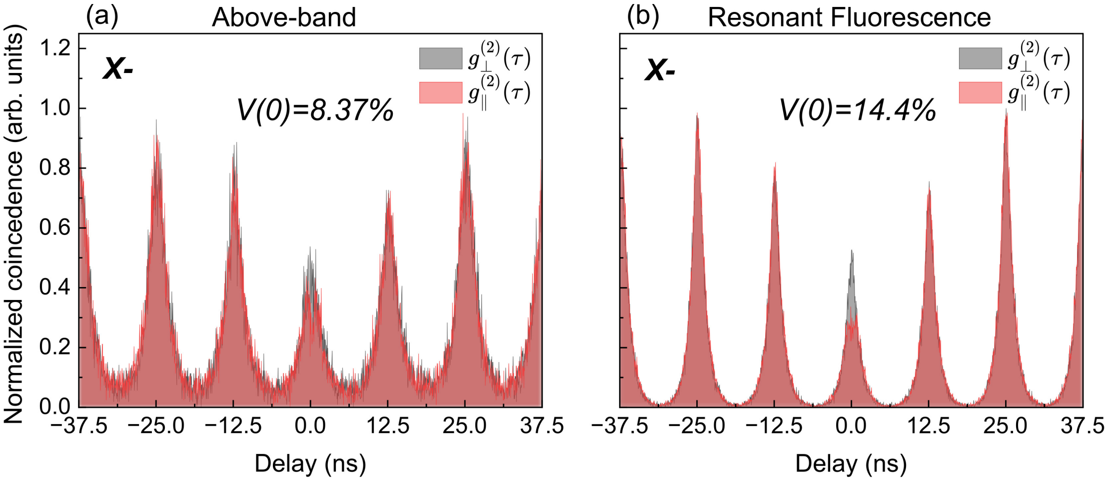

Figure 5.12: HOM measurements of the X^- peak using (a) above-band excitation at $\mathrm{P_{sat}}$ and (b) resonant excitation at a pulse area of π.

For both charge complexes measured above, TPI visibilities are improved using resonant excitation compared to above-band excitation. The improvement for the X peak is considerably more significant than for X^-, whilst the above-band visibility for the X^- photon is much greater than the X photon. Recall that for both the X and X^- photons, RF eliminates excitation jitter (see section 5.1.3), thus the observation of higher TPI visibilities in both cases. However, the linewidth measurements showed more excess broadening for the X photon compared to the X^- photon under AB excitation, suggesting that charge noise has a more severe impact on the X photon, consistent with the reduced above-band TPI visibility for the X^- photon. Additionally, HRPL measurements showed no change in the X linewidths under low-power resonant excitation, indicating that the improvement in TPI visibilities, from 0.8% to 21.7%, is primarily due to the elimination of excitation jitter. In contrast, the X^- photon linewidth was broadened using RF due to increased charge fluctuation, which tempered the improvement in the TPI visibility. Finally, the visibilities obtained in this work are consistent with those reported for other quantum dot systems with a $\sim 1\,\mathrm{ns}$ radiative lifetime, resonantly pumped using a pulsed laser with a $12.5\,\mathrm{ns}$ pulse separation [105].

5.3 Summary

To conclude, the influence of different excitation schemes on the coherence properties of a nanowire quantum dot was investigated in this chapter. Importantly, efficient resonant excitation was realized using the polarization-rejection method with two PBSs and one QWP, achieving high emission-to-laser ratios for both X and X^- photons. This was confirmed through HBT measurements which showed high single-photon purity, low excitation timing jitter and negligible re-excitation using resonant excitation. A reduction in single-photon purity with increasing pump power was observed, indicating that better rejection would be beneficial. Rabi oscillations over pulse areas of $3.5\,\pi$ for both the photon X and the X^- photon were observed, showcasing the success of coherent control in the nanowire quantum dot system.

At this preliminary stage, no reduction in the exciton linewidths was observed using the resonant excitation compared to the above-band excitation. In fact, the X^- photon linewidth was broadened using RF which was associated with increased charge noise from the added weak AB laser. These differing linewidth behaviours between the two excitons are consistent with the TPI measurements where the improvement in TPI visibility using RF is less significant for the charged exciton compared to the neutral exciton. While the results align with those from other quantum dot systems, further improvements in TPI visibilities and strategies to mitigate charge noise are still needed. These will be discussed in the following chapter.

Chapter 6

Conclusion and Future Work

In the previous chapters, the optical properties of nanowire quantum dots under different growth conditions were described. This chapter will first summarize the experimental results and provide a conclusion. The second half will outline potential future research directions, focusing on both the electronic and optical properties of nanowire quantum dots.

6.1 Conclusion

This work began by demonstrating the quantum size effect on the optical properties of nanowire quantum dots. It was shown that the confined energy levels and energy bandgap can be varied by controlling the dot's size, aspect ratio, and arsine concentration during growth.

Particularly, optical characterizations, including the micro-PL spectra, radiative lifetimes and single-photon purities, were conducted on three different quantum dot samples. The PL measurements under the above-band excitation revealed that the emission wavelengths of these dots could be tuned from 890 nm to 980 nm, with variable s-p splitting. Generally, smaller dots exhibit larger bandgaps and blue-shifted emission wavelengths, while dots with smaller diameters have reduced in-plane confinement and greater separation between s- and p-orbitals. P-shell excitation was performed on the dot from sample A, showing charged exciton emission under high excitation power. Next, power-dependent TRPL measurements on this dot using the two excitation schemes showed similar rise times ($\approx 0.19\,\mathrm{ns}$) and radiative decay times ($\approx 1\,\mathrm{ns}$) at 0.5 $\mathrm{P_{sat}}$. However, above-band excitation introduced more significant delays in the excitation process at higher power and exhibited varying decay times compared to the p-shell scheme. This inconsistency is likely due to limitations in the fitting model, as the rise and decay times are expected to be correlated. Auto-correlation measurements on a dot from sample C, conducted using an above-band pulsed laser at 40 MHz, yielded a single-photon purity of 90%.

To extend the emission wavelengths to the telecom C-band, a DROD structure was employed. This approach involved growing the dots with higher arsine concentrations and greater thickness than those used for O-band emitters. PL measurements revealed red-shifted emission wavelengths around 1530 nm, although multiple peaks and lower count rates compared to the O-band devices. Characterization of the 1531 nm peak demonstrated a raw single-photon purity of 90.3% (93.8% after background subtraction) and a lifetime of approximately 2.2 ns. Reduced brightness was attributed to the nanowire waveguide geometry, specifically the base diameter and taper length.

Lastly, the coherence properties of dots emitting below 1 μm were explored under different excitation schemes. RF on one dot from sample C was conducted using a polarization-rejection optical setup. The setup, incorporating two polarizing beam splitters, a quarter-wave plate, and spatial filtering (via fibre coupling), achieved effective laser suppression on the neutral exciton. This was confirmed through high single-to-laser ratios and the observation of Rabi oscillations on the spectrometer. RF measurements yielded $g^{(2)}(0) \approx 0.032$ for X peak and and $g^{(2)}(0) \approx 0.023$ for X^- peak. RF also resulted in reduced excitation timing jitter, evident in narrower side peaks in the $g^{(2)}(\tau)$ measurements and sharper rises in the TRPL. Linewidth measurements showed that the power broadening is significantly greater under above-band excitation compared to the p-shell. However, linewidths were not reduced for either X or X^- emissions under resonant excitation, at a power comparable with the above-band excitation. Lastly, the TPI visibilities were improved under RF by eliminating the excitation timing jitter. The values were increased from 0.8% to 21.7% for the X peak and from 8.37% to 14.4% for the X^- peak.

6.2 Future work

As evident in Chapters 4 and 5, further improvements are necessary to better understand nanowire quantum dots and enhance their optical performance. One key improvement is increasing the brightness and the emission rate of telecom C-band emitters, which can be accomplished by optimizing the nanowire waveguide geometry. Specifically, fine-tuning the growth temperature and time of the waveguide cladding can enable the base diameter and the taper length to be close to the optimal value. While the base diameter is expected to be around 390 nm to maintain $D/\lambda \sim 0.24$, a waveguide with a greater height and a smaller tapering angle may improve the overlap between the optical mode of the nanowire and the quantum dot emission (i.e. $\beta_{He_{11}}$), as well as more efficient collection by external optical systems.

For future applications, such as quantum key distribution, it is essential to study the coherence properties of the nanowire quantum dots. This thesis has demonstrated both linewidths and TPI measurements on the devices emitting below 1 μm under three excitation schemes. However, the results suggest that using RF alone does not significantly reduce charge noise compared to the above-band and p-shell excitations. One explanation is that the timescale associated with capturing and releasing the charge carriers from nearby traps is comparable to the radiative recombination time of an exciton confined within the dot.

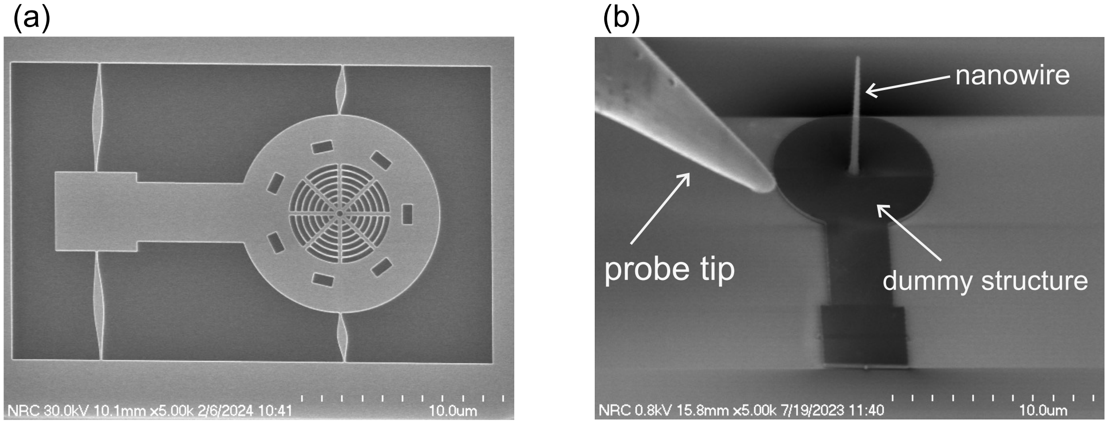

Figure 6.1: (a) SEM image of a CBR structure fabricated in silicon on insulator (SOI) material, viewed from the top. (b) SEM imagine viewed at 45° shows that a pre-fabricated dummy silicon structure placed over a nanowire using the pick-and-place technique.

Minimizing the impact of the charge environment on dot emissions can be achieved either by reducing the radiative lifetime of the excitons or by mitigating charge noise through the application of an external electric field. As mentioned in section 2.3.2, photonic cavities can enhance the spontaneous emission rate through the Purcell effect and shorten the radiative lifetime. In the nanowire quantum dot system, one possible structure is a circular Bragg resonator (CBR), as shown in Figure 6.1(a). A pick-and-place technique [96] will be applied to lift a tethered CBR from its substrate and position it over a nanowire through the centre hole. Figure 6.1(b) shows an exemplary SEM image of transferring a dummy structure onto a single nanowire. This demonstrates the feasibility of applying the cavity to the nanowire quantum dot device. Here, the dot is expected to be in the plane of the CBR. The position of the quantum dot in relation to the CBR will be tuned by using both nanopositioners and nanoscanners to match the dot emission energy to the cavity mode, optimizing the Purcell enhancement factor.

Another promising method for stabilizing the charge environments is applying an external electric field by using gates located around the optical quantum dot system. Previous work has demonstrated the effect of electric field on the energy tuning and FSS reduction of the quantum dot emission [106]. Additionally, when an external electric field is applied, the band structure of the dot and its surrounding material will be both modified such that the depth of a nearby trap potential is reduced. In this case, carriers can be swept from traps, hence suppressing the trapping and untrapping events. However, unlike the planar quantum dot systems, monolithic fabrication of gate structures on the sides of the free-standing nanowire is technically challenging due to the high aspect ratio of the nanowire geometry. Therefore, the pick-and-place method is again required to bridge the nanowire device and the external structures. Specifically, this can be realized in two ways, either by picking up a nanowire and placing it onto a gated structure, or by picking up a pre-patterned gate structure from the SOI substrate and placing it over a nanowire.

Lastly, the techniques discussed above for enhancing the coherence properties will be applied to the telecom dots. Optical properties regarding emission linewidths, TPI visibilities and photon coherence will be investigated on those quantum dots to facilitate long-distance secure communication technologies.

References

[1] P. Laferriére, A. Yin, E. Yeung, L. Kusmic, M. Korkusinski, P. Rasekh, D. B. Northeast, S. Haffouz, J. Lapointe, P. J. Poole, *et al.*, "Approaching transform-limited photons from nanowire quantum dots using excitation above the band gap," *Physical Review B*, vol. 107, no. 15, p. 155422, 2023.

[2] Y. Tokura, L. Kouwenhoven, D. Austing, and S. Tarucha, "Many-body effect in an artificial atom," *Physica B: Condensed Matter*, vol. 246, pp. 83–87, 1998.

[3] R. Hanson, J. M. Elzerman, L. H. W. Van Beveren, L. Vandersypen, L.-X. Zhang, P. Matagne, J. Leburton, and L. Kouwenhoven, "Experiments and simulations on a few-electron quantum dot circuit with integrated charge read-out," in *AIP Conference Proceedings*, vol. 772, pp. 44–49, American Institute of Physics, 2005.

[4] A. Rastelli, S. M. Ulrich, E.-M. Pavelescu, T. Leinonen, M. Pessa, P. Michler, and O. G. Schmidt, "Self-assembled quantum dots for single-dot optical investigations," *Superlattices and Microstructures*, vol. 36, no. 1-3, pp. 181–191, 2004.

[5] S. Kolatschek, C. Nawrath, S. Bauer, J. Huang, J. Fischer, R. Sittig, M. Jetter, S. L. Portalupi, and P. Michler, "Bright purcell enhanced single-photon source in the telecom o-band based on a quantum dot in a circular bragg grating," *Nano letters*, vol. 21, no. 18, pp. 7740–7745, 2021.

[6] P. Laferriére, S. Haffouz, D. B. Northeast, P. J. Poole, R. L. Williams, and D. Dalacu, "Position-controlled telecom single photon emitters operating at elevated temperatures," *Nano Letters*, vol. 23, no. 3, pp. 962–968, 2023.

[7] L. Novotny, R. D. Grober, and K. Karrai, "Reflected image of a strongly focused spot," *Optics letters*, vol. 26, no. 11, pp. 789–791, 2001.

[8] M. Planck, *Über das gesetz der energieverteilung im normalspektrum*. Springer, 1978.

[9] A. Einstein, “Über einen die erzeugung und verwandlung des lichtes betreffenden heuristischen gesichtspunkt,” *Annalen der Physik*, vol. 322, no. 6, pp. 132–148, 1905.

[10] C. J. Chunnilall, I. P. Degiovanni, S. Kück, I. Müller, and A. G. Sinclair, “Metrology of single-photon sources and detectors: a review,” *Optical Engineering*, vol. 53, no. 8, pp. 081910–081910, 2014.

[11] N. Maring, A. Fyrillas, M. Pont, E. Ivanov, P. Stepanov, N. Margaria, W. Hease, A. Pishchagin, A. Lemaître, I. Sagnes, *et al.*, “A versatile single-photon-based quantum computing platform,” *Nature Photonics*, vol. 18, no. 6, pp. 603–609, 2024.

[12] D. Bhattacharyya and J. Guha, *Quantum Optics and Quantum Computation.* 2053-2563, IOP Publishing, 2022.

[13] Y. Arakawa and M. J. Holmes, “Progress in quantum-dot single photon sources for quantum information technologies: A broad spectrum overview,” *Applied Physics Reviews*, vol. 7, no. 2, 2020.

[14] C. Portmann and R. Renner, “Security in quantum cryptography,” *Rev. Mod. Phys.*, vol. 94, p. 025008, Jun 2022.

[15] C. Schimpf, M. Reindl, D. Huber, B. Lehner, S. F. Covre Da Silva, S. Manna, M. Vyvlecka, P. Walther, and A. Rastelli, “Quantum cryptography with highly entangled photons from semiconductor quantum dots,” *Science advances*, vol. 7, no. 16, p. eabe8905, 2021.

[16] T. Kupko, M. von Helversen, L. Rickert, J.-H. Schulze, A. Strittmatter, M. Gschrey, S. Rodt, S. Reitzenstein, and T. Heindel, “Tools for the performance optimization of single-photon quantum key distribution,” *npj Quantum Information*, vol. 6, no. 1, p. 29, 2020.

[17] S. J. Freedman and J. F. Clauser, “Experimental test of local hidden-variable theories,” *Phys. Rev. Lett.*, vol. 28, pp. 938–941, Apr 1972.

[18] J. F. Clauser, “Experimental distinction between the quantum and classical field-theoretic predictions for the photoelectric effect,” *Phys. Rev. D*, vol. 9, pp. 853–860, Feb 1974.

[19] X. Guo, C.-l. Zou, C. Schuck, H. Jung, R. Cheng, and H. X. Tang, “Parametric down-conversion photon-pair source on a nanophotonic chip,” *Light: Science & Applications*, vol. 6, no. 5, pp. e16249–e16249, 2017.

[20] J.-P. Li, X. Gu, J. Qin, D. Wu, X. You, H. Wang, C. Schneider, S. Höfling, Y.-H. Huo, C.-Y. Lu, N.-L. Liu, L. Li, and J.-W. Pan, "Heralded nondestructive quantum entangling gate with single-photon sources," *Phys. Rev. Lett.*, vol. 126, p. 140501, Apr 2021.

[21] N. Montaut, L. Sansoni, E. Meyer-Scott, R. Ricken, V. Quiring, H. Herrmann, and C. Silberhorn, "High-efficiency plug-and-play source of heralded single photons," *Phys. Rev. Appl.*, vol. 8, p. 024021, Aug 2017.

[22] X. Lu, Q. Li, D. A. Westly, G. Moille, A. Singh, V. Anant, and K. Srinivasan, "Chip-integrated visible–telecom entangled photon pair source for quantum communication," *Nature physics*, vol. 15, no. 4, pp. 373–381, 2019.

[23] F. A. Domínguez-Serna, F. Rojas, and K. Garay-Palmett, "Quantum teleportation with hybrid entangled resources prepared from heralded quantum states," *Journal of the Optical Society of America. B, Optical physics*, vol. 37, no. 3, pp. 695–701, 2020.

[24] A. Christ and C. Silberhorn, "Limits on the deterministic creation of pure single-photon states using parametric down-conversion," *Phys. Rev. A*, vol. 85, p. 023829, Feb 2012.

[25] I. Aharonovich, D. Englund, and M. Toth, "Solid-state single-photon emitters," *Nature photonics*, vol. 10, no. 10, pp. 631–641, 2016.

[26] H. J. Kimble, M. Dagenais, and L. Mandel, "Photon antibunching in resonance fluorescence," *Phys. Rev. Lett.*, vol. 39, pp. 691–695, Sep 1977.

[27] A. M. Dibos, M. Raha, C. M. Phenicie, and J. D. Thompson, "Atomic source of single photons in the telecom band," *Phys. Rev. Lett.*, vol. 120, p. 243601, Jun 2018.

[28] X. Cao, M. Zopf, and F. Ding, "Telecom wavelength single photon sources," *Journal of Semiconductors*, vol. 40, p. 071901, jul 2019.

[29] A. Beveratos, R. Brouri, T. Gacoin, A. Villing, J.-P. Poizat, and P. Grangier, "Single photon quantum cryptography," *Phys. Rev. Lett.*, vol. 89, p. 187901, Oct 2002.

[30] B. Lienhard, T. Schröder, S. Mouradian, F. Dolde, T. T. Tran, I. Aharonovich, and D. Englund, "Bright and photostable single-photon emitter in silicon carbide," *Optica*, vol. 3, no. 7, pp. 768–774, 2016.

[31] L. Hanschke, K. A. Fischer, S. Appel, D. Lukin, J. Wierzbowski, S. Sun, R. Trivedi, J. Vučković, J. J. Finley, and K. Müller, “Quantum dot single-photon sources with ultra-low multi-photon probability,” *npj Quantum Information*, vol. 4, no. 1, p. 43, 2018.

[32] D. Huber, M. Reindl, S. F. Covre da Silva, C. Schimpf, J. Martín-Sánchez, H. Huang, G. Piredda, J. Edlinger, A. Rastelli, and R. Trotta, “Strain-tunable gaas quantum dot: A nearly dephasing-free source of entangled photon pairs on demand,” *Phys. Rev. Lett.*, vol. 121, p. 033902, Jul 2018.

[33] N. Tomm, A. Javadi, N. O. Antoniadis, D. Najer, M. C. Löbl, A. R. Korsch, R. Schott, S. R. Valentin, A. D. Wieck, A. Ludwig, *et al.*, “A bright and fast source of coherent single photons,” *Nature Nanotechnology*, vol. 16, no. 4, pp. 399–403, 2021.

[34] E. R. Pike, “Lasers, photon statistics, photon-correlation spectroscopy and subsequent applications,” *Journal of the European Optical Society - Rapid publications*, vol. 5, no. 0, 2010.

[35] S. Scheel, “Single-photon sources–an introduction,” *Journal of Modern Optics*, vol. 56, no. 2-3, pp. 141–160, 2009.

[36] T. Yatsui, *Progress in Nanophotonics 7*. Quantum Optics, Springer Cham, 2022.

[37] R. E. Slusher, L. W. Hollberg, B. Yurke, J. C. Mertz, and J. F. Valley, “Observation of squeezed states generated by four-wave mixing in an optical cavity,” *Phys. Rev. Lett.*, vol. 55, pp. 2409–2412, Nov 1985.

[38] M. Scully and M. Zubairy, *Quantum Optics*. Quantum Optics, Cambridge University Press, 1997.

[39] R. Hanbury Brown and R. Q. Twiss, “A Test of a new type of stellar interferometer on Sirius,” *Nature*, vol. 178, pp. 1046–1048, 1956.

[40] E. Knill, R. Laflamme, and G. J. Milburn, “A scheme for efficient quantum computation with linear optics,” *Nature Publishing Group*, vol. 409, p. 46–52, 2001.

[41] H. J. Kimble, “The quantum internet,” *Nature*, vol. 453, p. 1023–1030, 2008.

[42] N. Lal, S. Mishra, and R. P. Singh, “Indistinguishable photons,” *AVS Quantum Science*, vol. 4, p. 021701, 04 2022.

[43] C. K. Hong, Z. Y. Ou, and L. Mandel, “Measurement of subpicosecond time intervals between two photons by interference,” *Phys. Rev. Lett.*, vol. 59, pp. 2044–2046, Nov 1987.

[44] A. Kiraz, M. Atatüre, and A. Imamoğlu, “Quantum-dot single-photon sources: Prospects for applications in linear optics quantum-information processing,” *Phys. Rev. A*, vol. 69, p. 032305, Mar 2004.

[45] E. B. Flagg, A. Muller, S. V. Polyakov, A. Ling, A. Migdall, and G. S. Solomon, “Interference of single photons from two separate semiconductor quantum dots,” *Phys. Rev. Lett.*, vol. 104, p. 137401, Apr 2010.

[46] C. Santori, D. A. Fattal, J. Vuckovic, G. S. Solomon, Y. Yamamoto, and Y. Yamamoto, “Indistinguishable photons from a single-photon device,” *Nature Publishing Group*, 2002.

[47] F. Torcal-Milla, J. Lobera, A. Lopez, V. Palero, N. Andres, and M. Arroyo, “Mach-zehnder-based measurement of light emitting diodes temporal coherence,” *Optik*, vol. 267, p. 169722, 2022.

[48] A. Ekimov, A. Onushchenko, and V. Tsekhomskii, “Exciton light absorption by cucl microcrystals in glass matrix,” *Sov. Glass Phys. Chem*, vol. 6, pp. 511–512, 1980.

[49] V. Golubkov, A. Ekimov, A. Onushchenko, and V. Tsekhomskii, “The growth kinetics of cucl microcrystals in a vitreous matrix,” *Fiz. Khim. Stekla*, vol. 7, no. 4, pp. 397–401, 1981.

[50] A. Ekimov and A. Onushchenko, “Quantum size effect in semiconductor three-dimensional microcrystals,” *Pis’ ma Zh Eksp Teor Fiz*, vol. 34, pp. 363–366, 1981.

[51] R. Rossetti, S. Nakahara, and L. E. Brus, “Quantum size effects in the redox potentials, resonance Raman spectra, and electronic spectra of CdS crystallites in aqueous solution,” *The Journal of Chemical Physics*, vol. 79, pp. 1086–1088, 07 1983.

[52] “Electron-electron and electron-hole interactions in small semiconductor crystallites: the size dependence of the lowest excited electronic state,” *The Journal of chemical physics*, vol. 80, no. 9, pp. 4403–4409, 1984.

[53] M. Fox, *Optical properties of solids*, vol. 3. Oxford university press, 2010.

[54] M. Korkusinski, “Correlations in semiconductor quantum dots.,” 2004.

[55] I. Lifshitz and A. Kosevich, “On the oscillations of the thermodynamic parameters of a degenerate fermi gas at low temperatures,” *Bulletin of the Academy of Sciences of the USSR. Physics*, vol. 19, pp. 353–357, 1955.

[56] Y. Peter and M. Cardona, *Fundamentals of semiconductors: physics and materials properties*. Springer Science & Business Media, 2010.

[57] P. Hawrylak and M. Korkusiński, “Electronic properties of self-assembled quantum dots,” in *Single quantum dots: Fundamentals, applications, and new concepts*, pp. 25–92, Springer, 2003.

[58] E. Gadret, G. Dias, L. Dacal, M. de Lima Jr, C. Ruffo, F. Iikawa, M. Brasil, T. Chiaramonte, M. Cotta, L. Tizei, *et al.*, “Valence-band splitting energies in wurtzite inp nanowires: Photoluminescence spectroscopy and ab initio calculations,” *Physical Review B—Condensed Matter and Materials Physics*, vol. 82, no. 12, p. 125327, 2010.

[59] R. Singh, “Tuning fine structure splitting and exciton emission energy in semiconductor quantum dots,” *Journal of Luminescence*, vol. 202, pp. 118–131, 2018.

[60] P. Michler, *Quantum dots for quantum information technologies*, vol. 237. Springer, 2017.

[61] H. Robinson and B. Goldberg, “Light-induced spectral diffusion in single self-assembled quantum dots,” *Physical Review B*, vol. 61, no. 8, p. R5086, 2000.

[62] A. Muller, E. B. Flagg, P. Bianucci, X. Y. Wang, D. G. Deppe, W. Ma, J. Zhang, G. J. Salamo, M. Xiao, and C. K. Shih, “Resonance fluorescence from a coherently driven semiconductor quantum dot in a cavity,” *Phys. Rev. Lett.*, vol. 99, no. 18, p. 187402, 2007.

[63] B. Gerardot, R. Barbour, D. Brunner, P. Dalgarno, A. Badolato, N. Stoltz, P. Petroff, J. Houel, and R. Warburton, “Laser spectroscopy of individual quantum dots charged with a single hole,” *Applied Physics Letters*, vol. 99, no. 24, 2011.

[64] H. Wang, Z.-C. Duan, Y.-H. Li, S. Chen, J.-P. Li, Y.-M. He, M.-C. Chen, Y. He, X. Ding, C.-Z. Peng, *et al.*, “Near-transform-limited single photons from an efficient solid-state quantum emitter,” *Physical Review Letters*, vol. 116, no. 21, p. 213601, 2016.

[65] T. Takagahara, “Theory of exciton dephasing in semiconductor quantum dots,” *Physical Review B*, vol. 60, no. 4, p. 2638, 1999.

[66] A. Reigue, J. Iles-Smith, F. Lux, L. Monniello, M. Bernard, F. Margaillan, A. Lemaitre, A. Martinez, D. P. McCutcheon, J. Mørk, *et al.*, “Probing electron-phonon interaction through two-photon interference in resonantly driven semiconductor quantum dots,” *Physical review letters*, vol. 118, no. 23, p. 233602, 2017.

[67] P. Yu and Z. M. Wang, *Quantum dot optoelectronic devices.* Springer, 2020.

[68] J. Phoenix, “Investigation of photon interactions with semiconductor quantum dot devices for quantum communication applications,” Master’s thesis, University of Waterloo, 2020.

[69] M. Ciorga, A. Sachrajda, P. Hawrylak, C. Gould, P. Zawadzki, S. Jullian, Y. Feng, and Z. Wasilewski, “Addition spectrum of a lateral dot from coulomb and spin-blockade spectroscopy,” *Physical Review B*, vol. 61, no. 24, p. R16315, 2000.

[70] D. Leonard, K. Pond, and P. M. Petroff, “Critical layer thickness for self-assembled inas islands on gaas,” *Phys. Rev. B*, vol. 50, pp. 11687–11692, Oct 1994.

[71] D. Dalacu, A. Kam, D. G. Austing, X. Wu, J. Lapointe, G. C. Aers, and P. J. Poole, “Selective-area vapour–liquid–solid growth of inp nanowires,” *Nanotechnology*, vol. 20, no. 39, p. 395602, 2009.

[72] I. Friedler, C. Sauvan, J.-P. Hugonin, P. Lalanne, J. Claudon, and J.-M. Gérard, “Solid-state single photon sources: the nanowire antenna,” *Optics express*, vol. 17, no. 4, pp. 2095–2110, 2009.

[73] D. Dalacu, P. J. Poole, and R. L. Williams, “Nanowire-based sources of non-classical light,” *Nanotechnology*, vol. 30, p. 232001, mar 2019.

[74] M. Cygorek, M. Korkusinski, and P. Hawrylak, “Atomistic theory of electronic and optical properties of inasp/inp nanowire quantum dots,” *Physical Review B*, vol. 101, no. 7, p. 075307, 2020.

[75] D. Dalacu, K. Mnaymneh, J. Lapointe, X. Wu, P. J. Poole, G. Bulgarini, V. Zwiller, and M. E. Reimer, “Ultraclean emission from inasp quantum dots in defect-free wurtzite inp nanowires,” *Nano letters*, vol. 12, no. 11, pp. 5919–5923, 2012.

[76] S. Haffouz, K. D. Zeuner, D. Dalacu, P. J. Poole, J. Lapointe, D. Poitras, K. Mnaymneh, X. Wu, M. Couillard, M. Korkusinski, *et al.*, "Bright single inasp quantum dots at telecom wavelengths in position-controlled inp nanowires: the role of the photonic waveguide," *Nano letters*, vol. 18, no. 5, pp. 3047–3052, 2018.

[77] S. Haffouz, P. Poole, J. Jin, X. Wu, L. Ginet, K. Mnaymneh, D. Dalacu, and R. Williams, "Single quantum dot-in-a-rod embedded in a photonic nanowire waveguide for telecom band emission," *Applied Physics Letters*, vol. 117, no. 11, 2020.

[78] A. N. Wakileh, L. Yu, D. Dokuz, S. Haffouz, X. Wu, J. Lapointe, D. B. Northeast, R. L. Williams, N. Rotenberg, P. J. Poole, *et al.*, "Single photon emission in the telecom c-band from nanowire-based quantum dots," *Applied Physics Letters*, vol. 124, no. 4, 2024.

[79] O. Gazzano, T. Huber, V. Loo, S. Polyakov, E. Flagg, and G. Solomon, "Effects of resonant-laser excitation on the emission properties in a single quantum dot," *Optica*, vol. 5, no. 4, pp. 354–359, 2018.

[80] M. Müller, S. Bounouar, K. D. Jöns, M. Glässl, and P. Michler, "On-demand generation of indistinguishable polarization-entangled photon pairs," *Nature Photonics*, vol. 8, no. 3, pp. 224–228, 2014.

[81] A. V. Kuhlmann, J. Houel, D. Brunner, A. Ludwig, D. Reuter, A. D. Wieck, and R. J. Warburton, "A dark-field microscope for background-free detection of resonance fluorescence from single semiconductor quantum dots operating in a set-and-forget mode," *Review of scientific instruments*, vol. 84, no. 7, 2013.

[82] L. Leandro, J. Hastrup, R. Reznik, G. Cirlin, and N. Akopian, "Resonant excitation of nanowire quantum dots," *NPJ Quantum Information*, vol. 6, no. 1, p. 93, 2020.

[83] C. M. Natarajan, M. G. Tanner, and R. H. Hadfield, "Superconducting nanowire single-photon detectors: physics and applications," *Superconductor science and technology*, vol. 25, no. 6, p. 063001, 2012.

[84] K. Leosson, J. R. Jensen, J. M. Hvam, and W. Langbein, "Linewidth statistics of single ingaas quantum dot photoluminescence lines," *physica status solidi (b)*, vol. 221, no. 1, pp. 49–53, 2000.

[85] D. Gammon, E. Snow, B. Shanabrook, D. Katzer, and D. Park, "Homogeneous linewidths in the optical spectrum of a single gallium arsenide quantum dot," *Science*, vol. 273, no. 5271, pp. 87–90, 1996.

[86] H. G. Babin, J. Ritzmann, N. Bart, M. Schmidt, T. Kruck, L. Zhai, M. C. Löbl, G. N. Nguyen, C. Spinnler, L. Ranasinghe, *et al.*, "Charge tunable gaas quantum dots in a photonic nip diode," *Nanomaterials*, vol. 11, no. 10, p. 2703, 2021.

[87] R. Hui and M. O'Sullivan, *Fiber-Optic Measurement Techniques*. Academic Press, 2022.

[88] M. De Gregorio, S. Yu, D. Witt, B. Lin, M. Mitchell, Ł. Dusanowski, C. Schneider, L. Chrostowski, T. Huber-Loyola, S. Höfling, *et al.*, "Plug-and-play fiber-coupled quantum dot single-photon source via photonic wire bonding," *Advanced Quantum Technologies*, vol. 7, no. 1, p. 2300227, 2024.

[89] E. Yeung, D. B. Northeast, J. Jin, P. Laferriére, M. Korkusinski, P. J. Poole, R. L. Williams, and D. Dalacu, "On-chip indistinguishable photons using iii-v nanowire/sin hybrid integration," *Phys. Rev. B*, vol. 108, p. 195417, Nov 2023.

[90] P. Laferriére, E. Yeung, I. Miron, D. B. Northeast, S. Haffouz, J. Lapointe, M. Korkusinski, P. J. Poole, R. L. Williams, and D. Dalacu, "Unity yield of deterministically positioned quantum dot single photon sources," *Scientific Reports*, vol. 12, no. 1, p. 6376, 2022.

[91] P. Laferrière, E. Yeung, M. Korkusinski, P. J. Poole, R. L. Williams, D. Dalacu, J. Manalo, M. Cygorek, A. Altintas, and P. Hawrylak, "Systematic study of the emission spectra of nanowire quantum dots," *Applied Physics Letters*, vol. 118, no. 16, 2021.

[92] E. Yeung, *Hybrid integration of quantum dot-nanowires with photonic integrated circuits*. PhD thesis, Université d'Ottawa/University of Ottawa, 2021.

[93] D. Dalacu, D. B. Northeast, P. J. Poole, G. C. Aers, R. L. Williams, K. A. Owen, and D. Oblak, "Pump power control of photon statistics in a nanowire quantum dot," *Phys. Rev. B*, vol. 102, p. 115401, Sep 2020.

[94] P. Lodahl, S. Mahmoodian, and S. Stobbe, "Interfacing single photons and single quantum dots with photonic nanostructures," *Reviews of Modern Physics*, vol. 87, no. 2, pp. 347–400, 2015.

[95] P. Laferriére, E. Yeung, L. Giner, S. Haffouz, J. Lapointe, G. C. Aers, P. J. Poole, R. L. Williams, and D. Dalacu, "Multiplexed single-photon source based on multiple quantum dots embedded within a single nanowire," *Nano letters*, vol. 20, no. 5, pp. 3688–3693, 2020.

[96] K. Mnaymneh, D. Dalacu, J. McKee, J. Lapointe, S. Haffouz, J. F. Weber, D. B. Northeast, P. J. Poole, G. C. Aers, and R. L. Williams, "On-chip integration of single photon sources via evanescent coupling of tapered nanowires to sin waveguides," *Advanced Quantum Technologies*, vol. 3, no. 2, p. 1900021, 2020.

[97] X. Cao, M. Zopf, and F. Ding, "Telecom wavelength single photon sources," *Journal of Semiconductors*, vol. 40, no. 7, p. 071901, 2019.

[98] M. Benyoucef, M. Yacob, J. Reithmaier, J. Kettler, and P. Michler, "Telecom-wavelength (1.5 μm) single-photon emission from inp-based quantum dots," *Applied Physics Letters*, vol. 103, no. 16, 2013.

[99] M. Anderson, T. Müller, J. Huwer, J. Skiba-Szymanska, A. Krysa, R. Stevenson, J. Heffernan, D. Ritchie, and A. Shields, "Quantum teleportation using highly coherent emission from telecom c-band quantum dots," *npj Quantum Information*, vol. 6, no. 1, p. 14, 2020.

[100] T. Stievater, X. Li, D. G. Steel, D. Gammon, D. Katzer, D. Park, C. Piermarocchi, and L. Sham, "Rabi oscillations of excitons in single quantum dots," *Physical Review Letters*, vol. 87, no. 13, p. 133603, 2001.

[101] J. Villas-Bôas, S. E. Ulloa, and A. Govorov, "Decoherence of rabi oscillations in a single quantum dot," *Physical review letters*, vol. 94, no. 5, p. 057404, 2005.

[102] E. Schöll, L. Hanschke, L. Schweickert, K. D. Zeuner, M. Reindl, S. F. Covre da Silva, T. Lettner, R. Trotta, J. J. Finley, K. Müller, *et al.*, "Resonance fluorescence of gaas quantum dots with near-unity photon indistinguishability," *Nano letters*, vol. 19, no. 4, pp. 2404–2410, 2019.

[103] M. E. Reimer, G. Bulgarini, A. Fognini, R. W. Heeres, B. J. Witek, M. A. M. Versteegh, A. Rubino, T. Braun, M. Kamp, S. Höfling, D. Dalacu, J. Lapointe, P. J. Poole, and V. Zwiller, "Overcoming power broadening of the quantum dot emission in a pure wurtzite nanowire," *Phys. Rev. B*, vol. 93, p. 195316, May 2016.

[104] O. Gazzano, V. Loo, S. Polyakov, T. Huber, E. Flagg, and G. Solomon, "Resonant excitation linewidth narrowing of quantum dots emission," in *Quantum Information and Measurement*, pp. QT6A–8, Optica Publishing Group, 2017.

[105] L. Rickert, D. A. Vajner, M. von Helversen, J. Schall, S. Rodt, S. Reitzenstein, H. Liu, S. Li, H. Ni, Z. Niu, *et al.*, "High purcell-enhancement in quantum-dot hybrid circular bragg grating cavities for ghz-clockrate generation of indistinguishable photons," *arXiv preprint arXiv:2408.02543*, 2024.

[106] M. E. Reimer, M. P. van Kouwen, A. W. Hidma, M. H. van Weert, E. P. Bakkers, L. P. Kouwenhoven, and V. Zwiller, “Electric field induced removal of the biexciton binding energy in a single quantum dot,” *Nano letters*, vol. 11, no. 2, pp. 645–650, 2011.

[107] D. N. Klyshko, “Basic quantum mechanical concepts from the operational viewpoint,” *Physics Uspekhi*, vol. 41, pp. 885–922, Sept. 1998.